IRAQI JOURNAL OF APPLIED PHYSICS

The *Iraqi Journal of Applied Physics (IJAP)* is a peer reviewed journal of high quality devoted to the publication of original research papers from applied physics and their broad range of applications. IJAP publishes quality original research papers, comprehensive review articles, survey articles, book reviews, dissertation abstracts in physics and its applications in the broadest sense. It is intended that the journal may act as an interdisciplinary forum for Physics and its applications. Innovative applications and material that brings together diverse areas of Physics are particularly welcome. Review articles in selected areas are published from time to time. It aims to disseminate knowledge; provide a learned reference in the field; and establish channels of communication between academic and research experts, policy makers and executives in industry, commerce and investment institutions. IJAP is a quarterly specialized periodical dedicated to publishing original papers, letters and reviews in: Applied & Nonlinear Optics, Applied Mechanics & Thermodynamics, Digital & Optical Communications, Electronic Materials & Devices, Laser Physics & Applications, Plasma Physics & Applications, Quantum Physics & Spectroscopy, Semiconductors & Optoelectronics, Solid State Physics & Applications, Alternative & Renewable Energy, and Environmental Science & Technology.

ISSN (Print): 1813-2065, ISSN (Online): 2309-1673

Editorial Office:
P. O. Box 88052, Baghdad 12631, IRAQ
Mobile: +964 7832 360 114 (Telegram, Viber, WhatsApp)
Website: www.iraqiphysicsjournal.com
Emails: info@iraqiphysicsjournal.com, editor_ijap@yahoo.co.uk, ijap.editor@gmail.com,

SPONSORED AND PUBLISHED BY
AMERICAN QUALITY FOR SCIENTIFIC PUBLISHING INC.
1479 South De Gaulle Ct, Aurora, CO 80018, United States

IRAQI JOURNAL OF APPLIED PHYSICS

INSTRUCTIONS TO AUTHORS

CONTRIBUTIONS

Contributions to be published in this journal should be original research works, i.e., those not already published or submitted for publication elsewhere, individual papers or letters to editor.
Manuscripts should be submitted to the editor at the mailing address:

Iraqi Journal of Applied Physics, Editorial Board, P. O. Box 88052, Baghdad 12631, IRAQ
Mobile: +964 7832 360 114 (Telegram, Viber, WhatsApp)
Website: www.iraqiphysicsjournal.com
Email: info@iraqiphysicsjournal.com, editor_ijap@yahoo.co.uk, ijap.editor@gmail.com

MANUSCRIPTS

Two hard copies or a soft Word copy on a CD or DVD should be submitted to the Editor in the following configuration:

- **One-column** Double-spaced one-side A4 size with 2.5 cm margins of all sides
- Times New Roman font (16pt bold for title, 14pt bold for names, 12pt bold for headings, 12pt regular for text)
- Manuscripts presented in English only are accepted.
- English abstract not exceed 150 words
- 4 keywords (at least) should be maintained on (PACS preferred)
- Author(s) should express all quantities in SI units
- Equations should be written in equation form (*italic* and symbolic) NOT in plain text
- Tables and Figures should be separated from text and placed in new pages after the references
- Charts should be indicated by the software used for generating them (e.g., Excel, MATLAB, Grapher, etc.)
- Figures and diagrams can be submitted in original colored forms for assessment and they will be returned to authors after provide printable copies
- Only original or high-resolution scanner photos are accepted
- For electronic submission, articles should be formatted with MS-Word software
- Figures, charts, photos, images or pictures **SHOULD NOT** be grouped in Word file
- Figure caption should be written as plan text **NOT** inside a text box

AUTHOR NAMES AND AFFILIATIONS

It is IJAP policy that all those who have participated significantly in the technical aspects of a paper be recognized as co-authors or cited in the acknowledgments. In the case of a paper with more than one author, correspondence concerning the paper will be sent to the first author unless staff is advised otherwise.
Author name should consist of first name, middle initial, last name. The author affiliation should consist of the following, as applicable, in the order noted:
- Company or college (with department name or company division), Postal address, City, Governorate or State, zip code, Country name, contacting telephone number, and e-mail

REFERENCES

The references should be brought at the end of the article, and numbered in the order of their appearance in the paper. The reference list should be cited in accordance with the following examples:
[1] F.H. Al-Berkdar, D.N. Raouf and F.H. Hamza, "A Line Tuned TEM_{00} Mode CW CO_2 Laser", *Iraqi J. Appl. Phys.*, 1(1) (20025) 8-10.
[2] W. Demtröder, **"Atoms, Molecules, and Photons"**, Springer-Verlag (Berlin, 2006), Ch. 4, p. 130.
[3] Y. Lee, S.A. Korpela and R. Horne, "Structure of Multi-Cellular Natural Convection in a Tall Vertical Annulus", Proceedings of 7th International Heat Transfer Conference, U. Grigul et al., eds., Hemisphere (NY), 2 (1982) 221–226.
[5] M. Hashish, "Waterjet Technology Development", High Pressure Technology, PVP-Vol. 406 (2000) 135-140.
[6] D.W. Watson, "Thermodynamic Analysis", ASME Paper No. 97-GT-288 (1997).
[7] Z. Cheng, "Vibrational Discrete Action Theory", Ph.D. thesis, Columbia University, USA (2021).

PROOFS

Authors will receive proofs of papers and are requested to return one corrected copy as a WORD file on a compact disc (CD) or by email. New materials inserted in the original text without Editor's permission may cause rejection of paper unless the handling editor is informed.

COPYRIGHT FORM

Author(s) will be asked to sign the IJAP Copyright Form and hence transfer copyrights of the article to the Journal soon after acceptance of it. This will ensure the widest possible dissemination of information.

OFFPRINTS

Authors will receive electronic offprint free of charge and any additional reprints can be ordered.

SUBSCRIPTION AND ORDERS

Annual fees (4 issues per year) of subscription are:
50 US$ for individuals inside Iraq; **200** US$ for institutions inside Iraq; **100** US$ for individuals abroad; **300** US$ for institutions abroad.

IRAQI JOURNAL OF APPLIED PHYSICS
Vol. 19, No. 4A, October 2023, pp. 3-12

Hasan A. Tawfeeq
Jamal M. Rzaij

Department of Physics,
College of Science,
University of Anbar,
Ramadi, IRAQ

Effect of Nb_2O_5 and PdO Coatings on Sensing Characteristics of Nanostructured CdO Thin Films

In this study, a multilayer gas sensor based on CdO coated with Nb_2O_5 and CdO coated with PdO is developed using an effective thermal-vacuum evaporation deposition. The structural characteristics were studied by X-ray diffraction (XRD). Field emission scanning electron microscopy (FE-SEM) and atomic force microscopy (AFM) were used to investigate morphological and topographical features. FE-SEM study validated the nanofiber-like structures with clusters of spherical particles, while AFM analysis showed an average diameter of 14.21 nm to 37 nm. Various gas concentrations and work temperatures were used to analyze the sensing properties of CO_2 and NH_3. This work could facilitate the fabrication of nanostructured thin film oxides with distinguishing structural and morphological features for interesting gas sensor applications.

Keywords: Cadmium oxide; Thin films; Thermal Vacuum Evaporation; Gas sensor
Received: 06 June 2023; **Revised:** 18 July 2023; **Accepted:** 25 July 2023

1. Introduction

Due to their extensive potential applications in numerous scientific and technological disciplines, such as electronics, optics, aviation science, defense, etc., the preparation of thin films with nanoscale dimensions is of the utmost importance [1-3]. Also, the design of nanostructures of various semiconductor materials or conductors can contribute to improving their original properties [4-7]. Many physical and chemical methods, such as pulsed laser deposition, ion beam sputtering, thermal evaporation, vacuum deposition, chemical vapor deposition, co-precipitation, sol-gel, chemical bath deposition, etc. are available for the preparation of thin films [8-13]. With a direct band gap of 2.5 eV and an indirect band gap of 1.98 eV [14-16], CdO, a significant n-type semiconductor, has intriguing uses in a variety of industries, including solar cells, phototransistors, transparent electrodes, catalysts, and gas sensors [17,18]. Particle size, porosity, and specific surface area are crucial factors in these applications. Nanowires [19], nanobelts [20], and nanoparticles [21] are only a few of the intriguing morphologies of CdO nanostructures that have been created thus far. Niobium pentoxide has gained attention and widespread scientific interest in recent years as a substance with several uses. One of the widely used transparent oxide semiconductor materials is this one [22]. Due to its wide band gap, inability to dissolve in water, and air stability, this substance is transparent in the ultraviolet (UV) region. Its structure is rather complicated and exhibits polymorphism depending on the conditions and technique of manufacture [23,24]. Due to its use in solar cells, batteries, photo-detectors, and other electronic devices, particularly nanostructured Nb_2O_5, attention to Nb_2O_5 has increased [25-27]. PdO is a p-type oxide semiconductor [28,29] whose research into it as a gas-sensing material is still in its infancy. The literature on the mechanism of oxygen species respondingto CO has contradictory results. Chiang and Pan [30] provide the oxygen ionosorption hypothesis for the CO sensing mechanism on PdO. The combination of chemisorbed oxygen with co-adsorbed CO at low temperature led to the sensing behaviour of PdO. During the air gas-sensing reaction, Pd was able to maintain its oxidation state. In the literature, PdO species' reactivity towards CO oxidation has been researched and compared [31].

Due to the high surface-to-volume ratio, metal oxide nanoparticles increase the chemical reaction rates on the sensor surface of the thin films. This maximizes the interaction between the exposed surface of the nanostructured coatings and the gas species, significantly altering their physical and chemical properties [32]. This study aims to investigate the influence of Nb_2O_5 and Pdo coatings on the structural, morphological, and optical properties of nanostructured CdO thin films to develop a multilayer gas sensor for CO_2 and NH_3 detection under varying conditions.

2. Experimental Part

The sensor samples were prepared using CdO, Nb_2O_5 and PdO powders purchased from ReaChem, India (purity >99%). Two substrates were employed to deposit thin films. The first were glass substrates from China's National Equipment with dimensions of 25.5×76.2 cm^2 and thickness of 1-1.2 mm^2. The second were n-type silicon substrates (0.1-100 Ω.cm) with diameter of 2.25 cm^2. The glass and silicon substrates were cleaned with soap, rinsed with water, ultrasonically bathed, treated with an ethanol solution for impurities, and air-blasted for complete drying.

Thermal vacuum evaporation was used to deposit thin films under a high vacuum (≈3×10^{-5} mbar). A dc current was applied through the tungsten boat to heat the powder to the melting point before evaporating and depositing it on the substrate. The deposited films were annealed at 300°C for 1 hour in the air. For a 200±5 nm CdO film thickcness, 0.21 g of CdO powder was used, while 0.07 g and 0.11 g were used for 70±5 nm Nb_2O_5 and PdO thickcness, respectively. The first layer was a thin layer of CdO, followed by a thin layer of Nb_2O_5 deposited on top of the CdO layer (Nb_2O_5/CdO). Finally, the preceding procedures are repeated with PdO substituted for Nb_2O_5 (PdO/CdO).

The structural properties of CdO, Nb_2O_5/CdO, and PdO/CdO thin films were studied using a Bruker D2 PHASER x-ray diffractometer with a Cu-Kα x-ray tube (λ =1.5406Å) and diffraction angle (2θ) ranging in 10-80°. The MIRA3 model-TE-SCAN field-emission scanning electron microscope (FE-SEM) was used to analyze the surface morphology of developed films. Roughness and grain size were investigated by atomic force microscopy (AFM) using an Angstrom AA3000 Scanning Probe Microscope (SPM). A SPX500 photoluminescence (PL) spectrometer with a 325nm He-Cd laser as an excitation source, and a beam power of 20 mW at room temperature were utilized to investigate electronic transitions. The thickness of the prepared sensors was estimated using cross-sectional FE-SEM images and ImageJ software.

3. Results and Discussion

The XRD matching and chemical element identification were performed using X'Pert High Score software. Figure (1) indicates the XRD pattern of a Nb_2O_5/CdO sample with a thickness of 70 nm Nb_2O_5 deposited on 200 nm CdO. The results confirm the presence of cubic CdO crystal system with sharp diffraction peaks toward (111), (200), and (220), matcing the reference JCPDS 96-900-6688 [33]. Additionally, it signifies the development of an orthorhombic Nb_2O_5 phase, characterized by a relatively weak diffraction peak along the (100) direction, which aligns with the findings reported in the JCPDS 00-030-0873 reference [34]. The absence of any additional diffraction peaks and the sharpness of the peaks, which suggest excellent crystallization, both attest to the high purity of the Nb_2O_5/CdO sample.

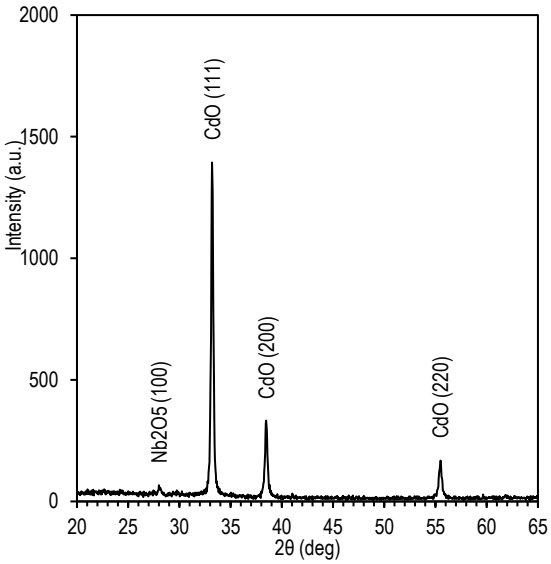

Fig. (1) The XRD pattern of Nb_2O_5/CdO thin film

The crystallite size (C.S) was calculated using Scherrer's equation as follows [35,36]:

$$C.S = \frac{0.9\lambda}{\beta \cos\theta} \quad (1)$$

where (λ) is the x-ray wavelength (1.5406Å), θ is the diffraction angle, and β is the full-width at half maximum (FWHM) of the peaks. This can be explained by a rise in the number of deposited particles from the target toward the substrate as the powder weight in the deposition boat increases.

Table (1) XRD parameters of Nb_2O_5/CdO thin film

2θ (deg)	FWHM (deg)	d_{hkl} Exp. (Å)	C.S (nm)	Hkl	Phase
28.0286	0.2883	3.1809	28.4	(100)	Orth. Nb_2O_5
33.1296	0.1996	2.7019	41.5	(111)	Cubic CdO
38.4968	0.2420	2.3366	34.8	(200)	Cubic CdO
55.4411	0.2884	1.6560	31.1	(220)	Cubic CdO

Figure (2) shows the XRD pattern of PdO/CdO thin-film samples with a thickness of 70 nm PdO deposited on 200 nm CdO. The results confirm the presence of distinct diffraction peaks for a cubic CdO with a diffraction peaks (100), (200), and (220). This result is consistent with the JCPDS 96-900-6688 [33].

Furthermore, the results shows diffraction peaks towards the (110) and (200) at angels of 29.3902° and 61.9186°, respectively, belonging to tetragonal crystal system of PdO, according to JCPDS 96-101-1330 [37]. Depending on the XRD parameters in table (2), the results confirm an increase in the average crystallite size. The absence of some diffraction peaks for PdO and Nb_2O_5 oxides may be attributed to their small thickness compared to CdO film [38]. The increase in crystalline size indicates an increase in the agglomeration of atoms with each other, which contributes to an increase in their size, which is what the gas sensor needs [39].

 ISSN (print) 1813-2065, (online) 2309-1673

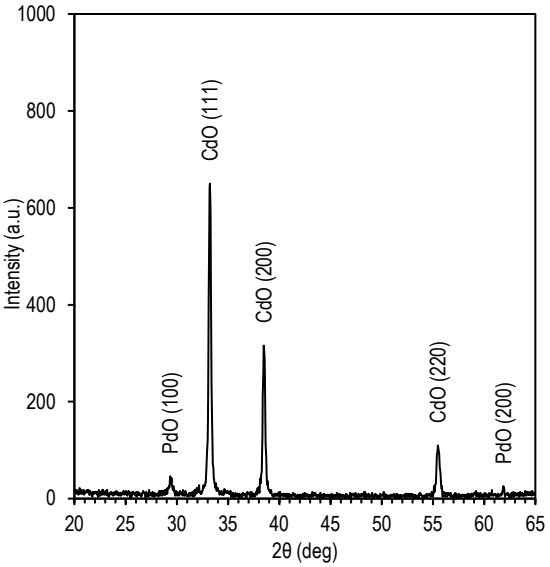

Fig. (2) The XRD pattern of PdO/CdO thin film

Table (2) XRD parameters of PdO/CdO thin film

2θ (Deg.)	FWHM (Deg.)	d_{hkl} Exp. (Å)	C.S (nm)	hkl	Phase
29.3902	0.2918	3.0366	28.1	(100)	Tet. PdO
33.1792	0.280	2.6979	29.6	(111)	Cubic CdO
38.4887	0.2918	2.3371	28.8	(200)	Cubic CdO
55.4822	0.310	1.6549	29.0	(220)	Cubic CdO
61.9186	0.2553	1.4974	36.3	(200)	Tet. PdO

The FE-SEM was used to study the surface morphology of the deposited films and determine their thickness, in addition to study the effect of the nanopowder concentration on the particle size of the deposited films.

Figure (3) shows the top view, cross-sectional, and a diagram of the particle size distribution. Figure (3a) shows the FE-SEM image of the Nb_2O_5 film, which shows a regular distribution free of cracks, in addition to that the atoms were deposited to appear in the form of small, regular-shaped spherical agglomerates with different dimensions. Figure (3b) shows that the thickness of the deposited Nb_2O_5film was about 90 nm, while the graphic distribution of the formed granules shown in Fig. (3c) indicates that the amount of grain size is 32 nm [40].

Figure (4a) shows the FE-SEM image of the PdO film, which shows a regular distribution free of cracks; in addition to that the atoms were deposited to appear in the form of small, regular-shaped spherical agglomerates with different dimensions. Figure (4b) also shows that the thickness of the deposited PdO film was about 85 nm, while the graphic distribution of the formed granules shown in Fig. (4c) indicates that the averagegrain size was 12 nm [41].

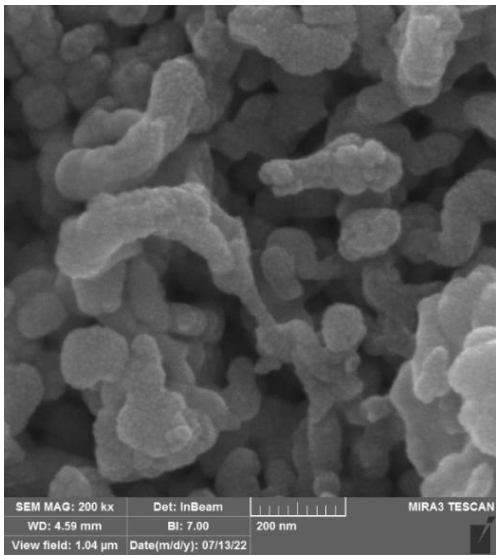

(a)

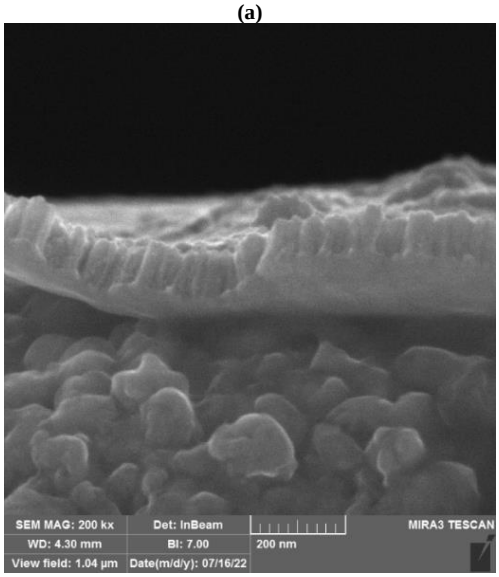

(b)

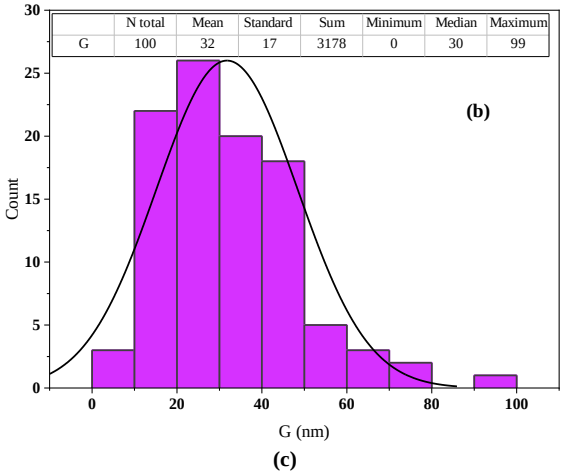

(c)

Fig. (3) FE-SEM microimages of (a) top-view, (b) cross-sectional, and (c) grain size distribution of Nb_2O_5/CdO sample

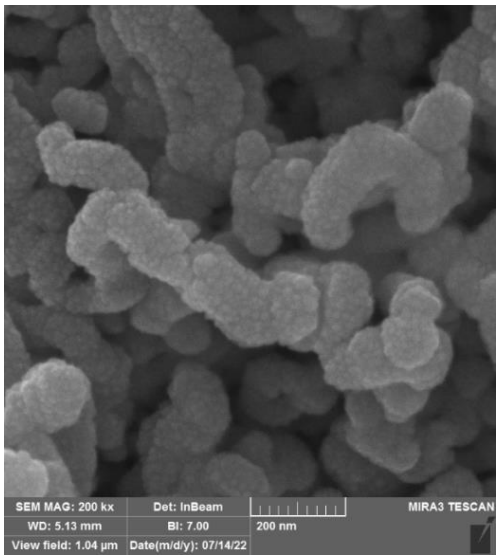

(a)

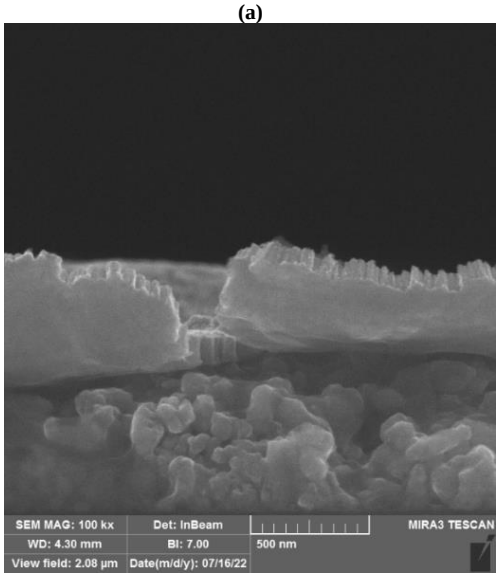

(b)

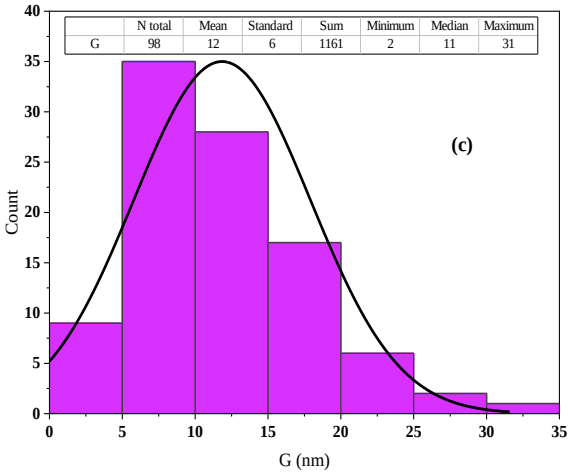

Fig. (4) FE-SEM microimages of (a) top-view, (b) cross-sectional, and (c) grain size distribution of PdO/CdO sample

Figure (5) shows the 2D and 3D AFM images of the Nb_2O_5/CdO thin film structure deposited on a silicon substrate under the influence of different RF power at room temperature. The low-power pictures show that the films are consistent and that the substrate surface is thoroughly coated with grains that are almost evenly spaced apart when RF power is increased. The microstructure of the deposited films revealed the creation of the particles, and as the power is increased, certain tiny grains grew larger [41].

High-roughness films play an essential role in electronic and optical applications and gas sensors due to their large surface area, which greatly enhances the absorption of light in the visible region. Also, these films are good trap for target gas molecules, which gives a good idea of the surface quality and grain growth [42]. Average grain size (G_{Save}) obtained from the distribution charts of the aggregated grains grown on the surfaces of thin films.

Figure (5a) shows a 2D AFM image of the Nb_2O_5/CdO thin film structure topography. It was found that the average surface roughness of this structure was 3.787 nm, with a root mean square (Sq) roughness of 6.569 nm. Figure (5b) also shows a 3D AFM image, which indicates a semi-uniform distribution of depsoited atoms, which arrange themselves to show a pyramid-like structure, with an average grain size of 14.21 nm (Fig. 5c).

Figure (6a) shows a 2D AFM image of the PdO/CdO thin film sample topography. It was found that the average surface roughness of the film was 1.267 nm, with a root mean square (Sq) of 1.552 nm. Figure (6b) also shows a 3D AFM image, which shows a uniform distribution of deposited atoms, with an average grain size of 37.00 nm (Fig. 6c).

From observing the behavior of the previous two models (Nb_2O_5/CdO) and (PdO/CdO), the results showed a decrease in the average of surface roughness from 3.787 to 1.267 nm and a decrease in the root mean square (Sq) from 6.569 to 1.552 nm. Figure (6b) shows a 3D AFM image that reveals the disappearance of some peaks with emerging hierarchical shapes, which contributed to the reduction of surface roughness, and the decrease in the average particle size to 33.98 nm, which contributed to the decrease in the average and mean square root roughness values, which in turn will contribute to increase the smoothness of the surface and the regularity of the deposited atoms.

Comparing the XRD, FE-SEM and AFM results, we observe that the decrease in crystallite size and grain size when coating the CdO film with Nb_2O_5 and PdO nanoparticles at a concentration of 2 mM is consistent, indicating that the prepared films exhibit uniform crystalline, morphological, and topographical properties.

 ISSN (print) 1813-2065, (online) 2309-1673

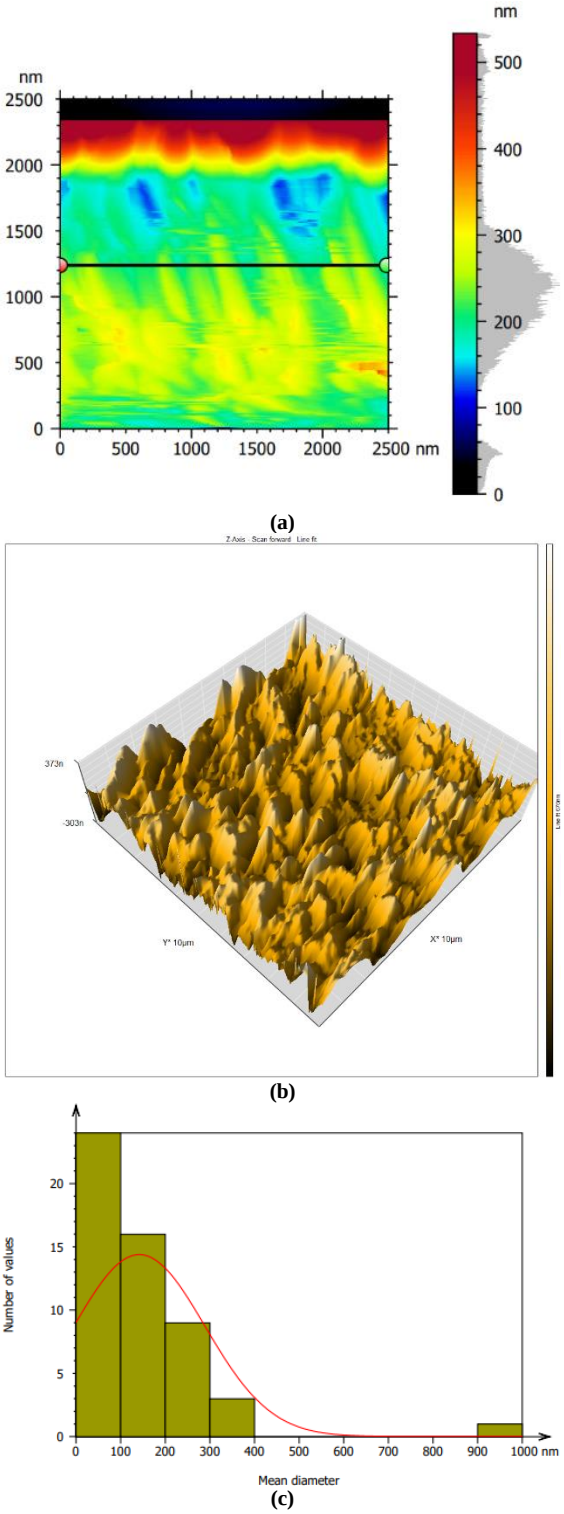

Fig. (5) (a) 2D, (b) 3D AFM images of Nb_2O_5-coated CdO thin film, and (c) distribution of particle diameters

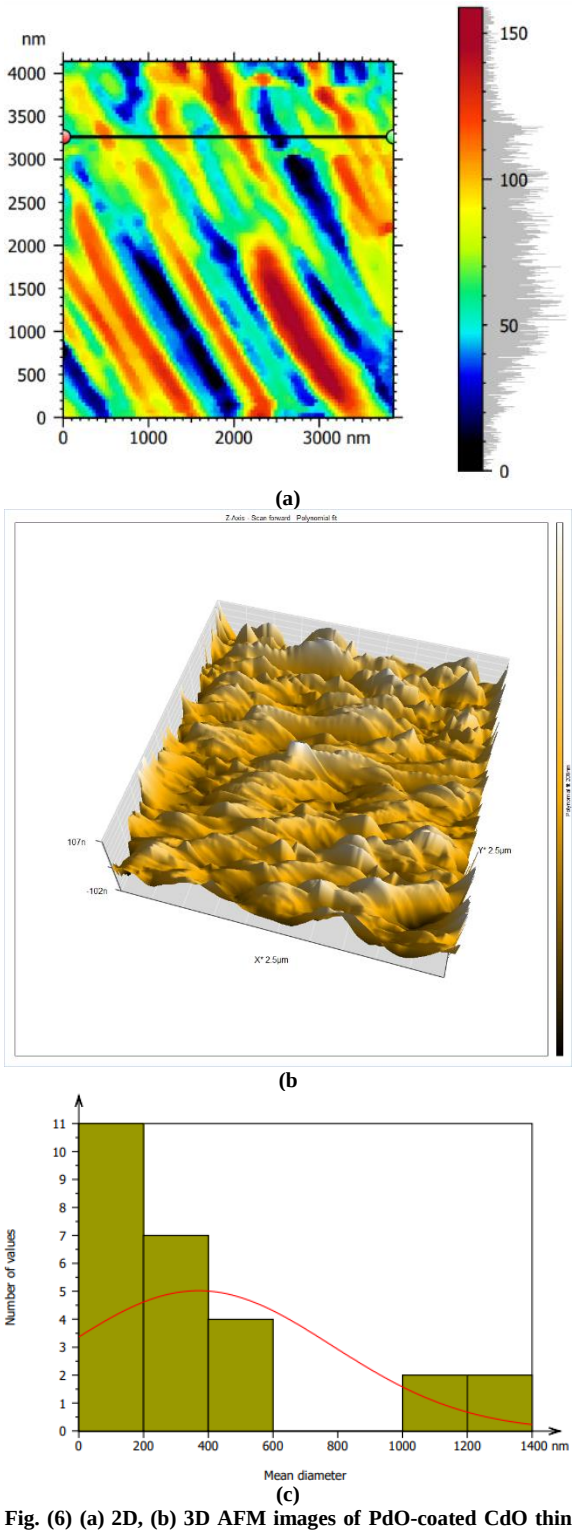

Fig. (6) (a) 2D, (b) 3D AFM images of PdO-coated CdO thin film, and (c) distribution of particle diameters

Figure (7) illustrates the variation of electrical conductivity (logσ) with operating temperature. With a temperature rise, an increase in conductivity is shown in each sample. The semiconducting nature of the multilayer materials and negative temperature coefficient of resistance caused the conductivity to rise as the temperature was raised [44,45].

Table (3) shows that all films have two activation energies because Nb_2O_5 and PdO have spinel structure, therefore, it is known that normal spinal have hopping kind of mechanism for carrier conductivity. The conduction of the films was confirmed to be due to polaronic hopping of holes. This is in agreement with Chun et al [41].

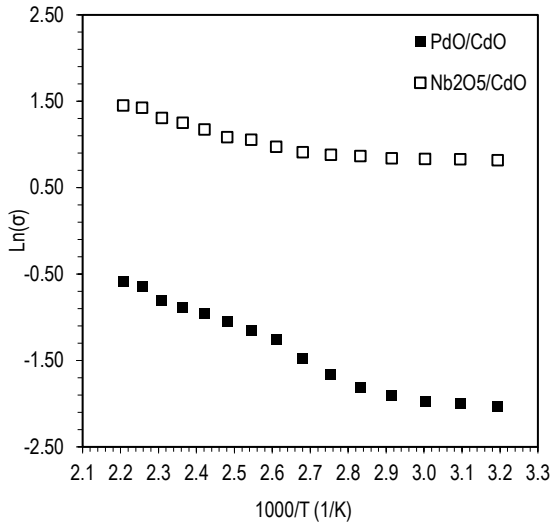

Fig. (7) Variation of log (σ) as a function of operating temperature

Table (3) Activation energies of the preapered samples

Sample	E_{a1} (eV)	Range (K)	E_{a2} (eV)	Range (K)	σ_{RT} $(\Omega.cm)^{-1}$
Nb_2O_5/CdO	0.010	303-363	0.095	363-453	2.27
PdO/CdO	0.026	303-343	0.166	343-453	0.13

One of the important optical analyses is the photoluminescence (PL). Figure (8) shows the PL spectra of the prepared Nb_2O_5/CdO thin film samples with an excitation wavelength of 320 nm. The spectrum shows PL bands catered at 403.12, 477.60, 580.81, 662.83, and 745.03 nm. The emission at 477.60 nm (2.60 eV) corresponds to the direct band-to-band radiative transition, which has less energy gap than the pure CdO film. The broad emission band at 580.8 nm corresponds to the exciton bound to the donor-level emission [46]. In addition, another bands located at 662.83 and 745.03 nm correspond to defect centers and oxygen vacancies or metal interstitials.

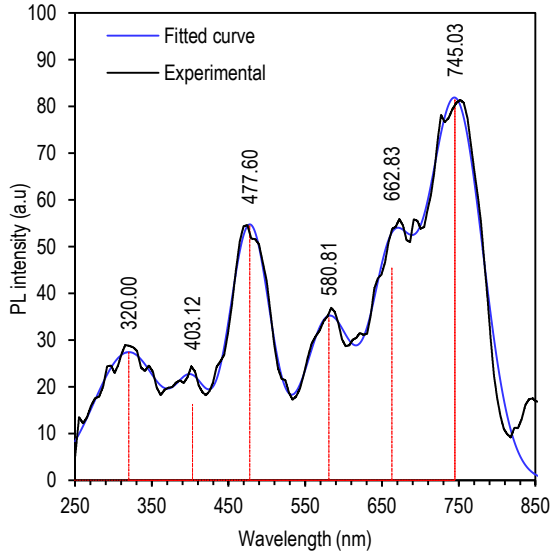

Fig. (8) PL spectra of the prepared Nb_2O_5/CdO structure

Table (4) PL emission peaks for the Nb_2O_5/ CdO thin film

Wavelength (nm)	FWHM (nm)	Intensity (a.u)	E (eV)
403.12	49.32	16.2	3.08
477.60	63.57	54.4	2.60
580.81	76.17	34.8	2.13
662.83	62.23	45.4	1.87
745.03	85.13	81.5	1.66

Figure (9) shows the PL spectra of the prepared PdO/CdO thin film structure with an excitation wavelength of 310 nm. The spectra show many bands located at 404.98, 482.13, 563.83, 634.32, and 784.48 nm. The emission at 482.13 nm (2.57 eV) corresponds to the band-to-band transition for the recombination of conducting electrons with holes.

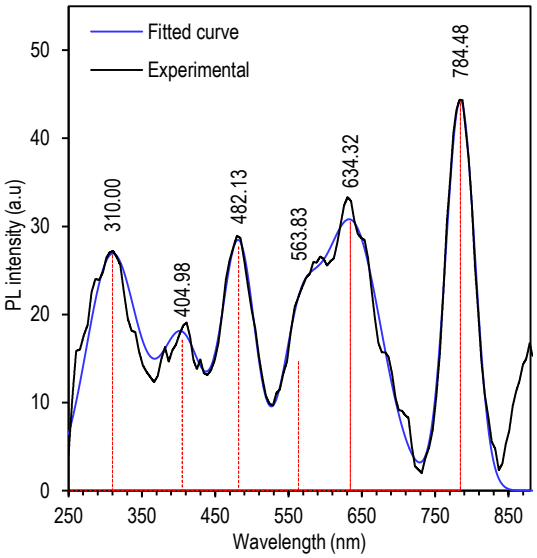

Fig. (9) PL spectra of the prepared PdO/CdO structure

The broad intense emission bands at 563.83 and 634.32 nm are attributed to the defect centers due to the donor localized levels. While the emergence of the PL emission line at 784.48 nm is due to the doping effect. The high intensity of these peaks is due to the presence of new defect centers induced by impurities after composing with Pd and Nb ions. This agrees with the doping effect of metal ions compared to work reported with other metal ions such as Al [47]. The pure CdO film does not show such a large peak as observed in the doped films.

Table (5) PL emission peaks for the PdO/ CdO thin film

Wavelength (nm)	FWHM (nm)	Intensity (a.u)	E (eV)
404.98	69.86	17.2	3.06
482.13	53.47	27.8	2.57
563.83	56.35	14.7	2.20
634.32	98.01	30.6	1.95
784.48	46.78	44.3	1.58

The gas response (S%) of the sensor can be mathematically expressed as the ratio of the change

 ISSN (print) 1813-2065, (online) 2309-1673

in the sensor's initial electrical current to the sensor's electrical current when subjected to a specific target ga concentration (Eq. 2) [40], assuming constant operating conditions, as

$$S(\%) = \frac{I_g - I_a}{I_a} \quad (2)$$

where I_a is the electrical current of the sensor when exposed to atmospheric conditions, and I_g is the electrical current of the sensor when exposed to target gas

Figure (10) illustrates the relationship between the gas response and the operating temperature of the samples when exposed to a concentration of 17.25 ppm of CO_2 gas. From Fig. (10a), it can concluded that the response of the Nb_2O_5/CdO sample to $CO_{2\ gas}$ shows a maximum sensitivity (90.7%) at room temperature as compared to PdO/CdO sample (19.5%) (Fig. 10b). It is well known that interactions between a target gas and the surface of the metal oxide semiconductor sensors play a major role in determining their response [48]. The sensor has a strong response to CO_2 gas even at working temperature up to 350 °C.

Figure (11a) depicts the variation in the reaction of the Nb_2O_5/CdO samples to 78.58 ppm of NH_3 gas as a function of operating temperature. For the PdO/CdO samples, the response declines with increasing operating temperature and reaches a maximum (2.5%) at 150°C before falling further to 17.2% with increasing operating temperature to 150°C (Fig. 11b). The speed of the chemical reaction taking place on the grain's surface and the rate at which gas molecules diffuse to that surface determines how quickly sensors react to these two variables. These are activation processes, and chemical reactions have higher activation energy. The pace of chemical reactions limits the sensor responsiveness at low temperatures [49]. The speed of the gas molecules' migration to that surface limits the sensor response at higher temperatures. The maximum sensor response occurs when the two processes are equal in rate at some intermediate temperature. According to this process, the sensor response reaches its maximum value at a certain temperature for each gas.

The sensor chooses to sense a certain gas at a specific temperature. As a result, the sensor may be used to identify a specific gas by adjusting the temperature. By running it at a certain temperature for a common gas, the same sensor may be used to detect a variety of gases. At various temperatures, the sensor response would vary on the gas being detected since gases have different energies for reaction on the metal oxide surface, desorption, and adsorption [50].

The rapid recuperation of the sensor can be attributed to the significant volatility exhibited by the by-product. The Nb_2O_5/CdO sample showed better recovery to CO_2 than PdO/CdO sample. While we see the response of the Nb_2O_5/CdO and PdO/CdO thin film to NH_3 are relatively close.

Various reaction pathways can lead to the oxidation of CO_2 on the CdO surface, depending on the surface's composition, structure, temperature, and species that have been adsorbed. Reaction complexes and intermediates are typically short-lived compounds that are challenging to identify. To understand the CO_2 gas sensing mechanism, we must understand the quantity and extent of oxygen species present on the surface, how CO_2 is adsorbed on the surface, the potential reaction pathways and the rates of each step, as well as the possibility of other elements interfering with the reaction and their presence.

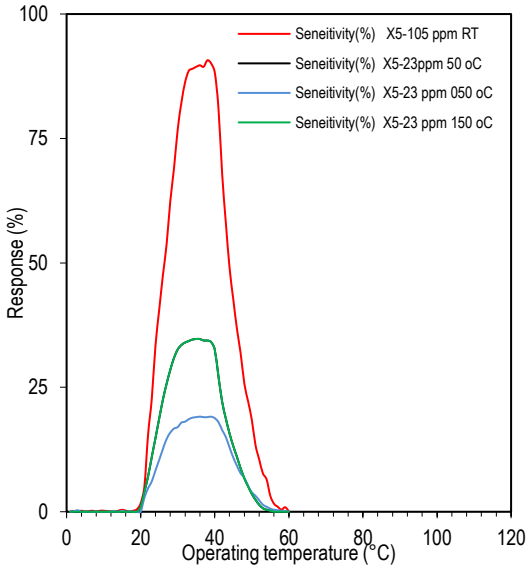

(a)

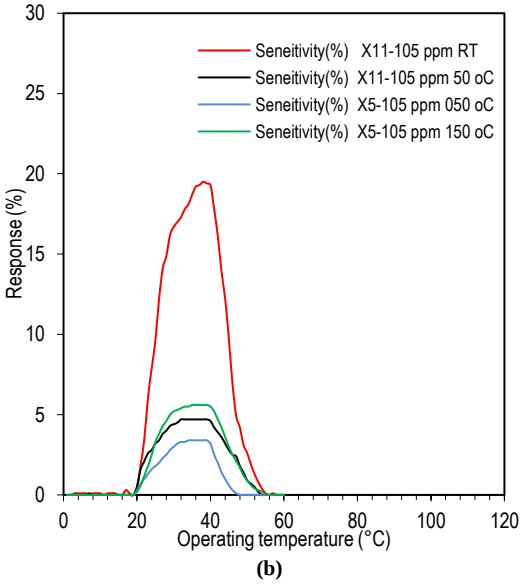

(b)

Fig. (10) Variation of response to CO_2 gas vs. operating temperature of (a) Nb_2O_5/CdO sample, and (b) PdO/CdO sample

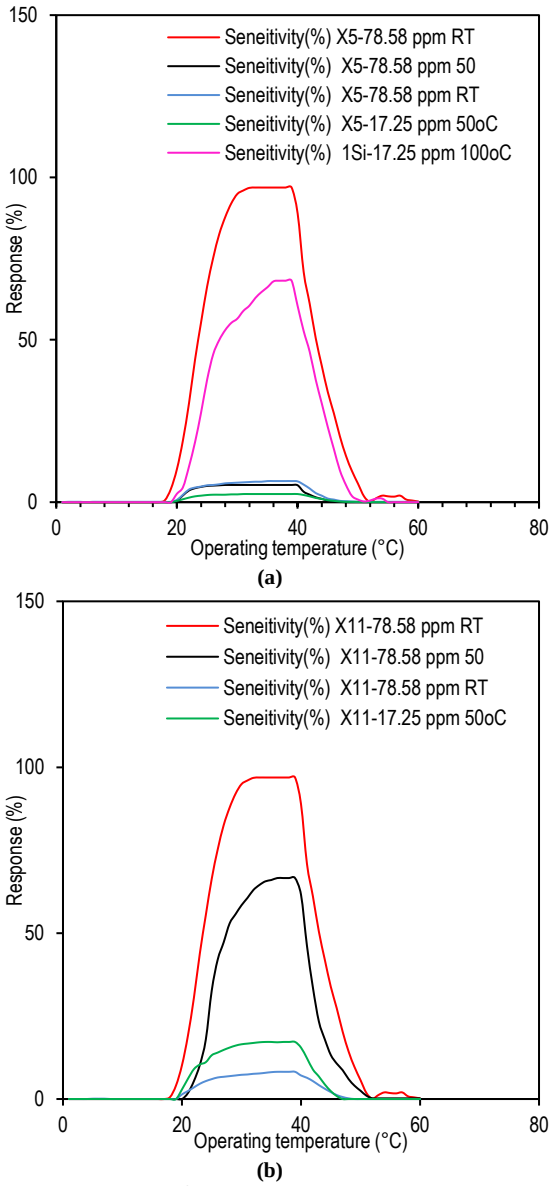

Fig. (11) Variation of response to NH_3 gas vs. operating temperature of (a) Nb_2O_5/CdO sample, and (b) PdO/CdO sample

The reaction time is the time required by the sensor to achieve 90% of the maximum resistance drop after being exposed to the target gas. The recovery time is the time required by the sensor to regain 90% of its initial resistance. When the sensor was exposed to a concentration of 17.25 ppm of NH_3 and CO_2 at different operating temperatures, the high sensitive structure composed of Nb_2O_5/CdO thin films exhibited rapid recovery (12.4s) and response (10.9s) to NH_3 and CO_2. This can be attributed to the presence of highly oxidizing and adsorbed oxygen species on the surface of the nanoparticles film [41].

4. Conclusions

The Nb_2O_5/CdO and PdO/CdO thin film structures were successfully deposited on glass and silicon substrates using the thermal vacuum evaporation technique. The current study confirmed that the deposition of a top layer of Nb_2O_5 or PdO significantly affected the structural and morphological properties of the CdO gas sensor, improving the sensitivity when exposed to various concentrations of CO_2 and NH_3 at various operating temperatures. One of the essential characteristics of this sensor is its fast response and short recovery time, so the developed sensors can effectively contribute to rapidly detect harmful gases in various environmental conditions.

Acknowledgments

The authors thank the University of Anbar for the support that was provided for this work.

References

[1] F. Iacomi et al., "Physical characterization of CdMnS nanocrystalline thin films grown by vacuum thermal evaporation", *J. Optoelectron. Adv. Mater.*, 8(1) (2006) 266.
[2] M. Jaiswal et al., "Synthesis of CrO_3 intercalated multilayer graphene for rapid and reversible NH_3 gas sensing", *Sens. Actuat. B: Chem.*, 310 (2020) 127826.
[3] O.A. Hamadi, K.Z. Yahiya and O.N.S. Jassim, "Properties of Silicon Carbide Thin Films Deposited by Vacuum Thermal Evaporation", *J. Semicond. Technol. Sci.*, 5(3) (2005) 182-186.
[4] R.S. Sabry, W.J. Aziz and M.I. Rahmah, "Employed Silver doping to improved photocatalytic properties of ZnO micro/nanostructures", *J. Inorg. Organomet. Polym. Mater.*, 30(11) (2020) 4533-4543.
[5] A. Singh et al., "The recent development of metal oxide heterostructures based gas sensor, their future opportunities and challenges: a review", *Sens. Actuat. A: Phys.*, 332 (2021) 113127.
[6] M.W. Alam et al., "The Recent Development in Chemoresistive-Based Heterostructure Gas Sensor Technology, Their Future Opportunities and Challenges: A Review", *Membranes*, 12(6) (2022) 555.
[7] O.A. Hamadi and K.Z. Yahiya, "Optical and electrical properties of selenium-antimony heterojunction formed on silicon substrate", *Sharjah Univ. J. Pure Appl. Sci.*, 4(2) (2007) 1-11.
[8] M.I. Rahmah and E.T. Garallah, "Preparation of copper oxides/polyvinyl alcohol nanocoatings with antibacterial activity", *Chem. Data Collec.*, 39 (2022) 100869.
[9] S. Mehla et al., "Recent advances in preparation methods for catalytic thin films and coatings", *Catal. Sci. Technol.*, 9(14) (2019) 3582-3602.
[10] C.S. Gopinath and N. Nalajala, "A scalable and thin film approach for solar hydrogen generation: a review on enhanced photocatalytic water splitting", *J. Mater. Chem. A*, 9(3) (2021) 1353-1371.
[11] M.A. Basyooni, Y.R. Eker and M. Yilmaz, "Structural, optical, electrical and room temperature gas sensing characterizations of spin coated

 ISSN (print) 1813-2065, (online) 2309-1673 PRINTED IN IRAQ

multilayer cobalt-doped tin oxide thin films", *Superlat. Microstr.*, 140 (2020) 106465.
[12] J.M. Rzaij and N.F. Habubi, "Enhancing the CO_2 sensor response of nickel oxide-doped tin dioxide thin films synthesized by SILAR method", *J. Mater. Sci.: Mater. in Electron.*, 33(15) (2022) 11851-11863.
[13] O.A. Hamadi, "Characteristics of CdO-Si Heterostructure Produced by Plasma-Induced Bonding Technique", *Proc. IMechE, Part L, J. Mater.: Design & Appl.*, 222 (2008) 65-71.
[14] C.-L. Kuo and M.H. Huang, "The growth of ultralong and highly blue luminescent gallium oxide nanowires and nanobelts, and direct horizontal nanowire growth on substrates", *Nanotechnol.*, 19(15) (2008) 155604.
[15] Y.C. Zhang and G.L. Wang, "Solvothermal synthesis of CdO hollow nanostructures from CdO2nanoparticles", *Mater. Lett.*, 62(4-5) (2008) 673-675.
[16] O.A. Hamadi, "Effect of Annealing on the Electrical Characteristics of CdO-Si Heterostructure Produced by Plasma-Induced Bonding Technique", *Iraqi J. Appl. Phys.*, 4(3) (2008) 34-37.
[17] R. Ferro and J. Rodrıguez, "Influence of F-doping on the transmittance and electron affinity of CdO thin films suitable for solar cells technology", *Solar Ener. Mater. Solar Cells*, 64(4) (2000) 363-370.
[18] A. Srivastava et al., "Novel growth morphologies of nano-and micro-structured cadmium oxide", *Mater. Lett.*, 62(4-5) (2008) 727-730.
[19] Y. Wang et al., "Preparation and characterization of ordered semiconductor CdO nanowire arrays", *J. Mater. Sci. Lett.*, 20 (2001) 1687-1689.
[20] Z.W. Pan, Z.R. Dai and Z.L. Wang, "Nanobelts of semiconducting oxides", *Science*, 291(5510) (2001) 1947-1949.
[21] A. Askarinejad and A. Morsali, "Syntheses and characterization of $CdCO_3$ and CdO nanoparticles by using a sonochemical method", *Mater. Lett.*, 62(3) (2008) 478-482.
[22] M. Abood, E. Salim and J. Saimon, "Niobium pentoxide thin film prepared using simple colloidal suspension for optoelectronic application", *Int. J. Nanoelectro. Mater.*, 11(2) (2018) 127-134.
[23] E.T. Salim et al., "Some physical properties of Nb2O5 thin films prepared using nobic acid based colloidal suspension at room temperature", *Mater. Res. Exp.*, 4(10) (2017) 106407.
[24] A. Umar et al., "CdO–ZnO nanorices for enhanced and selective formaldehyde gas sensing applications", *Env. Res.*, 200 (2021) 111377.
[25] M. Abood, E. Salim and J. Saimon, "Optical investigations of Nb2O5 at different teamperatures for optoelectronic devices", *J. Ovonic Res.*, 15(2) (2019) 109-115.
[26] H.A. Komurcu et al., "Production of hydrogen gas sensors based on sol–gel spin-coated Nb2O5 thin films", *J. Mater. Sci.: Mater. in Electron.*, 34(10) (2023) 922.
[27] H. Liu et al., "Hexagonal-like Nb_2O_5 nanoplates-based photodetectors and photocatalyst with high performances", *Sci. Rep.*, 5(1) (2015) 7716.
[28] C.-J. Huang et al., "Growth and photoresponse study of PdO nanoflakes reactive-sputter deposited on SiO_2", *J. Appl. Phys.*, 108(5) (2010).
[29] W. Son et al., "PdO-Nanoparticle-Embedded Carbon Nanotube Yarns for Wearable Hydrogen Gas Sensing Platforms with Fast and Sensitive Responses", *ACS Sens.*, 8(1) (2023) 94-102.
[30] Y.-J. Chiang and F.-M. Pan, "PdO nanoflake thin films for CO gas sensing at low temperatures", *The J. Phys. Chem. C*, 117(30) (2013) 15593-15601.
[31] H. Gabasch et al., "Comparison of the reactivity of different Pd–O species in CO oxidation", *Phys. Chem. Chem. Phys.*, 9(4) (2007) 533-540.
[32] M.A. Fakhri et al., "Optical investigations of nano lithium niobate deposited by spray pyrolysis technique with injection of Li_2CO_3 and Nb_2O_5 as raw materials", *Int. J. Nanoelectro. Mater.*, 11(Special Issue BOND21) (2018) 103-108.
[33] J. Zhang, "Room-temperature compressibilities of MnO and CdO: further examination of the role of cation type in bulk modulus systematics", *Phys. Chem. Miner.*, 26 (1999) 644-648.
[34] S. Tamura, K. Kato and M. Goto, "Single crystals of T-Nb_2O_5 obtained by slow cooling method under high pressures", *Zeitsch. Anorgan. Allgem. Chemie*, 410(3) (1974) 313-315.
[35] A. Patterson, "The Scherrer formula for X-ray particle size determination", *Phys. Rev.*, 56(10) (1939) 978.
[36] M.I. Rahmah, "Novel triple hydrothermal method for preparation of $CuO/Fe_2O_3/Ag_2O$ nanocomposite with antimicrobial application", *Inorg. Nano-Metal Chem.*, (2023) 1-6.
[37] G. Levi and C. Fontana, "Ossidi di palladio", *Gazzetta Chimica Italiana*, 56 (1926) 388-396.
[38] J.M. Rzaij, A. Ibraheam and A.M. Abass, "Cobalt Effect on the Growth of Cadmium Oxide Nanostructure Prepared by Spray Pyrolysis Technique", *Baghdad Sci. J.*, 18(2) (2021) 401-408.
[39] S.K. Abdo and J.M. Rzaij, "Copper Molarity Effect on the Optical Properties of Cu_2CdSnS_4 Quaternary Thin Films", *Iraqi J. Sci.*, 62(5) (2021) 1513-1523.
[40] J.M. Marei et al., "Nitrogen Dioxide Gas Sensor of In_2O_3-ZnO Polyhedron Nanostructures Prepared by Spray Pyrolysis", *J. Nano Res.*, 70 (2021) 41-51.
[41] Q.A. Abduljabbar et al., "Spray rate effects on the NO_2 gas sensor properties of Ni-doped SnO_2 nanoflakes", *Eng. Res. Exp.*, 4(1) (2022) 015028.
[42] H.K. Webb et al., "Roughness parameters for standard description of surface nanoarchitecture", *Scanning*, 34(4) (2012) 257-263.
[43] B.E. Al-Jumaili, J.M. Rzaij and A. Ibraheam, "Nanoparticles of CuO thin films for room temperature NO_2 gas detection: Annealing time effect", *Mater. Today: Proc.*, 42 (2021) 2603-2608.

[44] R. Bari and S. Patil, "Nanostructured CdO thin films for LPG and CO_2 gas sensor prepared by spray pyrolisis technique", *Int. Lett. Chem. Phys. Astro.*, 18 (2014) 31-46.
[45] O.A. Hamadi, N.J. Shakir and F.H. Mohammed, “Magnetic Field and Temperature Dependent Measurements of Hall Coefficient in Thermal Evaporated Tin-Doped Cadmium Oxide Thin Films”, *Bulg. J. Phys.*, 37(4) (2010) 223-231.
[46] P. Sakthivel et al., "Influence of radiofrequency power on structural, morphological, optical and electrical properties of magnetron sputtered CdO: Sm thin films as alternative TCO for optoelectronic applications", *J. Alloys Comp.*, 765 (2018) 146-157.
[47] R. Bairy, S.D. Kulkarni and M. Murari, "Effect of Al doping on photoluminescence and laser stimulated nonlinear optical features of CdO nanostructures for optoelectronic device applications", *Opt. Laser Technol.*, 126 (2020) 106113.
[48] R. Bari, S. Patil and A. Bari, "Influence of precursor concentration solution on CO sensing performance of sprayed nanocrystalline SnO_2 thin films", *Optoelectro. Adv. Mater. Rapid Commun.*, 6 (2012) 887-895.
[49] L. Patil et al., "Detection of dimethyl methyl phosphonate–a simulant of sarin: The highly toxic chemical warfare–using platinum activated nanocrystalline ZnO thick films", *Sens. Actuat. B: Chem.*, 161(1) (2012) 372-380.
[50] R. Salunkhe et al., "Sprayed CdO thin films for liquefied petroleum gas (LPG) detection", *Sens. Actuat. B: Chem.*, 140(1) (2009) 86-91.

 ISSN (print) 1813-2065, (online) 2309-1673 PRINTED IN IRAQ

IRAQI JOURNAL OF APPLIED PHYSICS
Vol. 19, No. 4A, October 2023, pp. 13-20

Luma A. Jassim
Layla A. Jabor

Department of Chemistry,
College of Science,
Tikrit University,
Tikrit, IRAQ

Synthesis of Activated Carbon Nanoparticles from Date Seeds to Remove Malachite Green

In this study a dye (Malachite green) was prepared at a concentration of (80 mg/L), and a series of dilute solutions were prepared. Then prepare activated charcoal from Khastawi dates. The effect of several factors on adsorption was also calculated, including the impact of the amount of adsorbent, the effect of adsorption, the effect of contact time, the effect of the pH function, and the effect of volume. In addition, the Langmuir equation, the Temkin equation, the second-order equation on the isotherms, the second Freundlich equation, the isotherm, and thermodynamics were calculated.

Keywords: Adsorption; Malachite Green; Activated Carbon; Nanoparticles
Received: 19 April 2023; **Revised:** 02 June 2023; **Accepted:** 09 June 2023

1. Introduction

One of the most well-liked and often-used adsorbents for water and wastewater treatment worldwide is activated carbon (AC) [1]. The first adsorbent for water filtration is charcoal, the precursor to current-activated carbon [2]. In 1773, Scheele made the initial discovery of the specific adsorptive properties of charcoal for the treatment of gases [3]. Two years later, in 1786, he made the same discovery for decolorizing solutions. Scheele also gave the first comprehensive account of the adsorptive power of charcoal in the liquid phase [4,5]. From 1789 to 1790, Lowitz invented charcoal to eliminate unpleasant tastes and odors from water. The Swedish scientist von Ostreijko is credited with creating commercial activated carbon. In 1900 and 1901, he was granted two patents that covered the fundamental ideas of chemical and thermal (or physical) activation of carbon using metal chlorides and carbon dioxide and steam, respectively [6]. The first industrial-scale chemical activation of sawdust with zinc chloride took place at an Austrian facility in Aussing in 1914 and in the Bayer dye plant in 1915 [7]. In this activation, the carbonaceous material was heated by pyrolysis and exposed to dehydrating agents like zinc chloride or phosphoric acid [8]. The phrase "activated carbon" refers to carbon-based materials with established internal pore systems. AC is created from carbonaceous-rich materials such as wood, coal, lignite and coconut shell [9]. Because of its high surface area, high porosity, well-developed internal pore structure made up of micro-, meso-, and macropores, and a broad range of functional groups on its surface, alumina ceramic (AC) is a flexible material with a wide range of uses, mostly in the environmental sector. The most common forms of oxygen, hydrogen, sulfur, and nitrogen in AC are functional groups and atoms chemically connected to the structure. The primary functional groups in the carbon structure commonly thought to be involved in the absorption of contaminants include carboxyl, carbonyl, phenols, lactones, quinones, and others. The distinctive adsorption characteristics of AC may be considerably influenced by these functional groups [4]. The activation procedure, precursor(s), heat treatment, and post-chemical treatment are the key sources of the functional groups on the carbon surface. To enhance the effectiveness of AC for the removal of certain pollutants, sensible heat or chemical treatments may change the type and concentration of surface functional groups. It has been widely shown that ACs are effective adsorbents for various contaminants [10]. Removing organic molecules with activated carbon has been far more effective than removing metals and other inorganic contaminants. By using various chemicals or practical treatment techniques, efforts are being made to significantly boost the potential of carbon surfaces [11], enhancing AC's capacity to remove certain pollutants from the aqueous phase. Many techniques, such as activation conditions (different agents, temperature, and duration of the process), precursors, additions, etc., might modify carbon's physical and chemical structure [12]. Several kinds of AC surface modification have been documented in the literature [13–17], which provide information on the chemistry and mechanism of the treatment approaches that allow for greater absorption of certain contaminants. Typically, the activation phase is followed by the surface modification of AC. Three types of alteration exist chemical, physical, and biological. Chemical modification is the first kind of modification. In addition, both oxidative [18] and non-oxidative [19] techniques for treating the surface of AC have been documented in the literature. Widely varying complexing groups, such as carboxylic, lactonic, and phenolic, have been studied on AC surfaces [20]. Understanding the many elements that affect the adsorption potential of AC is crucial before making any modifications. It will make modifying their

physical and chemical properties easier to improve their propensities for certain contaminants in an aqueous solution. The preliminary results of different modification techniques used with AC have been evaluated and addressed in this study. Readers are directed to the complete publications in the sources for information on the experimental approach and conditions [21]. Dye removal uses activated carbons [22,23]. A synthetic dye called malachite green (MG) colors silk, wool, leather, cotton, or paper. The treatment of fungus infections in fish eggs has a long history. Nevertheless, several negative consequences have been linked to the use of this dye owing to its teratogenic, mutagenic, genotoxic, and carcinogenic characteristics in animal studies [24]. Because of this, carbon-based adsorbents have been used to remove malachite green from the aqueous solution. These materials may be made by pyrolyzing various wastes and activating them with phosphoric acid and sodium hydroxide [25] or by chemically activating lignite with KOH [26]. Nevertheless, prior studies conducted by our research team have shown the significance of choosing suitable precursors and pyrolysis conditions [27] for the low-cost and environmentally friendly synthesis of carbon-based adsorbents without needing external chemical activation. Malachite green (MG) needs to be removed from an aqueous solution, and the current work seeks to investigate the adsorption capacity of carbon-based adsorbents generated by pyrolysis of waste products from the paper industry (WMPI) and pine bark (PB) [28]. Activated carbon is used in a wide range of applications, including the storage of methane and hydrogen [29], air purification, capacitive deionization, super capacitive swing adsorption [30], solvent recovery, decaffeination, gold purification, metal extraction, water purification, medicine, sewage treatment, air filters in respirators, compressed air filters, teeth whitening, the production of hydrogen chloride, and edible electronics [31]. One of its main industrial uses is using activated carbon in metal finishing to purify electroplating solutions. The direct purification method, for instance, is used to eliminate organic contaminants from brilliant nickel-plating solutions [32]. Various organic compounds are added to increase the deposit characteristics of plating solutions and enhance features like brightness, smoothness, flexibility, etc. [33]. Organic additives produce undesirable breakdown products in the solution due to the flow of direct current and electrolytic reactions of anodic oxidation and cathodic reduction [34]. Its excessive accumulation may hurt the deposited metal's plating quality and physical characteristics [35]. Such contaminants are eliminated by activated carbon treatment, which also restores plating performance to the required level [36]. Upon oral intake, activated carbon is used to treat poisonings and overdoses. Several nations utilize tablets or capsules of activated carbon as an over-the-counter medication to treat diarrhea, indigestion, and flatulence [37]. Nevertheless, intestinal gas and diarrhea are unaffected by activated charcoal [38]. It is often medically useless if poisoning is brought on by consuming caustic substances, boric acid, or petroleum products. It is sensitive to poisoning by cyanide, iron, lithium, arsenic, methanol, ethanol, and ethylene glycol in solid acids and bases [39]. These compounds won't be stopped from entering the body by activated carbon. It is included in the WHO's list of essential medications [40].

2. Experimental Part

The materials used in this work include malachite green (M.G.) and activated charcoal as adsorbent surfaces, HCl, NaCl, Na_2CO_3, and NaOH. According to published procedure [41,42], a dye (malachite green) was prepared at a concentration of 80 mg/L by dissolving 80 mg in one liter (1000 mL) of distilled water, and a series of dilute solutions were prepared. In order to prepare activated charcoal, a 20g of $ZnCl_2$ was dissolved in 100 mL of distilled water. A 50g of date stones (Khastawi dates from the Hawija region) was soaked in this solution for three days at a temperature of 80-90°C and a boiling stone was added to distribute the heat. After soaking, the material was burnt at a temperature of 550°C for three hours, then washed with HCl acid at a concentration of 1 M. Then the material was soaked in HCl acid solution of 10 M concentration for 24 hours, then filtered and washed until it the pH value was 7. Then it was dried in the oven for four hours at a temperature of 100°C. After that, the material was grinded until it became as a powder. This procedure was presented by [43,44].

3. Results and Discussion

The effect of adsorbent weight on the removal efficiency of M.G. of aqueous solutions was studied at a constant temperature and a constant time, and we have several variables, where six weights were taken (0.02, 0.016, 0.013, 0.01, 0.007, 0.004) [45], as shown in table (1), where the ideal weight was (0.013) g / liter to give it the highest absorption, equal to 95.7.

Table (1) Effect of adsorbent weight on adsorption of M.G. dye from aqueous solutions

Dye	Dose (g/L)	Abs	C_o (mg/L)	Qe (mg/g)	Adsorption efficiency
	Before adsorption	1.000	80.00	0	0
	0.020	0.045	3.60	47.75	95.5
M.G	0.016	0.043	3.44	47.85	95.7
Co=80	0.013	0.048	3.84	47.60	95.2
	0.010	0.050	4.00	47.50	95.0
	0.007	0.065	5.20	46.75	94.5
	0.004	0.076	6.08	46.20	92.5

The study was done by taking four different variable solutions (NaCl, HCl, Na_2CO_3, NaOH), as shown in table (2), where the variables for each solution appeared.

 ISSN (print) 1813-2065, (online) 2309-1673

Table (2) The effect of changing solutions on the dye of malachite green from aqueous solutions

Dye	Solution	Abs	C_o (mg/L)	Qe (mg/g)	%
M.G Co=80	NaCl	0.124	9.92	350.4	87.6
	HCl	0.106	8.48	357.6	89.4
	Na_2CO_3	0.214	17.12	314.4	78.6
	NaOH	0.113	9.04	354.8	88.7

The equilibrium time was studied on the adsorption process of green malachite dye as in table (3) and figure (1), where thirteen times were studied, which are 0, 5, 10, 15, 20, 25, 30, 45, 60, 90, 120, 150, and 180 minutes. The highest percentage of dye removal from the aqueous solution was found at (30 minutes), with an absorbance value of 340.4, the adsorption capacity, and adsorption efficiency of 85.1, which is the best contact time found to remove the dye from aqueous solutions.

Table (3) The effect of equilibration time on the removal of M.G. from aqueous solutions

Dye	Time	C_o (mg/L)	Qe (mg/g)	Adsorption efficiency	Abs
M.G 80	0	80.00	0	0	1.000
	5	18.00	310.0	77.5	0.225
	10	16.96	315.2	78.8	0.212
	15	14.48	327.6	81.9	0.181
	20	22.84	340.8	85.2	0.148
	25	10.64	346.8	86.7	0.133
	30	11.92	340.4	85.1	0.149
	45	12.08	339.6	84.9	0.151
	60	14.40	328.0	82.0	0.180
	90	12.08	339.6	84.9	0.151
	120	8.24	358.8	89.7	0.103
	150	11.84	340.8	85.2	0.148
	180	14.00	330.0	82.5	0.175

The effect of the pH function on the adsorption process was studied within the range (of 3-11) pH for green malachite dye in aqueous solutions and at a temperature of 25°C (pH=7), equal to 94.5, and at pH=3, similar to 94.5, meaning that the dye tends to the acidic medium because of the repulsion between the positive charge of the dye, the amount of the extra proton ions, and the positive direction of the surface, as shown in table (4).

Table (4) The effect of pH on the adsorption of M.G. dye from aqueous solutions

Dye	Ph	Abs	Ce	qe	%
M.G Co=80	3	0.079	6.32	368.4	92.1
	5	0.069	5.52	379.4	93.1
	7	0.055	4.40	378.0	94.5
	9	0.057	4.56	377.2	94.3
	11	0.055	4.40	378.0	94.5

The effect of volume was studied by taking several different volumes, which are 250, 150, 75, 50, 25, and 10 ml of solutions to the green malachite dye, where several results were obtained as shown in table (5) and the best volume was 25 ml [46].

Table (5) Effect of size on the dye of malachite green in aqueous solutions

Dye	Volume	Abs	C_o (mg/L)	Qe (mg/g)	%
M.G Co=80	250	0.780	62.40	88.0	22.0
	150	0.570	45.60	172.0	43.0
	75	0.490	39.20	204.0	51.0
	50	0.132	10.56	347.2	86.8
	25	0.118	9.44	352.8	88.2
	10	0.268	21.44	292.8	73.2

The effect of temperature change on the adsorption of green malachite dye was studied, where a range of temperatures was taken (20, 25, 30, and 35°C), as shown in table (6) and Fig. (2).

The values of the thermodynamic functions for the change of interactions in the adsorption process give information about the adsorbent material. The adsorbent surface and the nature of the force in the adsorption through knowledge of the enthalpy (ΔH) that was measured from the Vant Hoff equation as in table (7) and Fig. (3), which gave Negative values for enthalpy, entropy, and free energy, endothermic, and thus the adsorption is physical. Table (7) shows the values of the maximum adsorption quantities (lnK) and the different temperatures (T) for the green malachite formula [47].

$$K=\frac{qe*w(g)}{Ce*V\ (L)}$$

$$K_{293}=\frac{337.6*0.015}{12.48*0.05} \rightarrow K=8.115 \quad \text{and}$$

$$K_{298}=\frac{348.4*0.015}{10.32*0.05} \rightarrow K=10.127$$

$$K_{303}=\frac{372*0.015}{5.6*0.05} \rightarrow K=19.92 \quad \text{and}$$

$$K_{308}=\frac{374.4*0.015}{5.12*0.05} \rightarrow K=21.937$$

$$\Delta G=\Delta H-T\Delta S \rightarrow \Delta S=\frac{\Delta H}{T}$$

The study of the adsorption kinetics of the green malachite dye was at a fixed concentration of 0.013 for the adsorbent and 0.08 for the green malachite and a range of temperatures (20-35°C) and at different times, as shown in table (8) and Fig. (4), and the false first-order equation was applied. Calculating the second-order equation on isotherms Y=0.0037X-0.0031 [48].

Table (8) The values of the pseudo-first- and second-order equations, or the so-called pseudo-first-order, for the adsorption of M.G. dye from aqueous solutions

t	293 t/qt	298 t/qt	303 t/qt	308 t/qt
5	0.020	0.022	0.013	0.015
15	0.040	0.053	0.041	0.048
25	0.120	0.125	0.069	0.071
35	0.115	0.102	0.095	0.096
45	0.163	0.148	0.124	0.125
55	0.183	0.169	0.150	0.148
65	0.192	0.197	0.174	0.173
70	0.240	0.246	0.193	0.192
75	0.290	0.288	0.210	0.209
80	0.345	0.215	0.215	0.212

The results obtained from the different isotherms (Langmuir, Temkin, Freundlich) are of great importance because they clarify the particles and their

distribution between the phases. Here, the study was done on the green malachite dye by taking different concentrations (5-80) [49], as shown in table (9), and different temperatures (20, 25, 30, and 35°C) and the acidity function (pH = 7) as in tables (10-12), and figures (5-8).

Calculation of the Langmuir equation for malachite green $\frac{C_e}{q_r} = \frac{1}{q_{max}\, K_L} + \frac{C_e}{q_{max}}$

Calculation of the Freundlich equation for malachite green lnqe= ln Kf + 1/n lnCe

Calculation of the Temkin equation for malachite green $qe = b_T \ln K_T + b_T \ln Ce$

Table (9) Langmuir isotherm values for adsorption of malachite dye from aqueous solutions

293		298		303		308	
Ce	Ce/qe	Ce	Ce/qe	Ce	Ce/qe	Ce	Ce/qe
36.88	0.109	35.20	0.101	7.04	0.0189	15.28	0.040
38.40	0.113	32.80	0.099	7.76	0.0200	9.28	0.024
38.64	0.114	33.92	0.097	8.24	0.0210	10.00	0.026
19.52	0.057	19.76	0.056	7.04	0.0180	7.12	0.019
24.80	0.073	26.40	0.075	7.76	0.0200	8.08	0.021
20.00	0.059	19.60	0.056	7.12	0.0180	5.92	0.015
12.48	0.036	12.64	0.036	5.60	0.0130	5.12	0.013
21.68	0.002	23.12	0.066	7.52	0.0190	7.20	0.019
28.40	0.084	28.16	0.080	8.64	0.0220	8.24	0.022
33.68	0.099	10.32	0.002	5.84	0.0150	4.88	0.002

Table (10) Temkin isotherm values for adsorption of malachite dye from aqueous solutions

293		298		303		308	
qe	lnCe	qe	lnCe	qe	lnCe	qe	lnCe
215.6	3.60	224.0	3.56	364.8	1.95	323.6	6.57
208.0	3.64	280.0	3.49	361.2	2.04	307.2	2.22
206.8	3.65	206.8	3.52	358.8	2.10	350.0	2.30
202.9	3.97	302.4	2.98	364.8	1.95	364.4	1.96
276.0	3.21	276.0	3.27	361.2	2.04	359.6	2.08
300.0	2.99	300.0	2.97	364.4	1.96	370.4	1.77
337.6	2.52	337.6	2.53	372.0	1.72	374.4	1.63
291.6	3.07	291.6	3.14	362.4	2.01	364.0	1.97
258.0	3.34	259.2	3.33	356.8	2.15	358.8	2.10
231.6	3.51	348.4	2.33	370.8	1.76	375.6	1.58

Table (11) Freundlich isotherm values for adsorption of malachite dye from aqueous solutions

293		298		303		308	
lnCe	lnqe	lnCe	lnqe	lnCe	Lnqe	lnCe	lnqe
3.60	5.373	3.56	5.411	1.95	5.89	6.57	5.770
3.64	5.337	3.49	5.634	2.04	5.889	2.22	5.720
3.65	5.331	3.52	5.331	2.10	5.882	2.30	5.857
2.97	5.710	2.98	5.711	1.95	5.899	1.96	5.898
3.21	5.620	3.27	5.620	2.04	5.899	2.08	5.670
2.99	5.700	2.97	5.700	1.96	5.898	1.77	5.910
2.52	5.820	2.53	5.820	1.72	5.910	1.63	5.920
3.07	5.670	3.14	5.670	2.01	5.892	1.97	5.890
3.34	5.550	3.33	5.550	2.15	5.877	2.10	5.880
3.51	5.440	2.33	5.850	1.76	5.915	1.58	5.920

The XRD of activated charcoal nanoparticles was measured, and the particle size, according to the Scherrer's equation, was 1.05 nm. These results are consistent with what has been published in previous studies [1], as shown in Fig. (9).

As for the SEM measurement, it is the best that has been prepared so far, as it contains nanochannels and nanoslits and is characterized by periodic nanostructures and sizes mentioned in Fig. (10). In addition to this, the material has a nano-chip structure, which provides a very high surface area. In addition to this, the material has micro spacing between particles. From this, we can predict that the adsorption will be very effective.

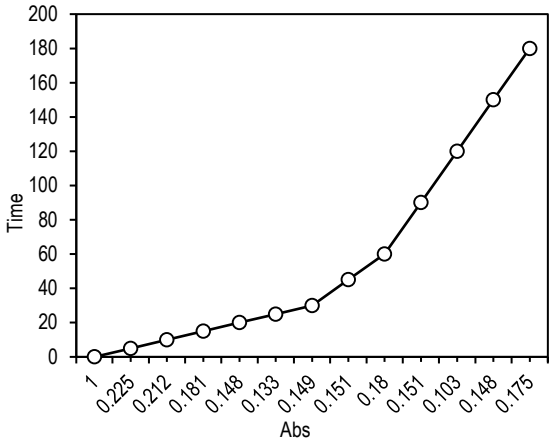

Fig. (1) The effect of equilibration time on the removal of M.G. from aqueous solutions

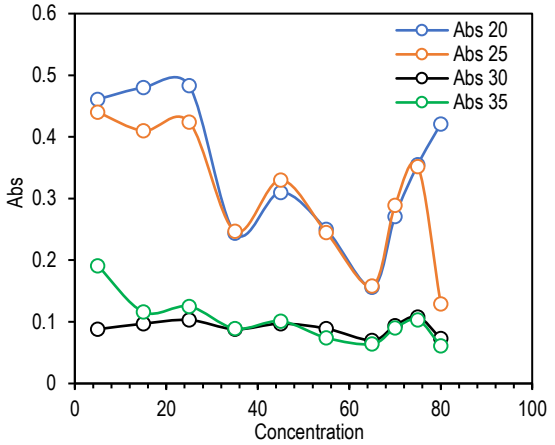

Fig. (2) The effect of temperature on the adsorption capacity of M.G. dye in aqueous solutions

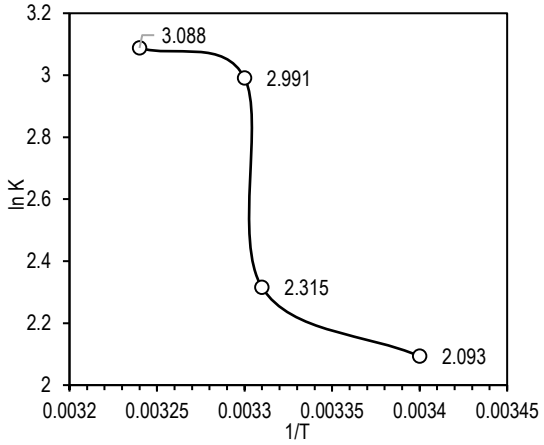

Fig. (3) The values of the thermodynamic functions

 ISSN (print) 1813-2065, (online) 2309-1673

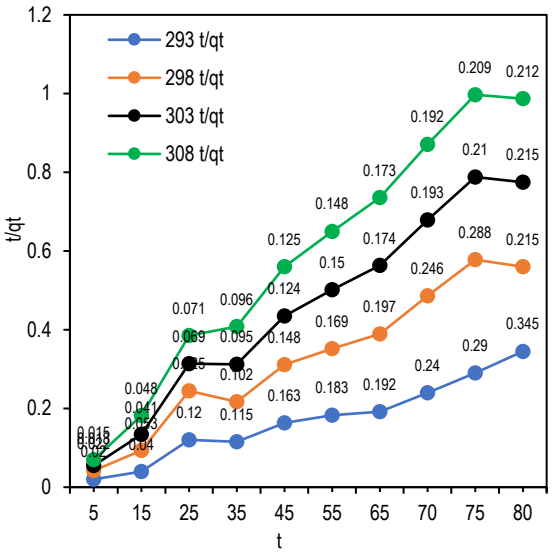

Fig. (4) The values of the pseudo-first- and second-order equations, or the so-called pseudo-first-order, for the adsorption of M.G. dye from aqueous solutions

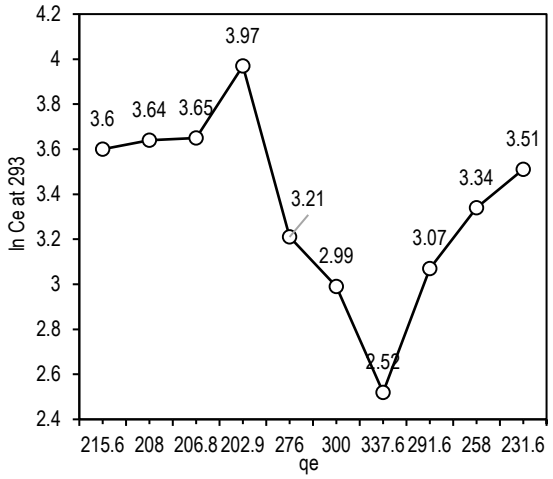

Fig. (5) Temkin isotherm values at 293°C

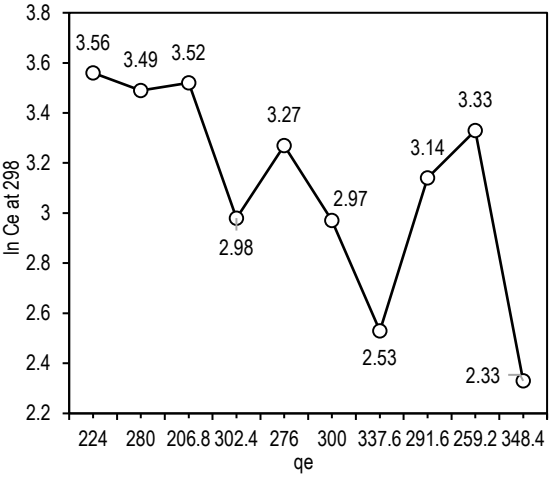

Fig. (6) Temkin isotherm values at 298°C

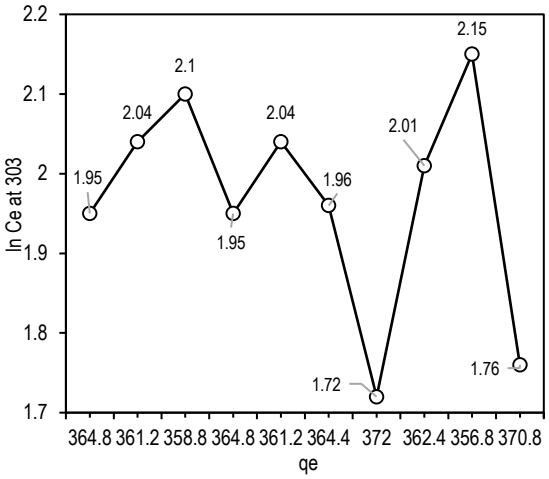

Fig. (7) Temkin isotherm values at 303°C

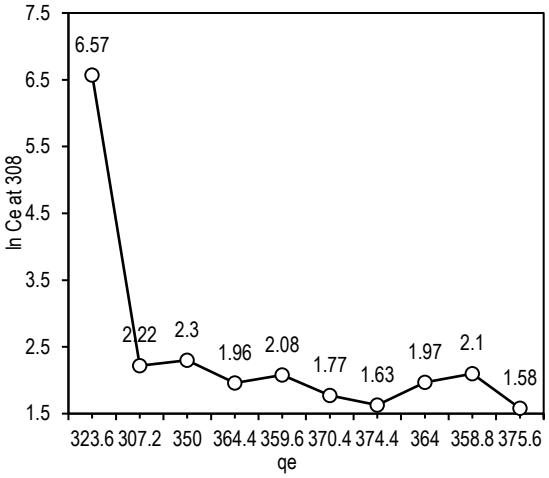

Fig. (8) Temkin isotherm values at 308°C

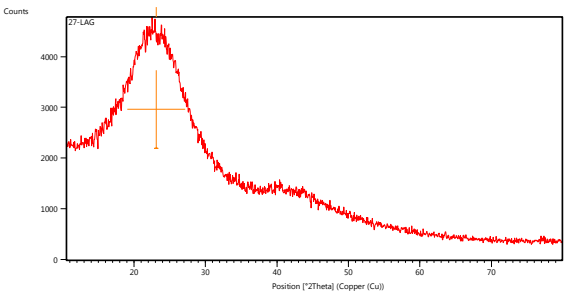

Fig. (9) XRS of activated charcoal nanoparticles

4. Conclusions

A dye (Malachite green) was prepared in this study, then activated charcoal was prepared from Al-Khastawi dates. The effect of several factors on the dye removal efficiency was also calculated, including the impact of the amount of adsorbent, the ideal weight was (0.013) g/L, the effect of changing the solution, and the development of contact time. The highest percentage of dye removal from the aqueous solution was found at (30 minutes) and the absorbance value (340.4), adsorption capacity, and adsorption efficiency (85.1), which is the best contact time found to remove the dye from aqueous solutions, and the effect of pH, where the highest percentage of

absorbance appeared at pH=7, equal to 94.5, and pH=3, similar to 94.5, meaning that the dye tends to the medium acid due to the repulsion between the positive charge of the dye, the amount of the extra proton ions, and the positive direction of the surface, and the effect of volume, and the best volume was (25) ml. Thermodynamics was also studied, which gave negative values for enthalpy, entropy, and free energy, endothermic; thus, the adsorption is physical. The adsorption kinetics was calculated, and the false first-order equation was applied. Adsorption isotherms were studied, and it was found that adsorption behaves like a theory that can be given to adsorption as high as possible and equal to (0.9943).

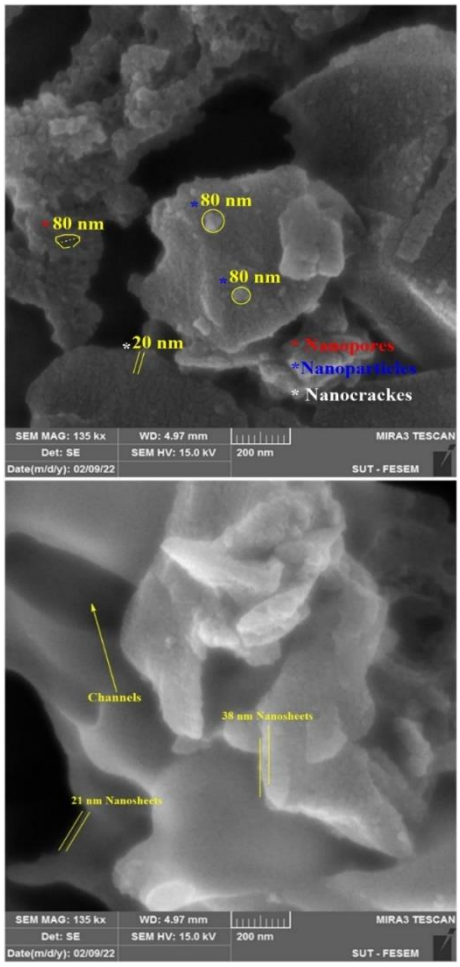

Fig. (10) SEM images of activated charcoal nanoparticles

References

[1] I. Uzun and F. Güzel, "Adsorption of some heavy metal ions from aqueous solution by activated carbon and comparison of percent adsorption results of activated carbon with those of some other adsorbents", *Turk. J. Chem.*, 24(3) (2000) 291-298.

[2] N.J. Wagner and R.J. Jula, "Activated carbon adsorption", in *Activated carbon adsorption for wastewater treatment*, CRC Press (2018) 41-60.

[3] H. Marsh and F. Rodriguez-Reinonso, **"Activated Carbon"**, Elsevier Science & Technology Books (Amsterdam, 2006), 89-100.

[4] Bansal, R. C., & Goyal, M. (2005). *Activated carbon adsorption*. CRC press.

[5] T.J. Bandosz and and C.O. Ania, "Surface chemistry of activated carbons and its characterization", in *Interface Science and Technology*, Elsevier, vol. 7 (2006) 159-229.

[6] H. Sontheimer, J.C. Crittenden and R.S. Summers, "Activated Carbon for Water Treatment", University of Karlsruhe (1988).

[7] A. Dąbrowski, "Adsorption—from theory to practice", *Adv. Colloid Interface Sci.*, 93(1-3) (2001) 135-224.

[8] P.J. Purcell, "Milestones in the development of municipal water treatment science and technology in the 19th and early 20th centuries: part I", *Water Env. J.*, 19(3) (2005) 230-237.

[9] J.T. Cookson, P.N. Cheremishinoff and F. Eclerbusch, **"Carbon Adsorption Handbook"**, Michigan: Ann Arbor Science Publishers (1978).

[10] R.T. Yang, **"Adsorbents: fundamentals and applications",** John-Wiley & Sons (2003).

[11] L. Monser and N. Adhoum, "Modified activated carbon for the removal of copper, zinc, chromium and cyanide from wastewater", *Separ. Purif. Technol.*, 26(2-3) (2002) 137-146.

[12] P. Pietrowski, I. Ludwiczak and J. Tyczkowski, "Activated carbons modified by Ar and CO_2 plasmas–acetone and cyclohexane adsorption", *Mater. Sci.*, 18(2) (2012) 158-162.

[13] J. Lee, J. Kim and T. Hyeon, "Recent progress in the synthesis of porous carbon materials", *Adv. Mater.*, 18(16) (2006) 2073-2094.

[14] C.Y. Yin, M.K. Aroua and W.M.A. Daud, "Review of modifications of activated carbon for enhancing contaminant uptakes from aqueous solutions", *Separ. Purif. Technol.*, 52(3) (2007) 403-415.

[15] J. Rivera-Utrilla et al., "Activated carbon modifications to enhance its water treatment applications. An overview", *J. Hazard. Mater.*, 187(1-3) (2011) 1-23.

[16] M.S. Shafeeyan et al., "A review on surface modification of activated carbon for carbon dioxide adsorption", *J. Anal. Appl. Pyrol.*, 89(2) (2010) 143-151.

[17] J.M. Dias et al., "Waste materials for activated carbon preparation and its use in aqueous-phase treatment: a review", *J. Env. Manag.*, 85(4) (2007) 833-846.

[18] M. Santiago et al., "Modified activated carbons for catalytic wet air oxidation of phenol", *Carbon*, 43(10) (2005) 2134-2145.

[19] S. Sato et al., "Influence of activated carbon surface acidity on adsorption of heavy metal

 ISSN (print) 1813-2065, (online) 2309-1673

ions and aromatics from aqueous solution", *Appl. Surf. Sci.*, 253(20) (2007) 8554-8559.
[20] V.L. Snoeyink and W.J. Weber, "The surface chemistry of active carbon; a discussion of structure and surface functional groups", *Env. Sci. Technol.*, 1(3) (1967) 228-234.
[21] A. Üçer, A. Uyanik and Ş.F. Aygün, "Adsorption of Cu (II), Cd (II), Zn (II), Mn (II) and Fe (III) ions by tannic acid immobilised activated carbon", *Separ. Purif. Technol.*, 47(3) (2006) 113-118.
[22] Y. Al-Degs et al., "Effect of carbon surface chemistry on the removal of reactive dyes from textile effluent", *Water Res.*, 34(3) (2000) 927-935.
[23] A.K. Jain, V.K. Gupta and A. Bhatnagar, "Utilization of industrial waste products as adsorbents for the removal of dyes", *J. Hazard. Mater.*, 101(1) (2003) 31-42.
[24] S.J. Culp et al., "Toxicity and metabolism of malachite green and leucomalachite green during short-term feeding to Fischer 344 rats and B6C3F1 mice", *Chemico-biol. Interact.*, 122(3) (1999) 153-170.
[25] I.A. Rahman et al., "Adsorption characteristics of malachite green on activated carbon derived from rice husks produced by chemical–thermal process", *Biores. Technol.*, 96(14) (2005) 1578-1583.
[26] Y. Önal, C. Akmil-Başar and Ç. Sarıcı-Özdemir, "Investigation kinetics mechanisms of adsorption malachite green onto activated carbon", *J. Hazard. Mater.*, 146(1-2) (2007) 194-203.
[27] G. Gascó et al., "The influence of organic matter on sewage sludge pyrolysis", *J. Anal. Appl. Pyrol.*, 74(1-2) (2005) 413-420.
[28] A. Méndez et al., "Preparation of carbon-based adsorbents from pyrolysis and air activation of sewage sludges", *Chem. Eng. J.*, 108(1-2) (2005) 169-177.
[29] N. Chada et al., "Activated carbon monoliths for methane storage", in *APS March Meeting Abstracts* (vol. 2012, pp. W33-012).
[30] Y. Soo et al., "Adsorbed methane film properties in nanoporous carbon monoliths", in *APS March Meeting Abstracts* (vol. 2013, pp. M38-001).
[31] K.A. Marill et al., "Prospective, randomized trial of template-assisted versus undirected written recording of physician records in the emergency department", *Annals Emerg. Med.*, 33(5) (1999) 500-509.
[32] P.J. Paul, "Value Added Products from Gasification–Activated Carbon", *Bangalore: The Combustion, Gasification and Propulsion Laboratory (CGPL) at the Indian Institute of Science (IISc)* (2002).
[33] J. Lehmann and S. Joseph, "Biochar for environmental management: an introduction", in *Biochar for Enviro. Manag.*, (Routledge, 2015) 1-13.
[34] J. Xia et al., "A review on adsorption mechanism of gold cyanide complex onto activation carbon", *J. Indust. Eng. Chem.*, (2022).
[35] G. Oliveira et al., "Paper pulp-based adsorbents for the removal of pharmaceuticals from wastewater: a novel approach towards diversification", *Sci. Total Env.*, 631 (2018) 1018-1028.
[36] P. Cataldi et al., "An electrically conductive oleogel paste for edible electronics", *Adv. Func. Mater.*, 32(23) (2022) 2113417.
[37] World Health Organization, *World Health Organization model list of essential medicines: 21st list 2019* (No. WHO/MVP/EMP/IAU/2019.06).
[38] K.A. Adegoke et al., "Modification of cellulosic material for rapid dyeability with malachite green dye", *Sci. African*, (2022) e01138.
[39] M. Rajabi, K. Mahanpoor and O. Moradi, "Preparation of PMMA/GO and PMMA/GO-Fe_3O_4 nanocomposites for malachite green dye adsorption: kinetic and thermodynamic studies", *Composites Pt. B: Eng.*, 167 (2019) 544-555.
[40] Y.K. Alasadi et al., "Synthesis, Characterization, and Molecular Docking of New Tetrazole Derivatives as Promising Anticancer Agents", *J. Pharmaceut. Neg. Results*, 13(3) (2022) 513-522.
[41] A.M. Abdullah, L.H. Alwan and A.M. Abdulqader, "Thermodynamic and kinetic studies of Eriochrome black adsorption on activated charcoal prepared from lemon leaves", *Mater. Res. Exp.*, 6(12) (2020) 1250h8.
[42] M.A. Toma et al., "Study the adsorption of cyclopentanone on to natural polymers", *AIP Conf. Proc.*, 2394(1) (2022) 040007.
[43] A.S. Ahmed et al., "High surface area activated charcoal for water purification", *J. Compos. Sci.*, 6(10) (2022) 311.
[44] A.H. Dalaf et al., "Synthesis, Characterization, Biological Evaluation, and Assessment Laser Efficacy for New Derivatives of Tetrazole", *Key Eng. Mater.*, 911 (2022) 33-39.
[45] A.H. Dalaf, F.H. Jumaa and I.A. Yass, "Synthesis, characterization, biological evaluation, molecular docking, assess laser efficacy, thermal performance and optical stability study for new derivatives of bis-1, 3-oxazepene and 1, 3-diazepine", *AIP Conf. Proc.*, 2394(1) (2022) 040037.
[46] Y.K. Alasadi, F.H. Jumaa and A.H. Dalaf, "Synthesis, identification, antibacterial activity and laser effect of new derivatives of bis-1, 3-oxazepene-4, 7-dione and 1, 3-diazepine-4, 7-

dione", *AIP Conf. Proc.*, 2394(1) (2022) 040019.
[47] A.M. Hamad et al., "Green synthesis of copper nanoparticles using strawberry leaves and study of properties, anti-cancer action, and activity against bacteria isolated from Covid-19 patients", *Karbala Int. J. Mod. Sci.*, 9(1) (2023) 12.
[48] M.M. Aftan et al., "Impact para position on rho value and rate constant and study of liquid crystalline behavior of azo compounds", *Mater. Today: Proc.*, 45 (2021) 5529-5534.
[49] M.M. Aftan et al., "Application of biological activity of oxazepine and 2-azetidinone compounds and study of their liquid crystalline behavior", *Mater. Today: Proc.*, 43 (2021) 2040-2050.

Table (6) The effect of temperature on the adsorption capacity of M.G. dye in aqueous solutions

Concentration	20				25			
	Abs	%	qe	Ce	Abs	%	Qe	Ce
5	0.461	53.9	215.6	36.88	0.440	56.0	224.0	35.20
15	0.480	52.0	208.0	38.40	0.410	59.0	280.0	32.80
25	0.483	51.7	206.8	38.64	0.424	57.6	206.8	33.92
35	0.244	75.6	302.9	19.52	0.247	75.3	302.4	19.76
45	0.310	69.0	276.0	24.80	0.330	67.0	276.0	26.40
55	0.250	75.0	300.0	20.00	0.245	75.5	300.0	19.60
65	0.156	84.4	337.6	12.48	0.158	84.2	337.6	12.64
70	0.271	72.9	291.6	21.68	0.289	71.1	291.6	23.12
75	0.355	64.5	258.0	28.40	0.352	64.8	259.2	28.16
80	0.421	57.9	231.6	33.68	0.129	87.1	348.4	10.32
Concentration	**30**				**35**			
	Abs	**%**	**qe**	**Ce**	**Abs**	**%**	**Qe**	**Ce**
5	0.088	91.2	364.8	7.04	0.191	80.9	323.6	15.28
15	0.097	90.3	361.2	7.76	0.116	88.4	307.2	9.28
25	0.103	89.7	358.8	8.24	0.125	87.5	350.0	10.00
35	0.088	91.2	364.8	7.04	0.089	91.1	364.4	7.12
45	0.097	90.3	361.2	7.76	0.101	89.9	359.6	8.08
55	0.089	91.9	364.4	7.12	0.074	92.6	370.4	5.92
65	0.070	93.0	372.0	5.60	0.064	93.6	374.4	5.12
70	0.094	90.6	362.4	7.52	0.090	91.0	364.0	7.20
75	0.108	89.2	356.8	8.64	0.103	89.7	358.8	8.24
80	0.073	92.7	370.8	5.84	0.061	93.1	375.6	4.88

Table (7) The values of the thermodynamic functions

T	1/T	K	lnk	ΔH (J)	ΔS (K.J)	ΔG (J)
293	0.00340	8.115	2.093	-7012.4	-0.023900	-7019.4000
298	0.00331	10.127	2.315		-0.023500	-7014.4119
303	0.00330	19.92	2.991		-0.023143	-7019.4120
308	0.00324	21.937	3.088		-0.022767	-7012.4220

Table (12) Isothermal variables for each of Langmuir, Freundlich and Temkin the adsorption capacity of malachite green from aqueous solutions

C	Freundlich			Langmuir			Temkin		
	Kf	n	R_2	Q_{max}	Kt	R_2	B_T	K_T	R_2
20	0.4631	7.0603	0.9400	0.0199	0.0034	0.73	0.0078	5.3133	0.9687
25	0.3435	6.6988	0.7600	0.0167	0.0034	0.94	0.0085	5.5202	0.8277
30	0.0825	6.0564	0.9200	0.0017	0.0028	0.96	0.0284	12.2800	0.9943
35	0.0116	5.6155	0.0006	0.0047	0.0031	0.89	0.0383	16.0170	0.3391

 ISSN (print) 1813-2065, (online) 2309-1673

IRAQI JOURNAL OF APPLIED PHYSICS
Vol. 19, No. 4A, October 2023, pp. 21-28

Bushra A. Hasan
Hiba H. Issa
Ahmad A. Hasan

Department of Physics, College of Science, University of Baghdad, Baghdad, IRAQ

Fabrication and Investigation of Structural, Optical and Dielectric Properties of ZnO:MnO_2 Composites

In this work, $(ZnO)_{1-x}(MnO_2)_x$ compounds were synthesized with composition (x=0, 0.1, 0.2, 0.3, 0.4, and 0.5) of manganese oxide content using solid state reaction. Thin films were prepared from these compounds on glass substrates at room temperature using pulsed laser deposition method. The structure of the prepared compounds and thin films were analyzed using x-ray diffraction while the optical properties was measured using UV-visible spectrophotometry. It was found that the synthesized composites declared many peaks in the diffraction pattern which indicate polycrystalline structure with hexagonal wurtzite hexagonal structure of ZnO, and MnO_2 and Mn_2O_3 secondary phases. A narrowing in the optical energy gap was found as Mn content increases up to 0.4 and then a blue shift was observed for residual x value. The optical constants were reduced as Mn was introduced to ZnO and then they got to grow up. The dependencies of the a.c. conductivity, dielectric constant and tangent loss on angular frequency and Mn content were explored. Good correlation was observed between the structural optical and electrical properties.

Keywords: ZnO:MnO_2 composites; Microstructure analysis; Dielectric properties
Received: 30 March 2023; **Revised:** 09 June 2023; **Accepted:** 16 June 2023

Introduction

Zinc oxide (ZnO) has taken great interest as a result of excellent employment in many fields such as electronics, optics and photonics [1,2]. So, in order to acquire higher speeds of electronic transportation and investigate the confinement effect on the optical properties, many researchers have focused their attention and works on the micro- and nanostructure zinc oxide. It is well known that ZnO has energy band gap of 3.3 eV and shows negative conductance. This enables to use it in the manufacture of transparent electronic and optoelectronic devices as well as sensors [3]. The importance of mixing ZnO – instead of indium tin oxide (ITO) – with another oxide can facilitate the engineering of the magnetic, electrical and optical properties of the devices based on such structures [4-8]. As well, mixing ZnO with transition metals was found to produce multifunctional composites those possess the same magnetic and optical properties [9]. It was referred that the samples can be fabricated in different forms like bulk or thin films with huge range of magnetic properties [10-11] and used in magneto-optical devices in the short wavelength region [12]. The incorporation of transition metal elements into ZnO structure provides easy way to produce tunable band gap that can be used in UV detectors and light emitting diodes (LEDs). Many researchers pointed out that mixing manganese (Mn) with ZnO will reduce energy band gap. It has been showed previously [13,14] and the monotonic increment of the energy band gap become in the shape of band bowing [15-21].

In this work, some features of $(ZnO)_{1-x}(MnO_2)_x$ thin films produced by PLD are reported, and the influence of Mn content on microstructural parameters, energy band gap and dielectric properties of $(ZnO)_{1-x}(MnO_2)_x$ thin films is explained.

Experimental Part

Six composite samples were made from mixing the appropriate amount of zinc oxide (ZnO) and manganese oxide (MnO) and the mixtures were put in quartz ampules. The ampules were evacuated, sealed and heated in an oven at temperatures of 1273 K for five hours. The obtained materials were grinded and pressed in form of pellets with thickness and diameters of 0.5 cm and 1 cm, respectively. These pellets were used as targets to prepare thin films using pulsed-laser deposition (PLD) method. The deposition of thin films were conducted by focusing Nd:YAG laser pulses on the target inside a chamber evacuated down to 10^{-3} torr. A Huafei Tongda Technology–Diamond-288 pattern EPLS laser system was used. This laser operates in Q-switching mode, wavelength 1064/532nm, repetition frequency of 1-6. The structural analysis was carried out using x-ray diffraction (XRD) patterns. The optical parameters were determined from the optical measurements using UV-visible spectrophotometry. The absorption coefficient was measured from the relation:

$$\alpha = -\frac{1}{d}(LnT) \qquad (1)$$

The energy band gap was obtained from Tauc's relation for direct allowed transition:

$$(\alpha h\nu)^2 = B(h\nu - E_g) \quad (2)$$

The optical constants; mainly refractive index (n), extinction coefficient (k), real and imaginary parts of dielectric constant (ε_r) and (ε_i) were measured according to the following relations:

$$n = \sqrt{\frac{4R}{(R-1)^2-k^2}} - \frac{(R+1)}{(R-1)} \quad (3)$$

$$R = \frac{(n-1)^2+k^2}{(n+1)^2+k^2} \quad (4)$$

$$k = \frac{\alpha\lambda}{4\pi} \quad (5)$$

$$\varepsilon_r = n^2 - k^2 \quad (6)$$

$$\varepsilon_i = 2nk \quad (7)$$

where R is the reflectance

The electrical conductivity has been conducted by using LCR meter in the frequency range of 50 Hz to 50 MHz. The a.c. conductivity was estimated from

$$\sigma_{a.c.} = \frac{d}{\bar{R}.A} \quad (8)$$

where $\bar{R}$ is the resistance, d is the sample thickness and A is the effective area

Results and discussion

Figure (1) shows the x-ray diffraction patterns $(ZnO)_{1-x}(MnO_2)_x$ powders . The composites samples were prepared with different (x) values. XRD pattern shows many peaks located at two theta 31.9°, 34.55°, 36.33°, 47.63°, 56.71°, 68.76°, and 69.42° corresponding to the reflection planes (100), (002), (101), (102), (110), (112), and (201), respectively, with strong peaks at (101) for all of manganese oxide values reflection. It can be observed that by the increasing in Mn content from x=0.3 and go on reduced the intensity of the all the peaks. The crystal size were (32.9, 32.9, 32.9, 28.8,3 8.4, and 34.6 nm), referred that the addition of manganese oxide reduced the crystal size up x= 0.3 and the opposite of that take place. There are secondary phases appeared at x=0.1 and beyond. The peaks located at two theta equal 23.29°, 32.99°, 33.06°, 38.33°, 55.26°, and 65.83° corresponding to planes (211), (200), (200), (411), (440), and (622), respectively, belonging to Mn_2O_3 phase, while the peaks appeared at 2θ equals to 12.76°, 18.00°, 13.00°, 28.74°, 37.60°, and 44.52° corresponding to planes (110), (200), (310), (211), and (411), respectively, belonging to MnO_2 phase. Similarly, figure (2) shows the XRD patterns of $(ZnO)_{1-x}(MnO_2)_x$ thin films. There is secondary phase MnO appeared at 2θ equals to 35.13° and 40.43° belonging to the reflection planes (111) and (200), respectively. The peak intensities also decrease at x=0.3 to 0.5. This refers that too much Mn doping decadents the crystallinity of the films, which reflects the creation of additional stress and lattice disorder by the effect of larger radius of manganese ion (Mn^{2+}) (0.66Å) in compared to the radius of zinc ion (Zn^{+2}) (0.6Å) [22].

The values of lattice constants (a and c) of the $(ZnO)_{1-x}(MnO_2)_x$ structure were obtained from the following equation:

$$\frac{1}{d_{khl}} = \frac{4}{3}\left[\frac{h^2+hk+k^2}{a^2}\right] + \frac{l^2}{c^2} \quad (9)$$

where h, k and l are the Miller indices, d_{hkl} is the interplanar spacing for the plane (hkl)

The crystal size (D), the dislocation density δ and the strain (ε) were calculated from the following equations:

$$D = \frac{0.9\lambda}{B\cos\theta} \quad (10)$$

$$\delta = \frac{1}{D^2} \quad (11)$$

$$\varepsilon = \frac{B\cos\theta}{4} \quad (12)$$

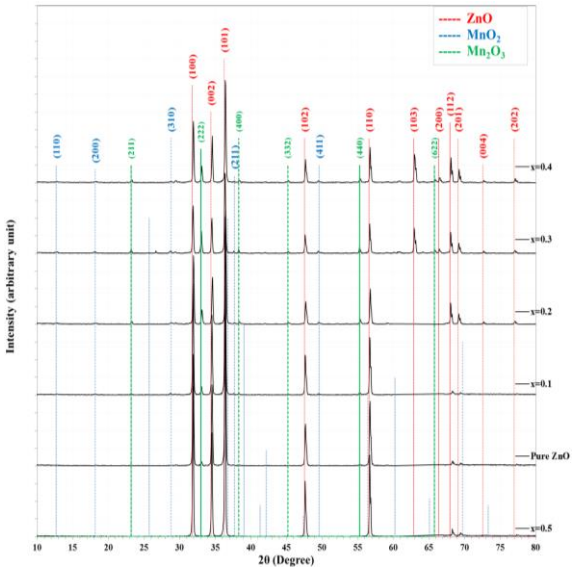

Fig. (1) The XRD patterns of $(ZnO)_{1-x}(MnO_x)_x$ powders

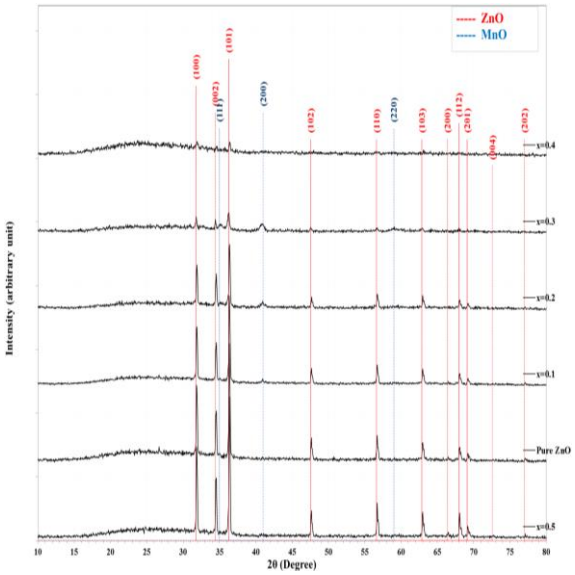

Fig. (2) The XRD patterns $(ZnO)_{1-x}(MnO_x)_x$ thin films

Table (1) displays the measured data of x-ray diffraction. It was found that average crystalline size increases to 47.6nm in the first stage of manganese oxide addition beyond x=0.3 and then decreases to lower value (24.4nm). On the other hand, the main diffraction peaks shift toward higher 2θ with the

 ISSN (print) 1813-2065, (online) 2309-1673

increase of x content, while the lattice constants values (*a* and *c*) were reduced by the continues addition of manganese oxide. The reduction of *a* and *c* values takes place as a result of zinc vacancies. It is well-known that manganese can exist in three different ionic forms named Mn^{2+}, Mn^{3+}, and Mn^{4+}. The ionic radius of the manganese ions Mn^{2+}, Mn^{3+}, and Mn^{4+} are 0.66Å, 0.58Å and 0.53Å, respectively. The increase of x content increases the values of *a* and *c* due to Zn^{2+} (0.60Å) is substituted by Mn^{3+} and Mn^{4+} [23]. This results was proved by previous work [24].

The growing of lattice constants take place for high value Mn content is occurred as a results of creation of deformations and strain in the films by the influence of admission of Mn as well as lattice mismatch between the film and the substrate as shown in table (1). This results agreed with the finding of references [25-28].

Table (1) The measured data from the XRD patterns, the lattice constants, crystal size, dislocation density, and stress of $(ZnO)_{1-x}(MnO_2)_x$ thin films

x	a	c	Crystal Size (nm)	Dislocation Density (line/m²)	Strain (ε)
0	3.2407	5.1918	26.00	$1.48x10^{15}$	0.0070
0.1	3.2407	5.1918	47.70	$0.44x10^{15}$	0.0070
0.2	3.2407	5.1875	47.60	$0.44x10^{15}$	0.0070
0.3	3.2378	5.1875	47.60	$0.44x10^{15}$	0.0013
0.4	3.2436	5.2046	26.00	$1.48x10^{15}$	0.0013
0.5	3.2432	5.2046	24.40	$1.48x10^{15}$	0.0070

The optical band gap (E_g) can be measured by fitting the absorption data to the direct transition equation by extrapolating the linear portions of the curves to zero as shown in Fig. (3). It can be observed a red shift in the energy gap as a result of Mn addition to ZnO. The energy gap of pure ZnO was 3.4 eV and it begin change as Mn was added to the host material. The energy gap values for different MnO content were 3.5, 2.7, 2.65, 1.6 and 2.65 eV, respectively. The reduction of the energy gap occurred by increasing of x content is ascribed to the interaction of different orbitales *s-d* and *p-d* which consequently leads to bowing of band gap in accordance to the explanation of second-order perturbation theory [29]. The energy gap return to increase for high Mn content.

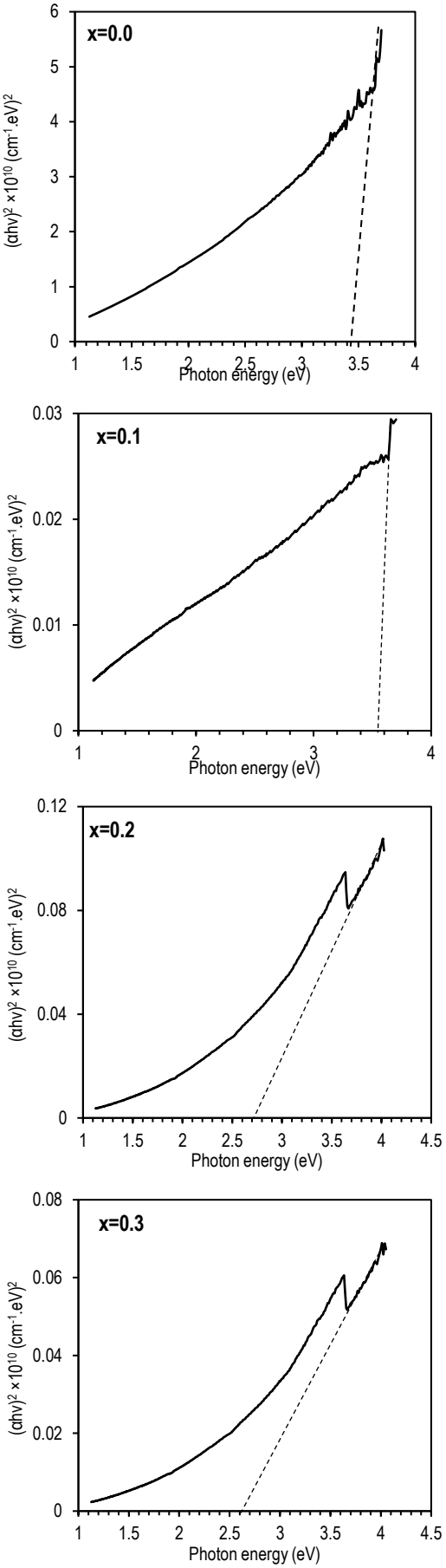

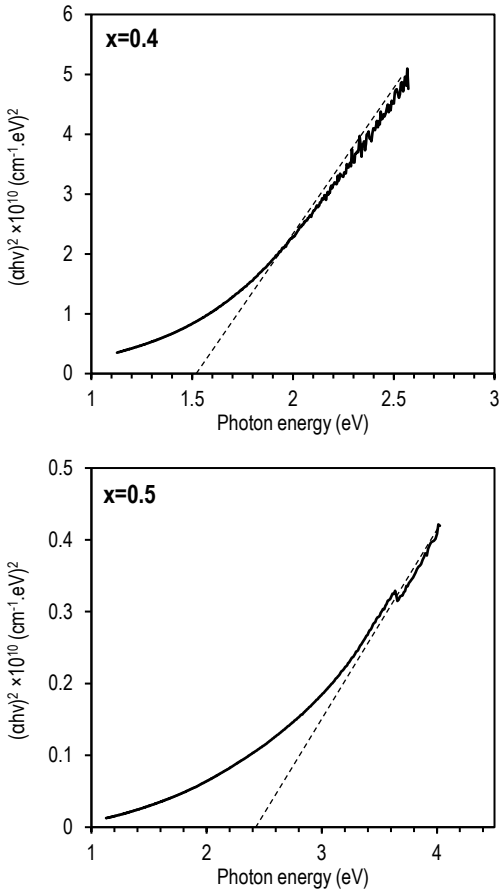

Fig. (3) The relation between $(\alpha h\nu)^2$ and photon energy (hv) for $(ZnO)_{1-x}(MnO_2)_x$ thin films with different values of x

The refractive index, extinction coefficient, real and imaginary dielectric constant were plotted as functions of wavelength as shown in figures (4-7). It is obvious that refractive index gets to change with increasing mixing ratio. The refractive index suffers reduction as manganese oxide added to the starting material otherwise the refractive index grow up by increasing of manganese ratio. The reduction and growing of refractive index is related with increasing of transparency and opacity of the composites thin films respectively [30-31]. The behavior of extinction coefficient is shown in Fig. (5) and table (2). It is clearly observed that (k) reduced in the first as MnO_2 added to the starting material and then get to grow up. The variation of (k) is ascribed to the variation of absorption coefficient. The plot diagram of real and imaginary dielectric constant shown in figures (6) and (7). The variation of real dielectric constant with mixing ratio is related with the variation of (n) according to Eq. (7) while the changing of imaginary dielectric constant is related with (k) according to Eq. (8).

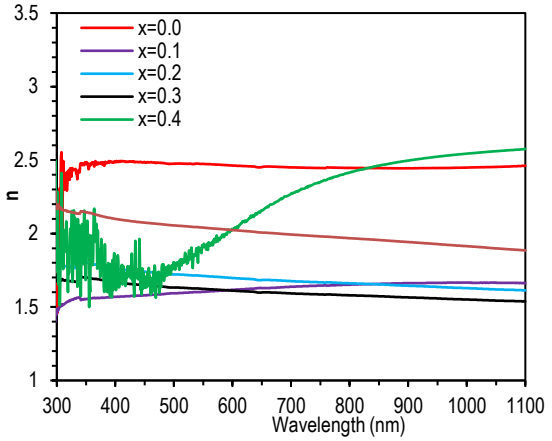

Fig. (4) The refractive index of $(ZnO)_{1-x}(MnO_2)_x$ thin films as a function of wavelength

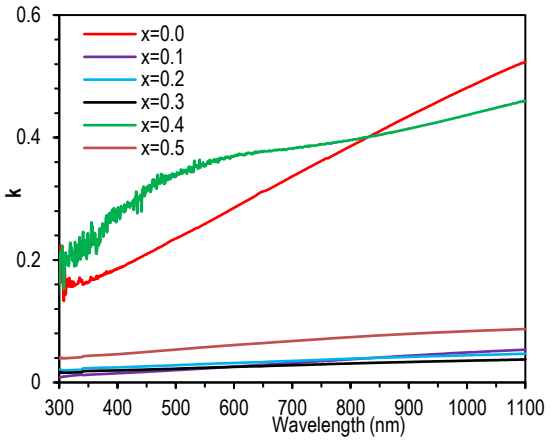

Fig. (5) The extinction coefficient of $(ZnO)_{1-x}(MnO_2)_x$ thin films as function of wavelength

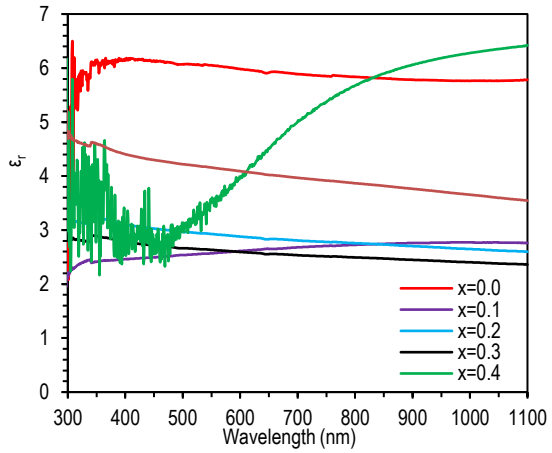

Fig. (6) The real dielectric constant of $(ZnO)_{1-x}(MnO_2)_x$ thin films as function wavelength

 ISSN (print) 1813-2065, (online) 2309-1673

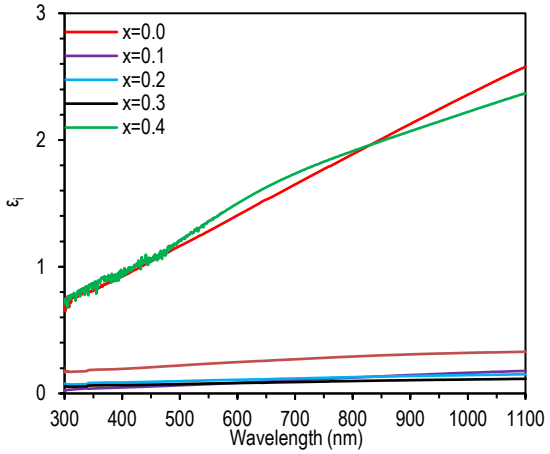

Fig. (7) The imaginary dielectric constant of $(ZnO)_{1-x}(MnO_2)_x$ thin films as function wavelength

Table (2) The optical parameters measured at λ=550nm and the energy band gap of $(ZnO)_{1-x}(MnO_2)_x$ thin films

Sample	T (%)	α (cm^{-1})	k	n	ε_r	ε_i	E_g (eV)
0.0	30.67	59101	0.259	2.474	6.054	1.281	3.40
0.1	90.11	5211	0.023	1.603	2.570	0.073	3.50
0.2	87.15	6880	0.030	1.711	2.927	0.103	2.70
0.3	89.58	5504	0.024	1.623	2.634	0.078	2.65
0.4	19.68	81296	0.356	1.906	3.506	1.357	1.60
0.5	76.87	13156	0.058	2.040	4.159	0.235	2.50

The plot of the dielectric constant versus the dielectric loss (ε_r vs. ε_i) of $(ZnO)_{1-x}(MnO_2)_x$ composites at different composites ratios are demonstrated in Fig. (8). In the investigated frequency range, the relation creates one semi- circle where the center occur below of the dielectric constant axis, this arc is a feature of presence of relaxation time distribution in the entire system [32]. It is clearly observed that the diameter of the circle get to vary with the x content, indeed it can be noticed that the diameter of the circle get change irregularly with the increase of x content this refers to pronounced change in the resistivity which reflect the modification the electrical properties of ZnO. The equivalent circuit can be given by parallel connection of resistance with a constant phase element which identical with the Cole–Cole model proposed by [33]. The measured polarizability were listed in table (3). The polarizability get to grow with x content reach maximum value at x=0.4 and the fall again. The behavior explanation of polarizability can be is found published elsewhere [34-38].

Figure (9) shows the frequency dependence of $\ln(\sigma_{a.c})$ for $(ZnO)_{1-x}(MnO_2)_x$ composites at various composites content. It is clear that the conductivity is basically increase as frequency increase. The demonstration of conductivity change with frequency (ω) and temperature is given by power law of Jonscher universal power law [39]:

$$\sigma_{tot}(\omega) = \sigma_{d.c.} + \omega \bar{A}^s \quad (13)$$

where $\bar{A}$ a constant a criteria of measuring the polarizability strength $\sigma_{d.c.}$ is the dc conductivity due to band conduction and (s) the important physical meaning is an exponent where the value ≤ 1 [40].

The slope of the same plot at high frequencies represent (s). The measured values of the exponent (s) are pot in table (2). There are many theories were postulated to described the behavior of (s). The quantum mechanical tunneling QMT model which proposed that (s) is temperature independent [41]. While when overlapping take place is the most convenient model postulated by Wang et al. [42] is large polaron tunneling model here (s) reduced by increasing of temperature till certain value after (s) suffering growing with raising temperature. In the case of small polaron model, (s) must grows by increasing of MnO_2 content [43]. The values of (s) in this work get to change non systematically with the increase of x content (decreases and increases with x). The proposed models are correlated barrier hopping (CBH) and small polaron (SP).The reduction of (s) proved the hopping of charge carriers over potential barrier will take place. The formula for (s) established of this model is given by Elliott [44,45]:

$$s=1-6k_BT/E_g \quad (14)$$

where E_g is the energy gap

This expression proposed that there is inverse relation between (s) and band gap of the investigated samples. The data display in table 1 and 3 proved this relation. The investigation of dielectric properties is additional reference to obtain valuable information in such a way that can be expected the type of conduction take place in the entire material as well as the sources of dielectric losses. Figure (10) shows the frequency dependence of dielectric constant for $(ZnO)_{1-x}(MnO_2)_x$ composites. It is clearly observed that dielectric constant get to reduce by the increase in frequency of the applied field. The dielectric constant at low frequency come from the contribution of different kinds of which are: deformational polarization (electronic, ionic) as well as relaxation (orientational and interfacial). At higher frequency the dipoles stope to follow the electric field variation which consequently reduced the orientational polarization and the dielectric constant reach constant value which related to interfacial polarization. On the other hand, at a constant frequency, the dielectric constant get to grow by increase of x content. This may be attributed to the inability of the dipoles to orient themselves at low x content by increasing x content, the orientation of the dipoles is become more easily (following thermal movements), which tends to an increase in dielectric constant value. The tangent loss is given by:

$$tan\delta = \frac{\varepsilon_i}{\varepsilon_r} \quad (15)$$

The changing of tangent loss with the frequency for $(ZnO)_{1-x}(MnO_2)_x$ composites with different x content is shown in Fig. (11). It is found at definite frequency, the dielectric loss increases by increase as MnO_2 was added to the starting oxide but then fall for further increase of MnO_2. This behavior may be attributed that to the minimum conduction loss for

low MnO_2 content. The continuous addition of MnO_2 is found be accompanied by creation of additional loss in the conductivity [46]. On the other hand the tangent loss for x content in the range (0-0.3) increases with increase in frequency reaching a maximum peak and then decreases, while the behavior for residual x values is opposite to that.

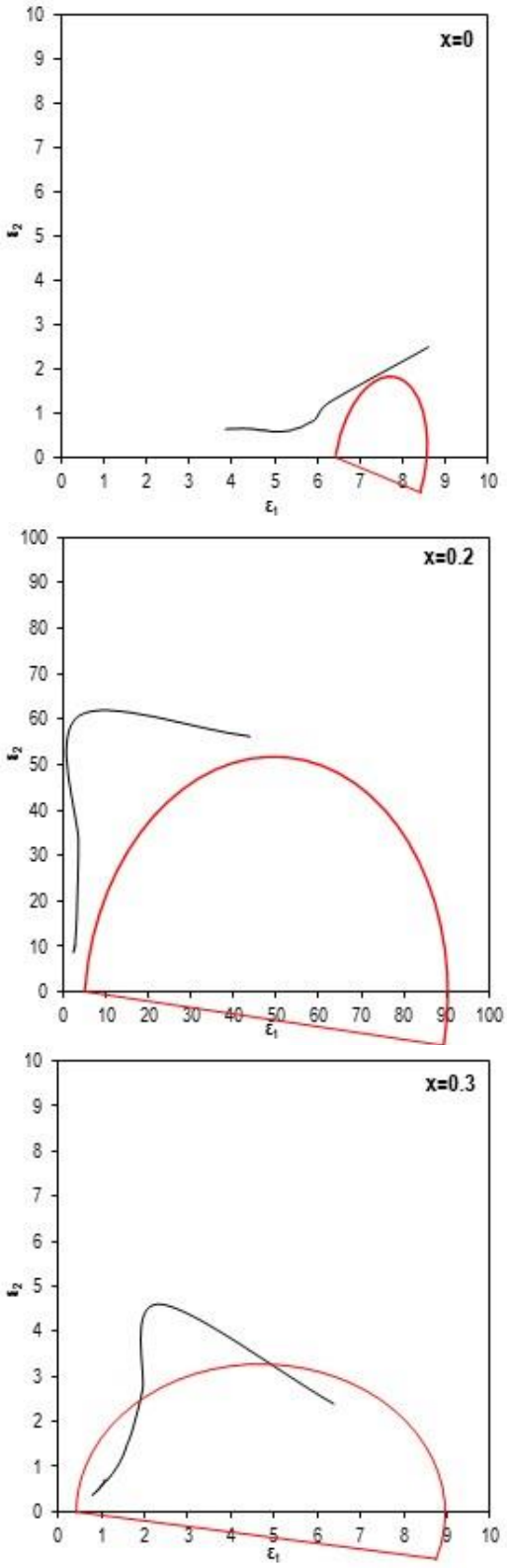

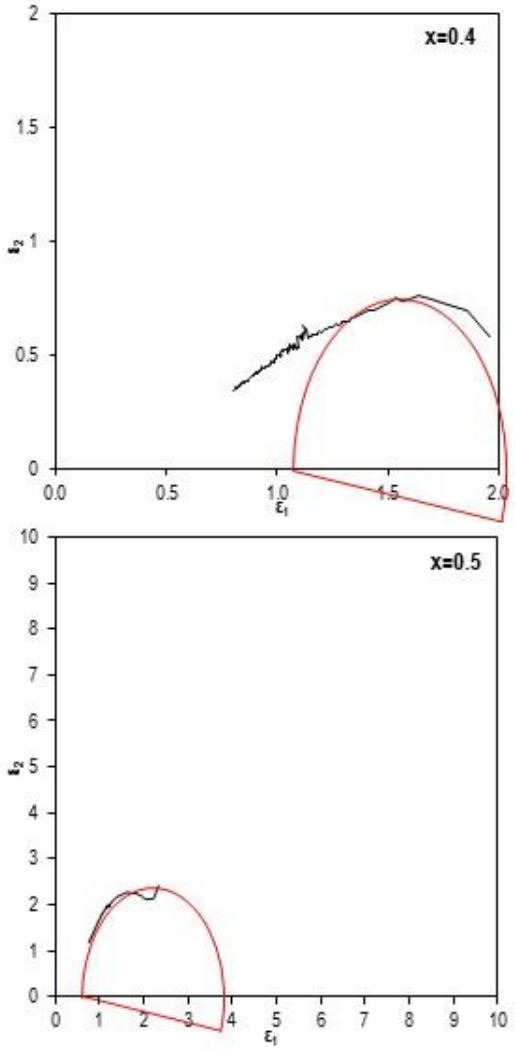

Fig. (8) The plot of dielectric constant versus dielectric loss of $(ZnO)_{1-x}(MnO_2)_x$ composites

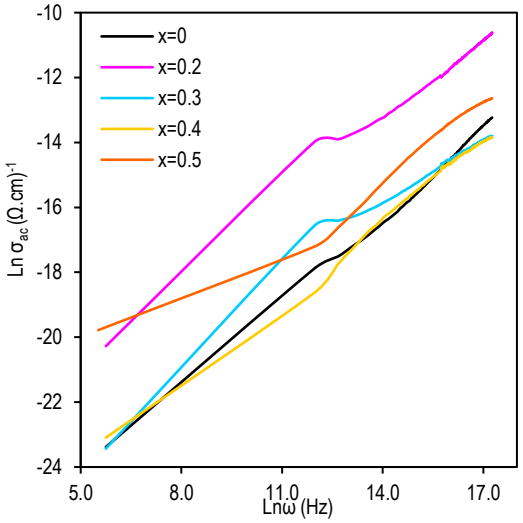

Fig. (9) The frequency dependence of electric conductivity of $(ZnO)_{1-x}(MnO_2)_x$ composites

 ISSN (print) 1813-2065, (online) 2309-1673

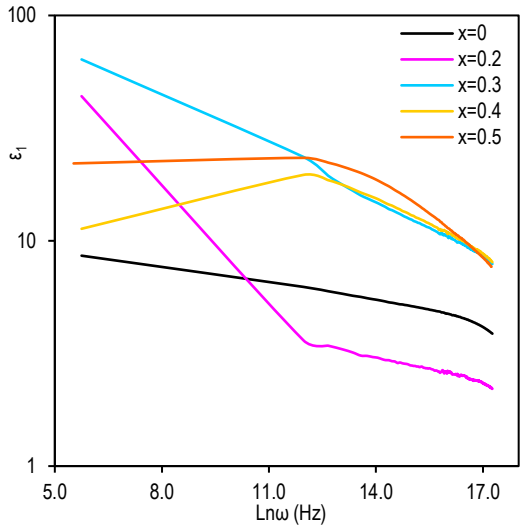

Fig. (10) The frequency dependence of dielectric constant of $(ZnO)_{1-x}(MnO_2)_x$ composites

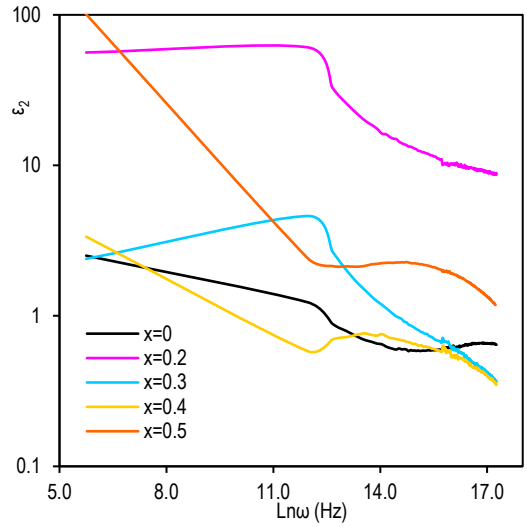

Fig. (11) The frequency dependence of dielectric loss of $(ZnO)_{1-x}(MnO_2)_x$ composites

Table (3) Values of polarizability, (s) power factor and density of states at Fermi level

x	α	s	$N(E_f)$
0	0.144444	0.948	6.77165E+34
0.2	0.044444	0.798	1.01874E+36
0.3	0.200000	0.711	1.3306E+36
0.4	0.222222	0.806	2.74113E+36
0.5	0.111111	0.731	1.34422E+36

Conclusion

Solid state reactions were adopted to prepare different composites from ZnO and MnO_2. The characterization of structures proved that manganese atoms substitute zinc sites in the crystals without modifying the hexagonal zinc oxide structure, with little variation in the lattice parameters with the extent of mixing. The optical measurements declare reduction of the energy gap upon MnO addition for Mn content $x \leq 0.4$. The optical constant together reduced as Mn introduced to ZnO after that they get to grow up. The study of ac conductivity for various MnO_2 content was found to follow the Jonscher's power law where s in the range 0.711-0.948. The polarizability values estimated that $(ZnO)_{1-x}(MnO_2)_x$ composites can be used in electronic circuits as resistor.

References

[1] S. Das Sarma, "Spintronics", *Am. Sci.*, 89(6) (2001) 516-528.
[2] P. Sharma, K. Sreenivas and K.V. Rao, "Analysis of ultraviolet photoconductivity in ZnO films prepared by unbalanced magnetron sputtering", *J. Appl. Phys.*, 93 (2003) 3963-3970.
[3] S.N. Khanna et al., "Ferrimagnetism in Mn_7 Cluster", *Chem. Phys. Letts.*, 378 (2003) 374-379.
[4] S. Major, A. Banerjee and K.L. Chopra, "Highly transparent and conducting indium-doped zinc oxide films by spray pyrolysis", *Thin Solid Films*, 108 (1983) 333-340.
[5] S. Major et al., "Thickness-dependent properties of indium-doped ZnO films", *Thin Solid Films*, 143 (1986) 19-30.
[6] K. Hauffe and A.L. Vierk, "Electrical conductivity of zinc oxide with foreign oxides", *J. Phys. Chem.*, 196 (1950) 160.
[7] C. Wagner, "The mechanism of the decomposition of nitrous oxide on zinc oxide catalyst", *J. Chem. Phys.*, 18 (1950) 69-71.
[8] A.F. Aktaruzzaman, G.L. Sharma and L.K. Malhotra, "Electrical, optical and annealing characteristics of ZnO:Al films prepared by spray pyrolysis", *Thin Solid Films*, 198 (1991) 67-74.
[9] S.K. Mandal and T.K. Nath, "Microstructural, magnetic and optical properties of ZnO:Mn ($0.01 \leq x \leq 0.25$) epitaxial diluted magnetic semiconducting films", *Thin Solid Films*, 515 (2006) 2535-2541.
[10] P. Sharma et al., "Ferromagnetism above room temperature in bulk and transparent thin films of Mn-doped ZnO", *Nat. Mater.*, 2 (2003) 673-677.
[11] D.C. Kundaliya et al., "On the origin of high-temperature ferromagnetism in the low-temperature processed Mn– Zn–O system", *Nat. Mater.*, 3 (2004) 709-714.
[12] C.J. Cong et al., "Synthesis, structure and ferromagnetic properties of Mn-doped ZnO nanoparticles", *Nanotechnol.*, 16 (2005) 981-984.
[13] S. Venkataprasad Bhat and F.L. Deepak, "Tuning the bandgap of ZnO by substitution with Mn^{2+}, Co^{2+} and Ni^{2+}", *Solid State Commun.*, 135 (2005) 345-347.
[14] R. Viswanatha et al., "Synthesis and Characterization of Mn-Doped ZnO Nanocrystals", *J. Phys. Chem. B*, 108 (2004) 6303-6310.
[15] J.K. Furdyna, "Diluted magnetic semiconductor", *J. Appl. Phys.*, 64 (1988) R29-R64.
[16] R.B. Bylsma et al., "Dependence of energy gap on x and T in $Zn_{1-x}Mn_xSe$: The role of exchange interaction", *Phys. Rev. B*, 33 (1986) 8207-8215.

[17] A.E. Jimenez-Gonzalez, A.J. SotoUrueta and R. Suarez-Para, "Optical and electrical characteristics of aluminum-doped ZnO thin films prepared by sol-gel technique", *J. Cryst. Growth,* 192 (1998) 430-438.
[18] J. Alaria et al., "No ferromagnetism in Mn doped ZnO semiconductors", *Chem. Phys. Lett.*, 415 (2005) 337-341.
[19] H.-W. Zhang et al., "Optical and magnetic resonance investigations of $Zn_{1-x}Mn_xO$ magnetic semiconductors", *J. Magn. Magn. Mater.*, 305 (2006) 377-380.
[20] H.-W. Zhang et al., "Magnetism in $Zn_{1-x}Mn_xO$ crystal prepared by hydrothermal method", *Solid State Commun.*, 137 (2006) 272-274.
[21] V.R. Shinde et al., "Mn doped and undoped ZnO films: A comparative structural, optical and electrical properties study", *Mater. Chem. Phys.*, 96 (2006) 326-330.
[22] P. Singh, A. Kaushal and D. Kaur, "Mn-doped ZnO nanocrystalline thin films prepared by ultrasonic spray pyrolysis", *J. Alloys Comp.*, 471(1-2) (2009) 11-15.
[23] K.P. Bhatti et al., "On the room-temperature ferromagnetism in $Zn_{0.98}(MnO_2)_{0.02}$", *Solid State Commun.*, 136 (2005) 384-388.
[24] B.N. Dole et al., "Structural studies of Mn doped ZnO nanoparticles", *Curr. Appl. Phys.*, 11(3) (2011) 762-766.
[25] C. Kittel, **"Introduction to Solid State Physics"**, 5th ed., Wiley (NY, 1976).
[26] K. Ueda, H. Tabata and T. Kawai, "Magnetic and Electric Properties of Transition-Metal-Doped ZnO Films", *Appl. Phys. Lett.*, 79 (2001) 988-999.
[27] A. Tiwari et al., "Structural, optical and magnetic properties of diluted magnetic semiconducting $Zn_{1-x}Mn_xO$ films", *Solid State Commun.*, 121 (2002) 371-374.
[29] R.B. Bylsma et al., "Dependence of energy gap on x and T in $Zn_{1-x}Mn_xSe$: The role of exchange interaction", *Phys. Rev. B*, 33 (1986) 8207-8215.
[30] B.A. Hasan et al., "Structural, Morphology and Optical Properties of Al_xSb_{1-x} Thin Films Prepared by Pulsed Laser Deposition (PLD)", *AIP Conf. Proc.*, 2372 (2021) 040010.
[31] B.A. Hasan and M.A. Kadhim, "Structure, Morphology and Optical Properties of Thermally Evaporated Cu_2S Thin Films Annealed at Different Temperatures", *AIP Conf. Proc.*, 2144 (2019) 030021.
[32] M. Haj Lakhdar, B. Ouni and M. Amlouk, "Dielectric relaxation, modulus behavior and conduction mechanism in Sb_2S_3 thin films", *Mater. Sci. Semicond. Process.*, 19 (2014) 32-39.
[33] R. Cheruku, L. Vijayan and G. Govindaraj, "Electrical relaxation studies of solution combustion synthesized nanocrystalline Li_2NiZrO_4 material", *Mater. Sci. Eng. B*, 177(11) (2012) 771-779.
[34] B.A Hasan and D.A. Umran, "Dielectric permittivity and ac conductivity of CuInSeTe thin films", *Semicond. Sci. Technol.*, 27 (2012) 125014.
[35] B.A. Hasan and H.H. Issa, "Dielectric properties and A.C electrical conductivity analysis of $(La_2O_3)_{1-x}(ZnO)_x$", *IOP Conf. Ser.: Mater. Sci. Eng.*, 928 (2020) 072003.
[36] B.A. Hasan et al., "Characterization of CuInSTe/CdS Heterojunctions", *IOP J. Phys.: Conf. Ser.*, 1032 (2018) 012020.
[37] B.A. Hasan and H.H. Issa, "Effect of thickness on the structure, morphology and A.C Bi_2S_3 thin films", *Iraqi J. Phys.*, 15(33) (2017) 87-95.
[38] B.A. Hasan and I.H. Shalal, "Dielectric behavior and AC electrical conductivity analysis of PMMA films", *Iraqi J. Phys.*, 11(20) (2013) 47-57.
[39] A.K. Jonscher, "The 'universal' dielectric response", *Nature*, 267 (1977) 673-679.
[40] K. Funke, "Jump relaxation in solid electrolytes", *Prog. Solid State Chem.*, 22(2) (1993) 111-195.
[41] W.H. Jung, "AC conduction mechanisms of $Gd_{1/3}Sr_{2/3}FeO_3$ ceramic", *Physica B*, 403(4) (2008) 636-638.
[42] K. Wang, H. Chen and W.Z. Shen, "AC electrical properties of nanocrystalline silicon thin films", *Physica B*, 336 (2003) 369-378.
[43] H.M. Abdelmoneim, "Dielectric and AC Conductivity of Potassium Perchlorate, $KCLO_4$", *Acta Phisica Polonica*, A117 (2010) 936-940.
[44] S.R. Elliott, "A theory of a.c. conduction in chalcogenide glasses", *Phil. Mag. B*, 36(6) (1978) 1291-1304.
[45] S.R. Elliott, "Temperature dependence of a.c. conductivity of chalcogenide glasses", *Phil. Mag. B*, 37(5) (1978) 553-560.
[46] A.M. Farid and A.E. Bekheet, "AC conductivity and dielectric properties of Sb_2S_3 films", *Vacuum*, 59(4) (2000) 932-939.

 ISSN (print) 1813-2065, (online) 2309-1673

IRAQI JOURNAL OF APPLIED PHYSICS
Vol. 19, No. 4A, October 2023, pp. 29-36

Amenah A. Salman
Firas J. Kadhim

Department of Physics, College of Science, University of Baghdad, Baghdad, IRAQ

Spectral Analysis and Enhancement of Sm^{3+} Photoluminescence in Sol-gel Derived Sm^{3+}-Ag^{+} Co-doped Silica Xerogels

Sol-gel technology has been used to prepare silver (Ag^{+}) nanoparticles-samarium (Sm^{3+}) ions co-doped silica xerogel. Typical surface plasmon resonance (SPR) band is observed in the spectra of Ag NPs in both collision solutions and silica xerogels at 431 nm and 427 nm respectively. FE-SEM and XRD examination highlight the nanoscale and polycrystalline structure of Ag NPs, while FTIR study shows how the ions (Ag^{+},Sm^{3+}) are distributed within the porous structure of silica xerogels. The photoluminescence (PL) and absorption (A) spectra have been obtained as a function of Sm^{3+} concentrations at room temperature. Prominent emission bands of Sm^{3+} ions have been observed for the transitions $^4G_{5/2}\rightarrow{}^6H_{5/2}$, $^4G_{5/2}\rightarrow{}^6H_{7/2}$ and $^4G_{5/2}\rightarrow{}^6H_{9/2}$: 569, 601 and 645nm respectively, at 400nm excitation. The presence of Ag NPs improves the PL intensity of the Dy^{3+} ions, as illustrated by the PL of Sm^{3+} in doped and co-doped silica xerogels. This improvement has been obtained by leasing the strong local electric field induced by SPR of Ag NPs in order to transfer energy from the Ag NPs to the Sm^{3+} ions. Radiative lifetime (τ_{rad}) and emission cross section ($\sigma_{em.}$) for the $^4G_{5/2}\rightarrow{}^6H_{7/2}$ transition in doped and co-doped samples have been calculated. All co-doped samples have shown white light emission, with color coordinates in the white range.

Keywords: Surface plasmon resonance; Noble metals; Lanthanides ions; Photoluminescence
Received: 05 March 2023; **Revised:** 01 July 2023; **Accepted:** 08 July 2023

1. Introduction

Light-emitting diodes (LEDs) have attracted increased attention from engineers and scientists in the solid-state luminescence sector in recent years due to their environmental friendliness, extended lifetime, energy-saving specifications, and high luminous efficiency [1,2]. Due to their potential use in photonic applications, silica containing metallic nanoparticles (NPs) and lanthanide (Ln^{3+}) have attracted a lot of attention. In particular, silver nanoparticles (Ag NPs) have garnered an extensive of interest because of their remarkable optical properties due to a surface plasmon resonance (SPR) in the visible range [3-6]. In the presence of plasmonic nanoparticles, the luminescence intensity emitted by lanthanide ions can be enhanced due to a strong absorption cross-section related to surface plasmon excitation in noble-metal nanoparticles and/or a large local field enhancement that is generated around the excited nanoparticle. [7-9], Ln^{+3} occupies a special place in the field of photonics, Since it can produce white luminescence, Sm^{3+} ion has attracted significantly of interest among rare earth (RE) ions [10,11], the shielding around 4f shell of Ln^{+3} by the outer 5s and 5p shells caused the sharp fluorescence in the ultraviolet (UV), to infrared (IR) regions [12-14]. The element Sm^{3+} was chosen as it excited under UV wavelength, broad emission bands can be seen from Sm^{3+} ions in any host matrix because of their $^4G_{5/2}\rightarrow{}^6H_J$ (J=5/2, 7/2, 9/2) transitions. It is also well-known that the concentration and host composition affect the intensities of the emission bands of the Sm^{3+} ion in silica xerogel [15]. The study of the host of Sm^{3+} and concentration-dependent properties is essential if preferred emission characteristics are to be obtained for device applications.

Various wet chemical methods, such as co-precipitation, hydrothermal, sol-gel technology, and combustion method, have been developed for materials synthesis [15-18]. The sol-gel technology is widely used, and it is an effective process. The chosen host silica is designed to have high lanthanide ions solubility, moderate lower melting point, structure, and chemical stability, as well as outstanding transparency and lower phonon energy, in order to satisfy the required application with the appropriate optical qualities [19-21]. Sm^{+3}-doped silicates for intense emissions in the visible region, especially the yellow-orange-red emission region, due to a growing market for their application in traffic signs, decoration, and textile printing, near white- light emitting diode (LED) [10,11,22].

Silica xerogel was chosen as the host matrix. Upon doping of these xerogels with samarium and silver, this enabled us to analyze the sensitization of

a luminescence of the lanthanide activator by Ag ions and the influence Ag NPs on the intensity of optical transitions of the activator under investigation. White LEDs are one potential application for these monoliths.

2. Experimental Procedure

2.1 Chemicals

Tetraethyl orthosilicate (TEOS, purity >98% supplied by Schuchardt, Germany), ethanol (C_2H_5OH, 99.0% supplied by Fluka Garantie, Germany), water and hydrochloric acid (HCl) were used as the starting materials and catalyst, respectively. The molar ratio was taken as 1:5:10 for TEOS/ethanol/water. Samarium chloride hexahydrate solutions ($SmCl_3.6H_2O$, 99.9% from Aldrich, silver nitrate ($AgNO_3$), by sodium citrate ($Na_3C_6H_5O_7$) and sodium citrate ($Na_3C_6H_5O_7$) were supplied by Fluke (Germany).

2.2 Preparation of Monoliths

Silica xerogel monoliths doped with Sm^{3+} and co-doped with Sm^{3+}-Ag^{+} were prepared using the sol-gel technique. Pure ethanol was mixed with a TEOS and denoted as sol(I) containing TEOS. A catalyst solution of HCl and pure ethanol in deionized water is used to make sol(II), then for preparation doped and co-doped samples with the molar ratio 1:5:10 for TEOS/ethanol/water, Sm^{3+} doped silica xerogels were prepared by mixing the samarium chloride hexahydrate solutions prepared by dissolved ($SmCl_3.6H_2O$) in deionized water with different concentrations (0.04, 0.09, 0.225, 0.55, 1.5)x10^{-1} M with sol(II) and then added to sol(I) with magnetic stirring for 30 min. Then a 0.5ml of N-N dimethylformamide was added as drying control chemical additive (DCCA) to the final sol. By pouring the Sol into a covered glass tube in an oven set at 60 °C, monoliths were able to gel after 14 hours, and for Ag^{+}-Sm^{3+} co-doped, mixture of samarium chloride hexahydrate solutions and silver colloid (yellow-brown) with concentration of 5x10^{-3} M has been prepared by using the chemical reduction method [23-24], were added to sol(II). The sol(II) was slowly added to sol(I) with magnetic stirring for 30 min to ensure homogeneity, then 0.5ml of N-N dimethylformamide was added to the final sol. A sealed glass tube containing the final sol was placed in an oven heated to 60 °C. The aging process was achieved after reaching the gel point after 24 hours. The transparent samples achieved by drying the gel with diameter of 0.7-0.8 cm, length of 1.9-2.1 cm and weight of 1.1899-1.3932 g for Sm^{3+} doped silica xerogel, and with diameter of 0.73-0.85 cm, length of 2.0-2.2 cm and weight of 1.3079-1.4099 g for Sm^{3+}-Ag^{+} co-doped silica xerogels.

3. Results and Discussion

The surface plasmon resonance (SPR) band of Ag NPs was recorded using a Shimadzu UV-1800 Double-Beam UV-Visible spectrophotometer (Fig. 1a,b). Figure (1a) represents the plasmon band centered at 437 nm in the colloid solution (yellow-brown) with concentration of 5x10^{-3} M. Figure (1b) shows a slight blue shift in SPR centered at 427 nm due to the doping of Ag NPs to silica xerogel at a concentration of 35.7x10^{-5} %.

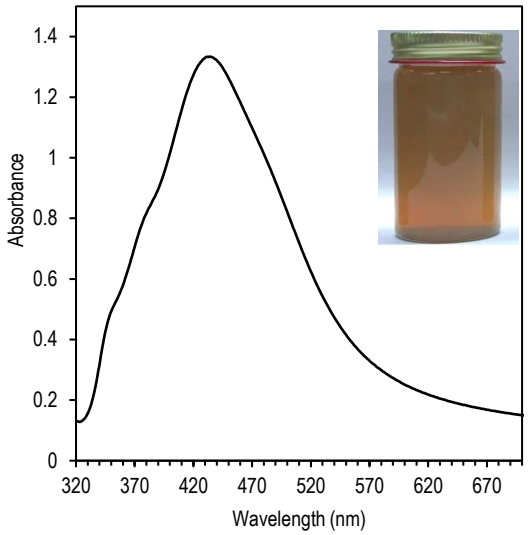

(a)

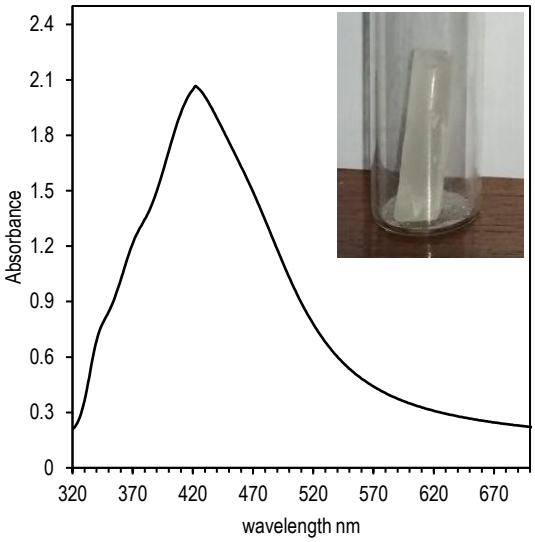

(b)

Fig. (1) UV-visible absorption spectrum of (a) Ag NPs in colloid solution, (b) Ag NPs doped silica monolith

The crystallinity of Ag NPs was detected using a Philips PW 1050 X-ray diffractometer, 1.54Å from Cu-K). Figure (2) shows an XRD pattern for polycrystalline Ag NPs, as shown by the single peak at 2θ=38°. This corresponds to the peak expected according to ASTM standards.

 ISSN (print) 1813-2065, (online) 2309-1673

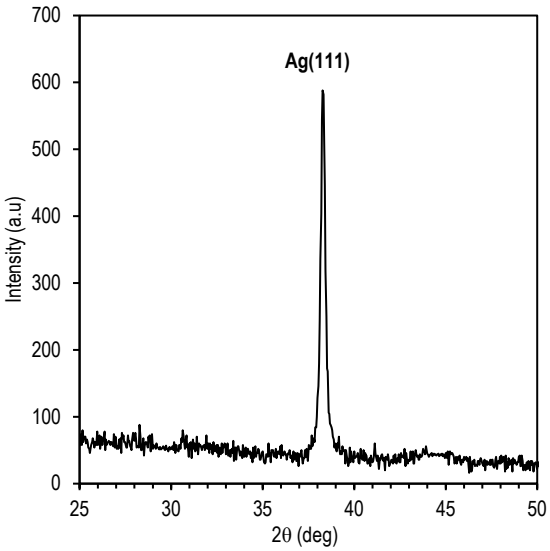

Fig. (2) XRD pattern of silver nanoparticles synthesized by chemical method

Field-emission scanning electron microscopy analysis was carried out using an Inspect F50 FE-SEM instrument to determine the morphology and size of the Ag NPs colloid. Figure (3) demonstrates that the nanoparticles of Ag NPs were nearly perfectly spherical, with sizes ranging from 31 to 35 nm and least agglomeration.

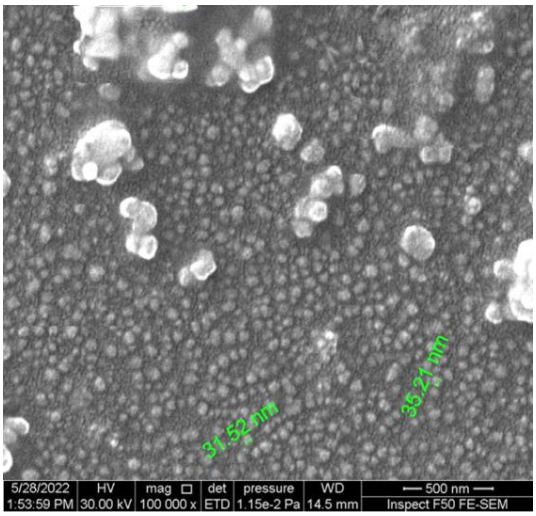

Fig. (3) FE-SEM image of Ag NPs synthesized from chemical reduction method

The intra-configurational $4f^n$-$4f^n$ transitions detected by spectra of Sm^{+3} ions in monoliths at various concentrations (4.3, 10.0, 21.9, 50.5, 178.0) $x10^{-4}$ %. According to the absorption spectra displayed in Fig. (4), the absorbance increases as the concentration of Sm^{+3} ions increases [25,26].

In Fig. (5), the photoluminescence (PL) spectra were recorded using a xenon lamp source in Shimadzu RF-5301 PC Spectrofluorophotometer of a Sm^{3+}-doped silica monolith at 400 nm excitation wavelength for the range of Sm^{3+} ion concentrations.

The $^4G_{5/2}\rightarrow{}^6H_{5/2}$ and $^4G_{5/2}\rightarrow{}^6H_{7/2}$ transitions are responsible for the 569 and 601 nm emission peaks, respectively, in the yellow-orange region of the spectrum, while the $^4G_{5/2}\rightarrow{}^6H_{9/2}$ transition causes the faint emission peak at 645 nm in the red region of spectra [25-27]. The absence of a symmetry center results in an occurrence of electric-dipole transitions ($^4G_{5/2}\rightarrow{}^6H_{9/2}$), the intensity of which is highly sensitive to variations in the local structural environment of the Sm^{3+} ions.

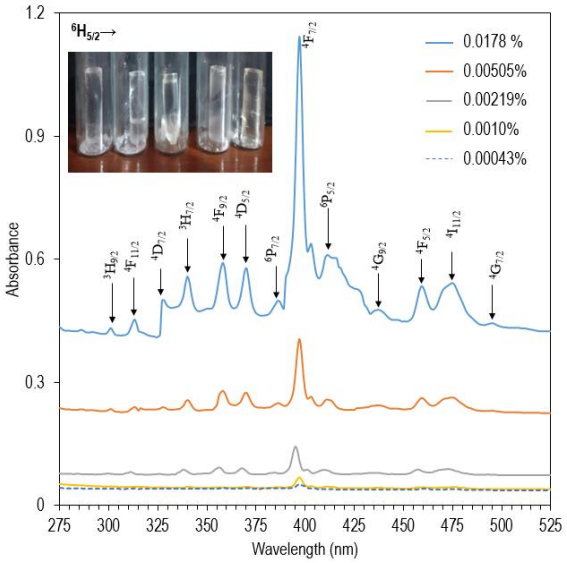

Fig. (4) The absorption spectra of silica monoliths doped with different concentrations of Sm^{+3} ions

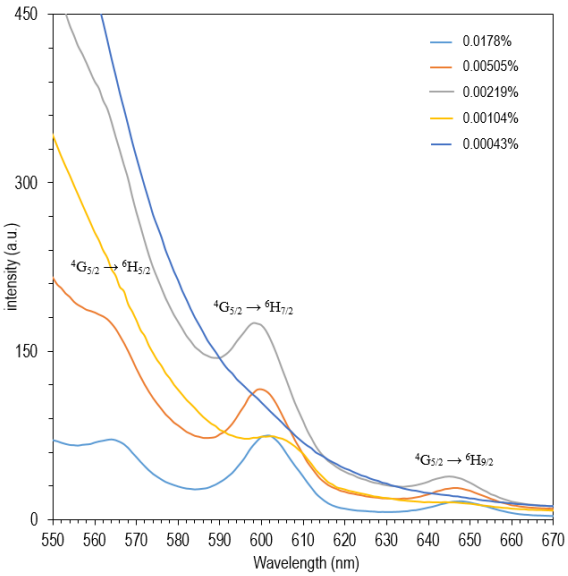

Fig. (5) The emission spectra of silica monolith doped with different concentrations of Sm^{+3} ions, excited by 400 nm

Despite the existence of the magnetic-dipole allowed transitions $^4G_{5/2}\rightarrow{}^6H_{5/2}$ and $^4G_{5/2}\rightarrow{}^6H_{7/2}$, the strengths of these transitions rarely vary with the local structural symmetry of the Sm^{3+} ions [25,26]. It is worth observing that the emission intensity is higher in the sample with a concentration of 0.00219% than in the other samples. Luminescence

quenching for Sm^{+3} in the silica matrix at other concentrations may be due to energy transfer between excited Sm^{+3} ions, as seen in cases such as cross-relaxation (CR) interactions between lanthanide ions, strong interactions between two active ions that can transfer excitation energy from one Sm^{+3} ion to another, O-H vibrations of water, and concentration quenching exhibited by Sm^{+3} ions at higher concentrations [25]. This phenomenon is most likely caused by an increase in the number of nonradiative decay channels and also due to many closely spaced excited states, which leads to the quenching; it denotes the clustering of these ions within the pores of the sol-gel material.

Figure (6) shows the absorption spectra of all Ag^{+}/Sm^{3+} co-doped silica xerogel samples with concentrations between 35.7×10^{-5}/0.00034 and 35.7×10^{-5}/0.0178%), containing Ag NPs. Each spectrum consists of fourteen absorption bands, thirteen corresponding to intra-configurational $4f^{n}$-$4f^{n}$ transitions of the Sm^{3+} ions and one corresponding to the Ag NPs. The presence of these bands in Ag^{+}-Sm^{3+} co-doped and Sm^{3+} doped materials is indicative of the spectroscopic activity of these ions.

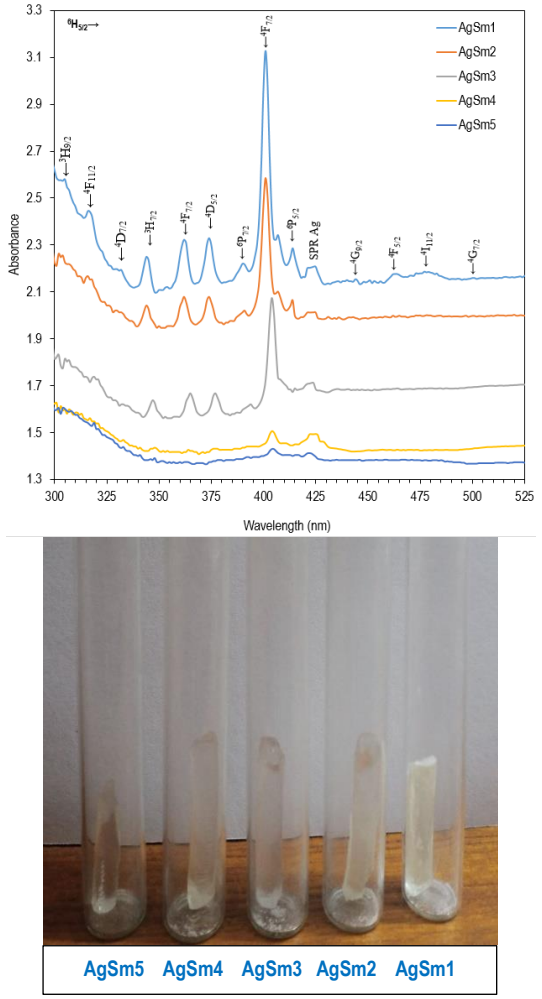

Fig. (6) (a) Absorption spectra of Ag-Sm^{3+} co-doped monoliths, (b) photographs of co-doped samples

Figure (7) illustrates the recorded PL spectra of the Ag^{+}-Sm^{3+} co-doped monoliths using the 400 nm excitation wavelength. It should be mentioned that the PL intensity of the monoliths is enhanced, local field effect (LFE), caused by surface plasmon resonance (SPR) of metallic NPs, can contribute to the enhancement, since the relative permittivity of the host silica oscillations of electrons, moving along the surface of metal NPs, oscillations induce a confined electromagnetic field in the vicinity of NPs [29,30], which result in an enhancement of the local electric field around the NPs, energy transfer from Ag NPs to Sm^{3+} ions has also been estimated as a cause for enhanced luminescence intensity ($Ag^{+}\rightarrow Sm^{3+}$) [28,29].

Fourier-transform infrared (FTIR) spectra of the all doping and co-doping samples were illustrated in Fig. (8). These spectra supported a distribution of ions (Ag^{+}, Sm^{3+}) in these porous structures. the absorption bands that correspond to the host's characteristic vibrational bands were discovered in the FTIR spectra; these bands were located at approximately 470, 800, and 1064 cm^{-1}, respectively, and were caused by the bending, symmetric stretching, and asymmetric stretching vibrations of siloxane Si-O-Si groups, while a weaker band at approximately 960 cm^{-1} was caused by the stretching vibration of silanol Si-OH groups, At roughly 1658 and 3419 cm^{-1}, two more bands were developed. The O-H bond in water molecules vibrates in these two bands [31,32], showing that the drying process at 60 °C does not entirely capture the water molecules from a silica pores.

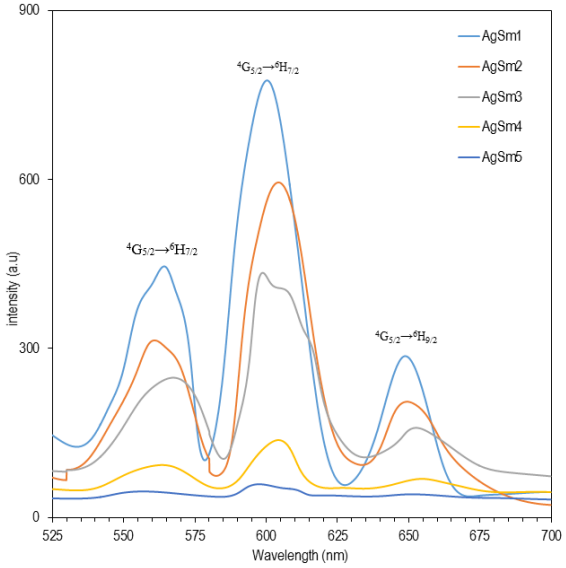

Fig. (7) Emission spectra of silica xerogel co-doped with Ag^{+}-Sm^{3+} ions excited by 400nm

 ISSN (print) 1813-2065, (online) 2309-1673

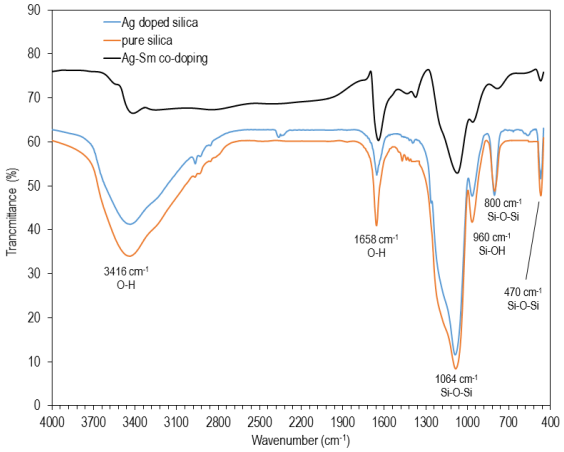

Fig. (8) FTIR spectra of pure silica xerogel, Ag doped and Ag^{+}-Sm^{3+} co-doped silica xerogel

The refractive index n(λ) was calculated by Michelson interferometer and was about 1.46-1.47. Bowen and Wokes gave an empirical formula to get a sufficiently accurate value of radiative lifetime (τ_{rad}) as follows [33]:

$$\frac{1}{\tau_{rad}} = 2.88 \times 10^{-9} \times n^2 * \grave{\upsilon} \int \varepsilon(\grave{\upsilon}) d\grave{\upsilon} \qquad (1)$$

where ὺ is the wavenumber at a peak of the absorption band in cm^{-1} and $\int \varepsilon(\grave{\upsilon}) d\grave{\upsilon}$ is the area under the absorption band curve, and ε(ὺ) is the molecular extinction coefficient.

Peak emission cross-section (σ_{em}) for transition $^4G_{5/2} \rightarrow {}^6H_{7/2}$ can be determined from:

$$\sigma_{em} = \frac{\lambda_p^4}{8\pi\, c\, n`^2\ \ \Delta\lambda_{eff}\ \tau_{rad}} \qquad (2)$$

where λ_p is a peak wavelength within the fluorescence band, $\Delta\lambda_{eff}$ is the emission linewidth (effective); which is determined by a full-width half maximum (FWHM) of the emission band, and ń is given by:

$$n` = \frac{(n^2(\lambda)+2)^2}{9n(\lambda)} \qquad (3)$$

The oscillator strength f_{exp} can be calculated from the absorption spectra using the formula [34]:

$$f_{exp} = 4.32 \times 10^{-9} \int \varepsilon(\grave{\upsilon}) d\grave{\upsilon} \qquad (4)$$

Table (1) (*see appendix*) includes the results of the calculated parameters from the recorder spectra. These parameters are related to the absorption band for transition $^6H_{5/2} \rightarrow {}^4F_{7/2}$ and the emission band for transition $^4G_{5/2} \rightarrow {}^6H_{7/2}$ of Sm^{+3} ions. Figure (9) displays the behavior of the peak emission cross-section (σ_{em}) with different concentrations of Sm^{+3} ions in doped and co-doped samples; it indicates that the σ_{em} are variation with the Sm^{+3} ions concentration, it a maximum value for the concentration Sm^{+3} 0.0034% in doped samples, this behavior due to the luminesces quenching related with the O-H vibrations of water and the concentration quenching at higher concentrations, and in the co-doped samples, σ_{em} increases with an increases the concentration of Sm^{+3} ions because of the enhancement in PL intensity of Sm^{+3} ions by Ag NPs, due to the LFE which is induced by SPR of Ag NPs and the energy transfer from Ag NPs to Sm^{3+} ions ($Ag^{+} \rightarrow Sm^{3+}$).

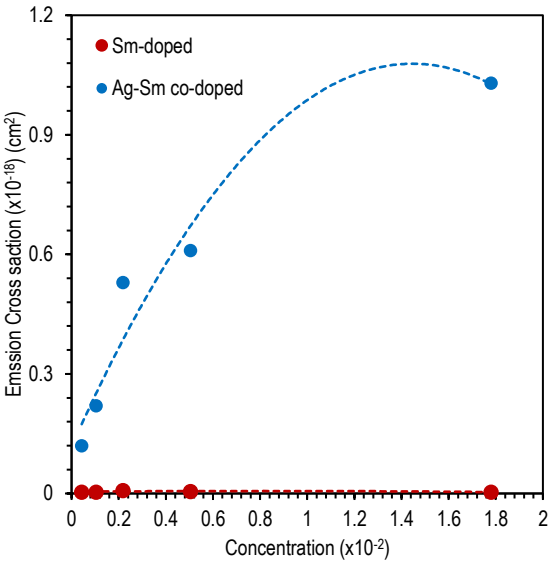

Fig. (9) Variation in peak emission cross-section (σ_{em}) with the concentrations of Sm^{3+} ions in doped and co-doped samples

White emission can be achieved by Ag^{+}-Sm^{+3} co-doping by the enhancement in luminescence intensity of the emission spectra of Sm^{+3} doped, as illustrated in Fig. (10a,b), which displays the luminescence colors of samples as defined by the Commission International de I'Eclairage (CIE) chromaticity diagram. The color coordinate for all samples under 400 nm excitation, figure (10a) shows a chromaticity coordinates of the Sm^{+3}-doped samples and figure (10b) shows positions of a chromaticity coordinates of the light emitted by all a co-doped samples are very close to each other. It can be seen that all the emitted light is white since all the coordinates lie within the white range of the chromaticity chart, a light emitted by AgSm5 are the closest to pure white light (x=0.333, y=0.333). In order to investigate the possibility of the as-synthesized phosphor in application for WLED.

Table (2) The color coordinates of the all samples

Sample	x	y	Sample	x	y
Sm1(B)	0.185	0.169	AgSm1(B)	0.417	0.378
Sm2(C)	0.172	0.170	AgSm2(C)	0.447	0.383
Sm3(D)	0.182	0.255	AgSm3(D)	0.436	0.381
Sm4(E)	0.165	0.219	AgSm4(E)	0.369	0.349
Sm5(F)	0.183	0.280	AgSm5(F)	0.353	0.340

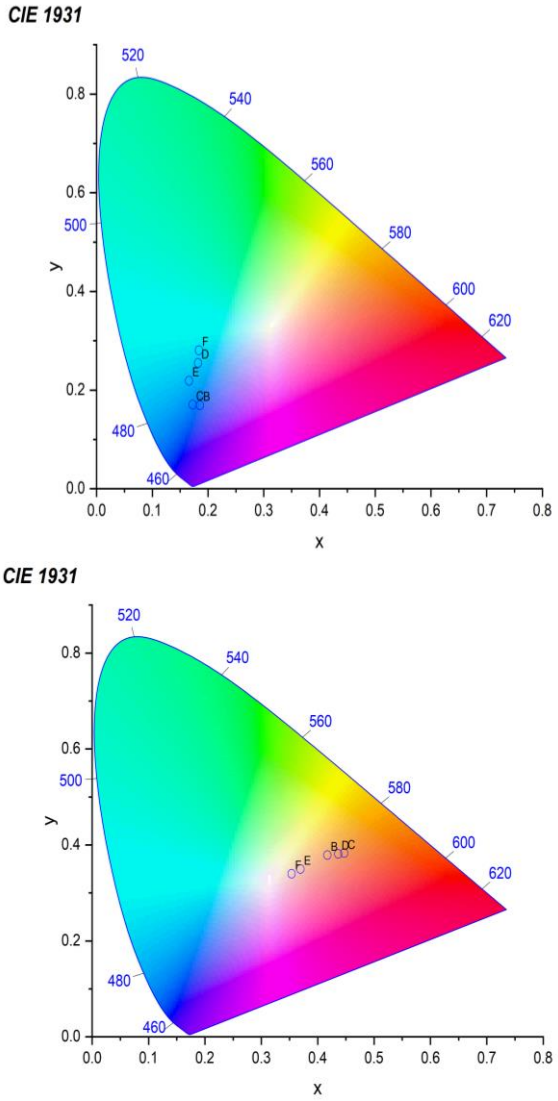

Fig. (10) (a) Chromaticity diagram corresponding to the light emitted from the (a) Sm^{+3}-doped silica, (b) Ag^{+}-Sm^{+3} co-doped silica (excited at 400nm)

4. Conclusions

Silica xerogel has established itself as a viable host material for active ions such as Sm^{3+} and Ag^{+} due to its high transparency, friendliness to the environment, and thermal stability. Spectroscopic analysis of Sm^{3+} ion-doped samples showed luminescence quenching at high doping levels, while the effect of SPR in Ag NPs showed how Ag NPs can enhance the photoluminescence of Sm^{3+} ions in co-doping samples to produce white light, the sample AgSm5 with the concentration $(0.043\text{-}0.0357)\%\times10^{-2}$ is the closest to the white light.

References

[1] P. Pust et al., "Narrow-band red-emitting $Sr[LiAl_3N_4]:Eu^{2+}$ as a next-generation LED-phosphor material", *Nat. Mater.*, 13(9) (2014) 891-896.

[2] M.Y. Chen et al., "Insights into $Ba_4Si_6O_{16}$ structure and photoluminescence tuning of $Ba_4Si_6O_{16}:Ce^{3+}$, Eu^{2+} phosphors", *J. Mater. Chem.*, C3(48) (2015) 12477-12483.

[3] S.P.A. Osorio et al., "Plasmonic Coupling in Er^{3+}:Au Tellurite Glass", *Plasmonics*, 7(53) (2012) 53-58.

[4] M. Reza Dousti et al., "Enhanced frequency upconversion in Er^{3+}-doped sodium lead tellurite glass containing silver nanoparticles", *Eur. Phys. J. D: Appl. Phys.*, 66 (2012) 237.

[5] T. Som and B. Karmakar, "Nanosilver enhanced upconversion fluorescence of erbium ions in $Er^{3+}Er^{3+}$: Ag-antimony glass nanocomposites", *J. Appl. Phys.*, 105 (2009) 013102.

[6] T. Som and B. Karmakar, "Surface plasmon resonance in nano-gold antimony glass–ceramic dichroic nanocomposites: One-step synthesis and enhanced fluorescence application", *Appl. Surf. Sci.*, 255 (2009) 9447-9452.

[7] G.E. Malashkevich et al., "Influence of Silver on the Sm^{3+} Luminescence in "Aerosil" Silica Glasses", *Phys. Solid State*, 50(8) (2008) 1408-1415.

[8] Y. Qi et al., "Enhanced upconversion emissions in Ho^{3+}/Yb^{3+} codoped tellurite glasses containing silver NPs", *J. Non-Cryst. Solids*, 402 (2014) 21-27.

[9] Z. Ashur et al., "Silver nanoparticles enhanced luminescence of Er^{3+} ions in boro-tellurite glasses", *Mater. Lett.*, 112 (2013) 136-138.

[10] J.J. Li et al., "Enhanced luminescence via energy transfer from Ag^{+} to RE ions (Dy^{3+}, Sm^{3+}, Tb^{3+}) in glasses", *Opt. Exp.*, 20(9) (2012) 10122-10127.

[11] Z. Yang, D. Xu and J. Sun, "Synthesis and luminescence properties of $Ba_3Lu(PO_4)_3:Sm^{3+}$ phosphor for white light emitting diodes", *Opt. Exp.*, 25(8) (2017) A391-A401.

[12] M.A. Hamzah et al., "Optical properties of Nd^{3+}:SiO_2 Prepared via Sol-Gel", *Int. J. Appl. Innov. Eng. Manag.*, 3(5) (2014) 495-499.

[13] B.T. Chiad et al., "Study the spectroscopy of samarium encapsulated in silica Xerogel matrices", *Iraqi J. Phys.*, 9(15) (2011) 49-54.

[14] B.T. Chiad, W.A.A. Twej and F.J. Al-Maliki, "Synthesis of Nanosilica Glass Activated by Erbium Ions, Spectroscopic studies", *Iraqi J. Phys.*, 7(8) (2009) 85-92.

[15] B.C. Jamalaiah et al., "Photoluminescence properties of Sm^{3+} in LBTAF glasses", *J. Lumin.*, 129(4) (2009) 363-369.

[16] F.H Ali, "Hydrophilic properties of nano-structure silicate synthesis by sol-gel-dipping technique", J. Phys.: Conf. Ser., 2114 (2021) 012076.

[17] A.H. Hasan and F.H. Ali, "Synthesis of Cr-Doped TiO_2 Using Sol-Gel Technique and Calculation of its Photocatalytic Activity", *Indian J. Nat. Sci.*, 9(51) (2018) 15242-15249.

[18] F.J. Kadhim et al., "Photoluminescence analysis for terbium β-diketonate complex-based silica xerogel matrices", *J. Sol-Gel Sci. Technol.*, 76(1) (2015) 150-155.

[19] A.V. Deepa, M. Priya and S. Suresh, "Influence of Samarium Oxide ions on structural and optical

 ISSN (print) 1813-2065, (online) 2309-1673 PRINTED IN IRAQ

properties of borate glasses", *Sci. Res. Essays*, 11(5) (2016) 57-63.
[20] B.T. Chiad et al., "Study the spectroscopy of samarium encapsulated in silica Xerogel matrices", *Iraqi J. Phys.*, 9(15) (2011) 49-54.
[21] R.B. Figueira, M. de Almeida, and J.R. Silva, "Optical fiber sensors based on sol-gel materials: design, fabrication and application in concrete structures", *Mater. Adv.*, 2 (2021) 7237.
[22] M. Monisha et al., "Reddish-orange emissions from Sm^{3+} doped zinc aluminoborosilicate glasses: A correlative study on structural, thermal, and optical properties", *J. Non-Cryst. Solids*, (2022) 121568.
[23] S.H. Hasan and S.S.M. Alawadi, "Reducing the Purification Period of Congo Red Dye Solution By Using Co-Exposure to Ultraviolet and Green Laser as A Photocatalysit Source", Iraqi J. Sci., 63(5) (2022) 2025-2038.
[24] S.S. Al-Awadi, R.T. Shbeeb and B.T. Chiad, "Effect of Silver Nanoparticles on Fluorescence Spectra of C480 dye", *Iraqi J. Sci.*, 59(1) (2018) 502-509.
[25] Z. Yang et al., "Characterization and luminescence properties of Sr_3GdPO_{43}:Sm^3 orange-red phosphor", *Opt. Eng.*, 54(10) (2015) 105102.
[26] M. Jayasimhadri et al., "Spectroscopic characteristics of Sm3+-doped alkali fluorophosphate glasses", *Spectro. Acta A Mol. Biomol. Spectro.*, 64(4) (2006) 939-944.
[27] L.V. Vu et al., "Synthesis and Optical Characterization of Samarium Doped Lanthanum Orthophosphate Nanowires", *Mater. Trans.*, 56(9) (2015) 1422-1424.
[28] E. Borsella et al., "Structural incorporation of silver in soda-lime glass by the ion-exchange process: a photoluminescence spectroscopy study", *Appl. Phys. A*, 71 (2000) 125-132.
[29] S. Paje et al., "Optical spectroscopy of silver ion-exchanged As-doped glass", *J. Non-Cryst. Solids*, 318 (2003) 239-247.
[30] K. Linganna, Ch. Srinivasa Rao and C.K. Jayasankar, "Optical Properties and Generation of White Light in Dy^{3+}-Doped Lead Phosphate Glasses", *J. Quant. Spec. Rad. Transf.*, 1(18) (2013) 40-48.
[31] M.K. Komal Poojha et al., "A complete analysis of the structural, optical, and gamma-ray attenuation of Dy^{3+} doped modifiers dependent Lead phosphate boro-tellurite glasses", *Optik*, 264 (2022) 169433.
[32] W.A.A. Twej et al., "FTIR Measurements for Structural Probing of Rare earth Sol-Gel Silica Glass System Co-Doped with Al^{3+}", *IEEE Xplore*, 14 (2011) 6369-6375.
[33] E.J. Bowen and F. Wokes, **"Fluorescence of Solutions"**, Langmans, Green (London, 1953).
[34] C.M. Reddy et al., "Optical Absorption and Photoluminescence Studies of Dy^{3+}:LCZSFB Glasses", *Phot. Lett. Poland*, 3(1) (2011) 32-34.
[35] B. Grobelna et al., "Luminescent properties of Sm(III) ions in Ln2(WO4)3 entrapped in silica xerogel", *J. Non-Cryst. Solids*, 353(30-31) (2007) 2861-2866.
[36] D. Kakoti et al., "Effect of ZnS nanoparticles on the Judd-Ofelt and radiative parameters of Sm3+ ions in sol-gel silica matrix", *J. Lumin.*, 211 (2019) 401-412.
[37] I. Aydin et al., "Sol-gel synthesized $Sr_4Al_{14}O_{25}$:Eu^{2+}/Dy^{3+} blue–green phosphorous as oxygen sensing materials", *Opt. Mater.*, 62 (2016) 285-296.
[38] S. Comby and J.-C.G. Bünzli, "Chapter 235 Lanthanide Near-Infrared Luminescence in Molecular Probes and Devices", ed.: K.A. Gschneidner, J.-C. Bünzli, V.K. Pecharsky, Handbook on the Physics and Chemistry of Rare Earths, Elsevier, 37 (2007) 217-470.
[39] B. Grobelna, B. Lipowska and A.M. Kłonkowski, "Energy transfer in calcium tungstate doped with Eu(III) or Tb(III) ions incorporated into silica xerogel", *J. Alloys Comp.*, 419(1-2) (2006) 191-196.
[40] Q. Zhu et al., "Selective synthesis and shape-dependent photoluminescence properties of (Y0.95Eu0.05)2O3 submicron spheres and microplates", *Trans. Nonferr. Metals Soc. China*, 22(10) (2012) 2471-2476.
[41] A.A. Pilarska, Ł. Klapiszewski and T. Jesionowski, "Recent development in the synthesis, modification and application of Mg(OH)2 and MgO: A review", *Powder Technol.*, 319 (2017) 373-407.
[42] K.M.S. Dawngliana and S. Rai, "Linear and nonlinear and optical properties of Sm3+ co-doped alumino-silicate glass prepared by sol-gel method", *J. Non-Cryst. Solids*, 598 (2022) 121929.
[43] A.V. Semchenko et al., "Synthesis of RE-Ag, Al-RE-doped sol-gel glass and films for solar cells", *J. Rare Earths*, 27(4) (2009) 671-674.
[44] J. Fonseca, "Nanoparticles embedded into glass matrices: glass nanocomposites", *Front. Mater. Sci.,* 16 (2022) 220607.
[45] G.C. Righini and M. Ferrari, "Photoluminescence of rare-earth—doped glasses", *Riv. Nuovo Cim.,* 28 (2005) 1–53.
[46] G.E. Malashkevich et al., "Luminescence spectral properties of Sm-and (Ce, Sm)-containing silica gel glasses", *Phys. Solid State,* 40 (1998) 420–426.
[47] C. Wei et al., "Advances in luminescent lanthanide complexes and applications", *Sci. China Technol. Sci.,* 61 (2018) 1265–1285.

APPENDIX

Table (1) The spectroscopic parameters of silica monolith doped with Sm^{+3} ions and co-doped with Ag^{+}/ Sm^{3+}

Sample (doped)	Sm^{+3} ions Concentration ($x10^{-2}$) (%)	Emission Cross Section σ_{em} ($x10^{-21}$) (cm^2)	Oscillator Strength f_{exp} ($x10^{-6}$)	Sample (co-doped)	Sm^{+3}-Ag^{+} ions Concentration ($x10^{-2}$) (%)	Emission Cross Section σ_{em} ($x10^{-18}$) (cm^2)	Oscillator Strength f_{exp} ($x10^{-6}$)
Sm1	1.78	3.5	0.86	AgSm1	1.78-0.0357	1.03	1.97
Sm2	0.505	4.9	0.97	AgSm2	0.505-0.0357	0.61	1.92
Sm3	0.219	7.9	0.98	AgSm3	0.219-0.0357	0.53	1.89
Sm4	0.104	3.7	0.89	AgSm4	0.104-0.0357	0.22	1.81
Sm5	0.043	3.8	0.91	AgSm5	0.043-0.0357	0.12	0.96

 ISSN (print) 1813-2065, (online) 2309-1673

IRAQI JOURNAL OF APPLIED PHYSICS
Vol. 19, No. 4A, October 2023, pp. 37-42

Nabeel A. Areebi

Department of Physics, College of Education, University of Al-Qadisiyah, Al-Diwaniyah, IRAQ

Bandwidth Enhancement for Annular Dielectric Resonator Antenna (ADRA) Using Stacked Technique

The present work focused on a dielectric resonator antenna (DRA), which has many applications in several systems, due to its multitasking possibilities. DR antennas can be fabricated in different shapes like cylindrical, cylindrical ring, rectangular and hemispherical. The proposed antenna is an annular DRA with an operating resonant frequency of 4.3GHz. Narrow bandwidth is the main disadvantage of these antennas. Bandwidth and gain enhancement can be achieved by stacked technique. The two and three annular DRAs are designed and simulated via finite-difference time domain (FDTD) method. Large bandwidth and better radiation power are achieved. The best result obtained for the bandwidth is 51.77% with three annular DRAs. Several parameters like return loss, directivity pattern and input impedance are calculated. Moreover, the stacked technique is used for increasing the bandwidth and directive gain in order to enhance the antenna's performance.

Keywords: Bandwidth, Dielectric Resonator Antenna, FDTD method, Stacked-technique
Received: 02 May 2023; **Revised:** 12 June 2023; **Accepted:** 17 June 2023

1. Introduction

Recently, the communications have developed widely and the dielectric resonator antenna (DRA) played a curial role in this developing due to its multitasking possibilities which made it have many advantages in several applications. One of most applications in high-performance spacecraft, satellite and missile [1]. One of the most crucial antenna parts for a variety of microwave and millimeter wave communications applications is now thought to be the tiny microstrip patch antenna. An essential aspect of the microstrip antenna is its ability to readily change its specific bandwidth by changing the form, thickness, or use of a multi-layered substrate or stacked technique [2]. For years ago, dielectric resonator antennas (DRAs) have preliminary been used into microwave circuits (as filters and oscillators for example). Within reason these traditional applications, the dielectric resonator (DR) was normally treated as a devices of the energy storage alternatively a radiator. Open DR was established to radiate for years before [3-5]. The DRAs are distinguishable structures that offer freedom in selecting the dimensions and types of the substrate used. A broad range of dielectric constant of 6 to 100 are used in many shapes of DRA (elliptical, cylindrical, and rectangular). The great features of the DRA are large bandwidth, high efficiency and mechanical simplicity [6,7]. One drawback of these standard DRAs is their narrow bandwidth (BW). The percentage of BW up to 11%, for a pure rectangular DRA configuration, can be achieved. Several techniques have been used to improve the BW of DRA. For example, is to reduce size of the DRA, in which the middle part of the DRA is elude, to improve the BW about 28%. Geometric modifying of the DRA into several shapes, like a conical DRA, slot cylinder and truncated tetrahedron, is another approach to enhance the bandwidth. Using U-shaped DRA, bandwidth can be increased to 42% [8,9]. Liu et al. [10] was presented a broadband-notched reconfigurable DRA for wideband performance. They showed that a multiple resonant modes for the rectangular DR fed by feed line can be generated. One of methods used to enhance bandwidth is changing the shape of the dielectric resonator. Moreover, using DRA with a dielectric resonator of the lowest dielectric constant increases its bandwidth and electromagnetic (EM) energy. Increasing the bandwidth can be achieved using the multi-layer approach with different modes of excitation and different permittivities in the DRA [11]. DRAs have a much broader BW compared with a microstrip antenna. The DRAs made utilized of mode radiated of a DR, while the microstrip antennas can be radiated only out of two narrow radiation holes. Comparing with microstrip antenna, DRAs are preferable because of high radiation efficiency due to the absence of surface waves and grounded planes. Avoidance of surface waves is another advantage of DRA over the microstrip antenna. However, the DR antenna and the microstrip antenna behave like resonant cavities. Other characteristics are shared between them. The DR can be used as an antennas at 1983 where the first work on the cylindrical Dielectric Resonator Antenna was achieved [12-14]. There are several advantages of DRA. DRA can be integrated with monolithic microwave integrated circuit (MMIC) as results of their small-size. They can be manufactured in different shapes (cylindrical,

rectangular, hemispherical and cylindrical rings, and have more design flexibility. Because of the low dissipation factor of dielectric materials, DRA is a low-loss antenna. Various feeds, such as slot, coplanar lines, microstrip lines, waveguide slots, dielectric image guides and probes, can be used to excite DRA [15-17]. Several techniques are used to enhance bandwidth, such as multi-segment DRA, single DRA, parasitic DRA and introducing a gap between the ground plane and DRA. A bandwidth of around 10% has been achieved by a single DRA with low permittivity. Parasitic DRA introduces high gain and can improve the BW up to 17%. BW up to 20% using multi-segment DRA can be achieved. Introducing a gap between the ground plane and DRA gives a typical BW of about 30% [18,19].

2. Annular Dielectric Resonator Antenna

Annular DRA can be used to prevent mode degeneracy and to lower Q factor and increasing the bandwidth [17]. The basic structure of (ADRA) is shown in Fig. (1). The excitation was chosen by a probe feed method for several reasons including providing less spurious radiation from the probe current, in addition, to the simplicity in theoretical engineering installation and practical manufacturing [20]. The ground plane of the DRA is a metal and the dielectric annular is of a dielectric constant ε_r and having thickness (d) with radius (a). In practical applications, the dominant mode are interested, which has the lower resonant frequency [21].

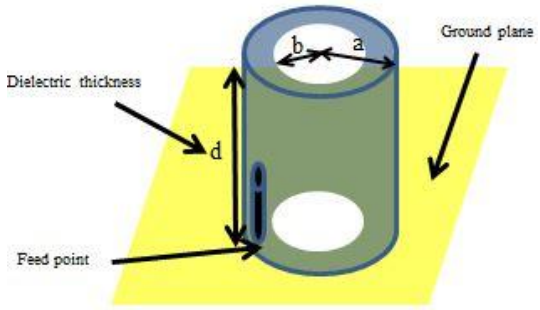

Fig. (1) The geometry of annular DRA

3. Finite Difference Time Domain (FDTD) Method

The FDTD method is a numerical technique used to solve field equations which are directly subject to imposed boundary constraints by the geometric structure. The FDTD method is extremely useful in simulating complex configuration because it provides a direct integration of time- depending Maxwell's equations. Compare with the method of moment and the finite element method, the FDTD method distinguished by the fact that it is a time domain technique [22]. The FDTD method depends on the volume and requires dividing the solution space into a uniform network of cells. The components of the electric field (E) and magnetic field (H) are distributed around each cell, where the E and H fields are calculated using the method of time increments. It allows the instantaneous response of any electromagnetic system. In other words, by increasing time, the components of the E and H fields are calculate at this time. These fields recalculated again after each time increment until the value of these fields within the system reaches zero, using Fourier transforms to extract the values in terms of frequency. Yee suggested that the FDTD space consists of size identical cells ΔxΔyΔz called (Yee cells) and the electric and magnetic fields components spread around each cell. E-field component surrounded by four magnetic fields components and each magnetic field component surrounded by four electric fields components, as shown in Fig. (2) . The cell's size is defined by the highest frequency, hence it must be smaller than $0.1\lambda_{min}$, and the step time in the FDTD space is determined by the relationship $\Delta t \leq \Delta x/c\sqrt{3}$, where Δt represents the step time, Δx represents the cell dimension[23,24].

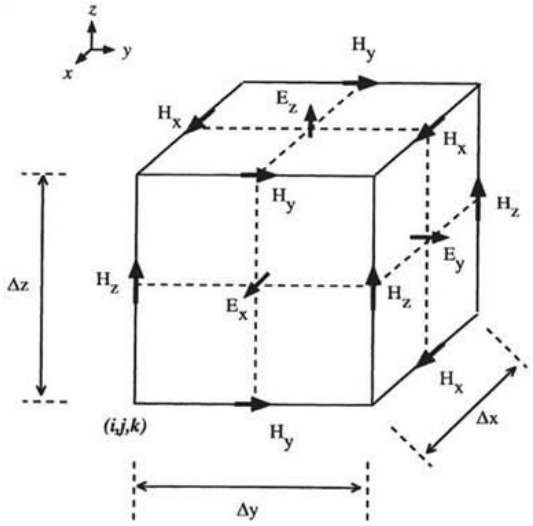

Fig. (2) Yee's cell FDTD in 3D

The system is excited by an electrical impulse that is mathematically represented by a Gaussian function in the time domain called a Gaussian pulse [23]:

$$p(t) = e^{-\left(\frac{t-t_0}{\tau}\right)^2} \quad (1)$$

where τ is a damping factor that relates to the pulse width and has a value that varies based on the problem's frequency band and is the time of pulse delay. The method of programming in infinite space, a perfectly matched layer is used. The values of the wave's compounds diminish and become very small as the wave propagates through space, compared to the values of the compounds at their greatest values. Fourier transformations can be used to calculate the values of impedance ($Z_{in}=R+iX$) after N calculations, where R and X represent resistance and recidivism, respectively. Input impedance in the frequency domain is [25].

$$Z_{in}(\omega) = \left(\frac{\int_{-\infty}^{\infty} V(t)e^{-j\omega t}dt}{\int_{-\infty}^{\infty} I(t)e^{-j\omega t}dt}\right) \quad (2a)$$

 ISSN (print) 1813-2065, (online) 2309-1673

$$Z_{in}(\omega) = \frac{\sum_{n=0}^{N} V(n\Delta t)e^{-j\omega n\Delta t}\Delta t}{\sum_{n=0}^{N-1} I\left(\left(n+\frac{1}{2}\right)\Delta t\right)e^{-j\omega\left(n+\frac{1}{2}\right)\Delta t}\Delta t} \quad (2b)$$

Where $V(t)$ is the voltage in the time domain calculated from Faraday's law, and $I(t)$ is the electric current in the time domain calculated from Ampere's law, and return loss in the frequency domain is calculated as:

$$S_{11} = \left(\frac{\int_{-\infty}^{\infty} V(t)e^{-j\omega t}dt}{\int_{-\infty}^{\infty} p(t)e^{-j\omega t}dt}\right) \quad (3a)$$

$$S_{11} = \frac{\sum_{n=0}^{N} V(n\Delta t)e^{-j\omega n\Delta t}\Delta t}{\sum_{n=0}^{N} p(n\Delta t)e^{-j\omega n\Delta t}\Delta t} \quad (3b)$$

4. Design of Annular DRA (ADRA)

The ADRA is fed by the coaxial probe technique. Feed point is determined using the try and error method in order to matching impedance. ADRAs have more interested use in wireless applications. It is a radio antenna morally used a microwave and millimeter frequencies that consist a block of ceramic material [26]. In current work, the standard operating resonant frequency is 4.3 GHz and the ADRA proposed with dielectric constant ε_r=10.2, thickness (d) of 8 mm and radius a=4 mm and b=2 mm. The simulated and designed results of ADRA with the optimum dimensions are shown in Fig. (3).

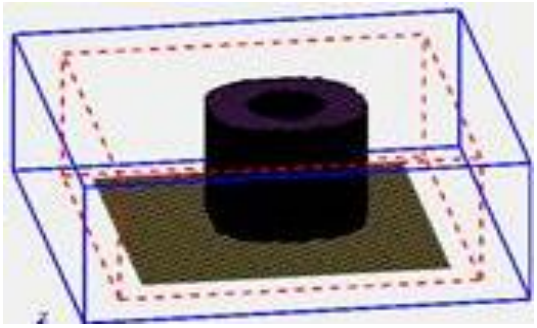

(a)

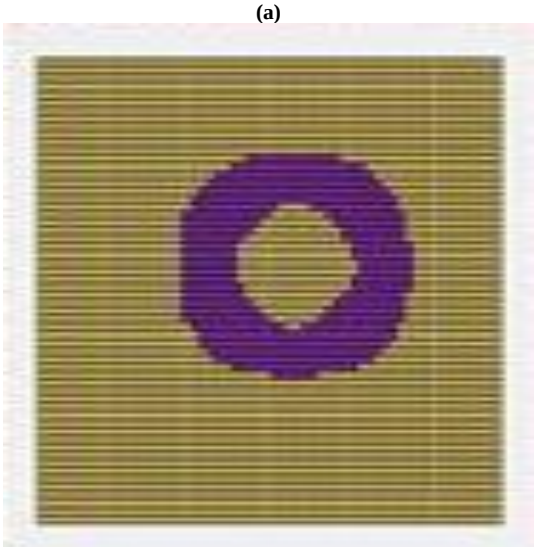

(b)

Fig. (3) ADRA proposed and calculated by FDTD method (a) side view (b) top view

5. Results and Discussion

5.1. Resonant Frequency and Input Impedance

Simulation results of input impedance (Z_{in}) are presented. Both of the resistance (real part) and the reactance (imaginary part) are plotted in Fig. (4). At the moment where the reactance value is zero, f_r=4.298 GHz and input impedance Z_{in}=50 Ω. Impedance matching between transmisssion line and DRA is very necessary. This matching causes transmisssion the higher amount of power from transmisssion line to the DRA.

5.2. Reflection Coefficient or Return Loss (RL or S_{11}) and Bandwidth

Figure (5) shows that the calculated value of return loss (-33.75 dB) and the resonant frequency is f_r=4.298 GHz. Bandwidth is calculated from the two frequencies values at sides of a -10 dB return loss. The percentage of bandwidth is 1.46%. Return loss is a measurement of reflected energy at a specific frequency, with the greater the radiated energy versus the lower the return energy. When the return loss is 0 dB, all of the power is returned to the source, However when the return loss is -33.75 dB, only a small portion of the incident energy is returned, and the majority of the incident energy is radiated.

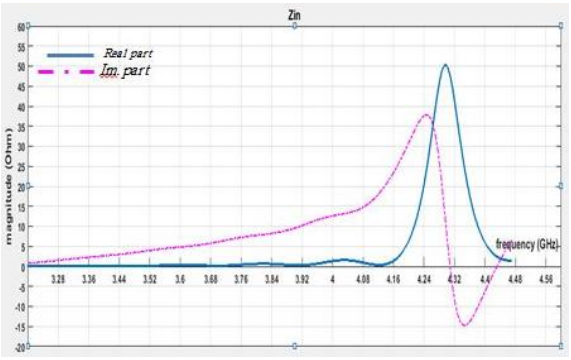

Fig. (4) Input impedance versus frequency calculated by FDTD method

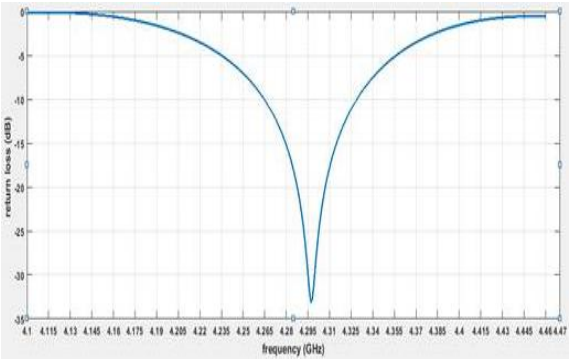

Fig. (5) Return loss versus frequency calculated by FDTD method.

5.3. Design of Two ADRAs

The proposed DRA is designed and simulated by FDTD method. Figure (6) shows the simulated results for two identical ADRAs, which have the same size. These two DRAs have different dielectric constants. One dielectric is aluminum nitride having a dielectric constant of 8.6, and the other is RT/Duroid 6010 with a dielectric constant of 10.2. The lower is fed by a coaxial probe, while the upper by electromagnetically coupled. Values of the return loss coefficients and resonant frequency are shown in Fig. (7). From these results, it is shown an increasing in BW from 1.46 to 18.05 % as a result of this design (stacked). The return loss coefficient (S_{11}) increased also. The resonant frequency was not significantly affected by this technique.

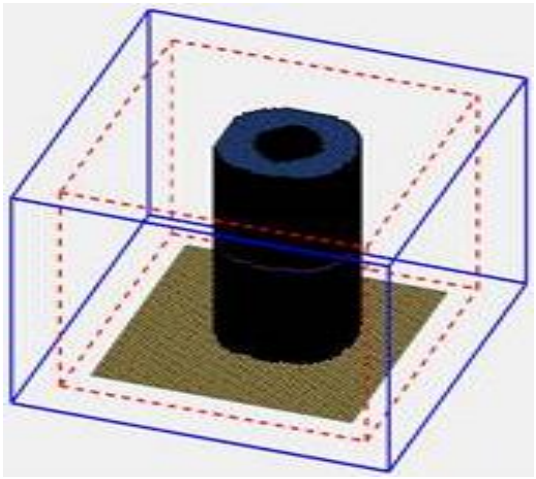

Fig. (6) Stacked technique for two identical ADRAs

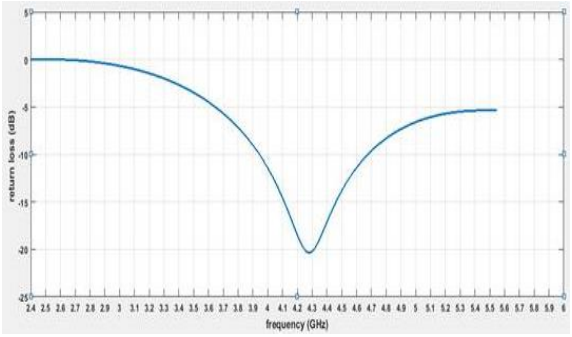

Fig. (7) Return loss (S_{11}) for two annular DRAs

5.4. Design of Three ADRAs

Next, the proposed design is to add another annular dielectric. Three annular DRAs are designed of equal thickness and radius, 8 and 4mm, respectively, as shown in Fig. (8). By adding a third annular which is Dupont 943 having dielectric constant of 7.4. The range of the resonant frequency increased to be 3.02 to 5.13 GHz. The bandwidth percentage increased to 51.77%, as shown in Fig. (9). The increase in bandwidth is mainly due to the increased thickness of the dielectric medium, and the decreased effective of dielectric constant. In addition to the previously mentioned reasons, bandwidth increased as a result of fringe fields creation.

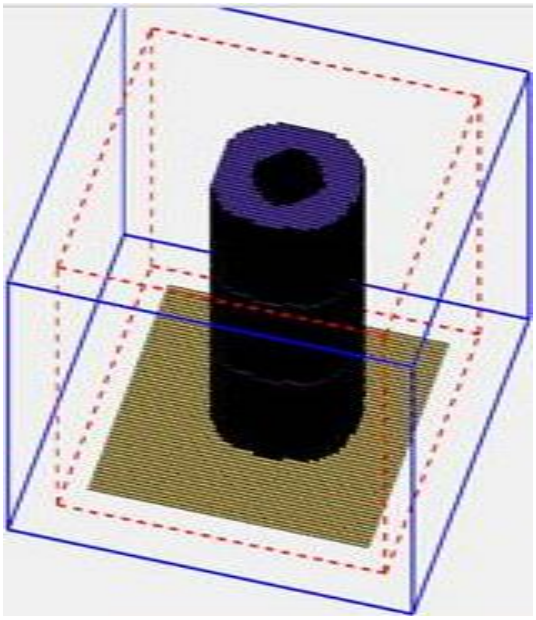

Fig. (8) Stacked technique for three identical ADRAs

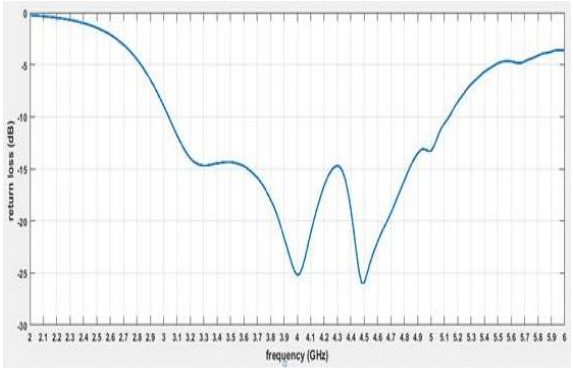

Fig. (9) Return loss (S_{11}) for three annular DRAs

It is important to mention that the amount of fringe fields depends on the antenna size as well as the thickness of the dielectric medium. The fringe fields increased as the thickness of the dielectric substrate increased. Values of the directivity pattern shown in Fig. (10) are explicated an increasing the directive gain and enhancement antenna's performance. Directivity can be calculated using the equations from Elsherbeni and Demir [23]. The polar representation of the field distribution in the two planes (E and H) is illustrated in figures (10a), (10b) and (10c), respectively.

 ISSN (print) 1813-2065, (online) 2309-1673

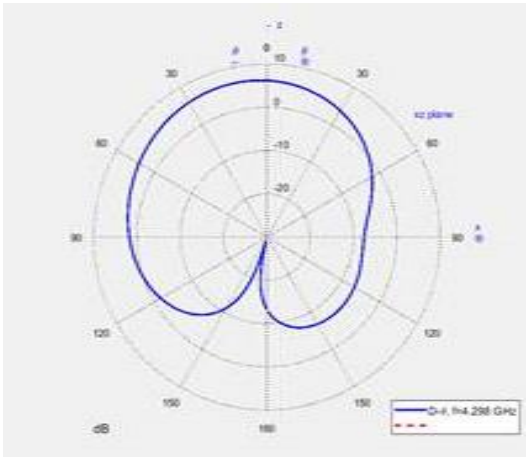

(a)

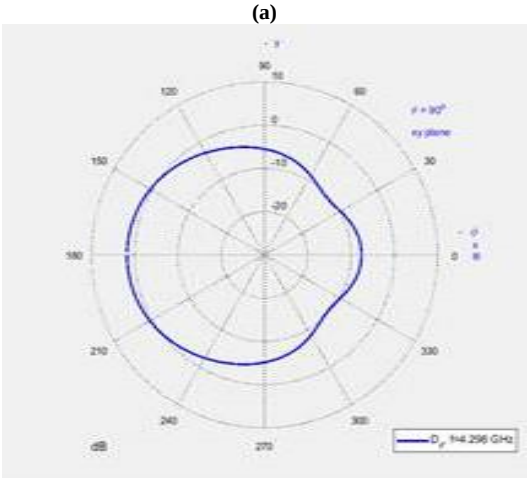

(b)

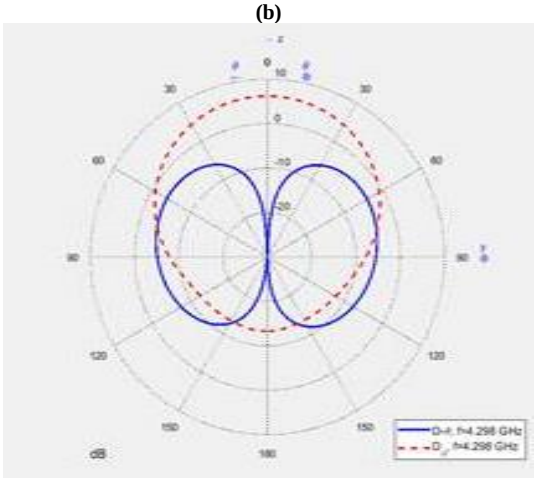

(c)

Fig. (10) Directivity patterns for three annular DRAs (a) in x-y plane, (b) in x-z plane, and (c) in y-z plane

6. Conclusions

In concluding remarks, the FDTD method was used to design and simulate ADRAs. The stacked technique has played a vital role in enhancing ADRA's performance. The better directivity and the coefficients of return loss were improved as a result of three stacked annular DRAs. Hence, this study confirmed that using stacked technique increased the value of the bandwidth and improved the directivity (7.17 dB) with increasing the return loss coefficients.

Acknowledgements

The author would like to thank the Department of Physics, College of Education, University of Al-Qadisiyah, Ministry of Higher Education and Scientific Research of Iraq for finical support for this study.

References

[1] M.N. Naik and C.R. Prashanth, "Design of compact annular ring microstrip antenna for multiband communication system," *J. Network Commun. Emerg. Technol.*, 7(8) (2017) 24-28.

[2] S.N. Ali, F.S. Atallah and A.H. Muhammad, "Design and Simulation of Rectangular Microstrip Patch Antenna Using a Computer Simulation Technology Operating at 4.5GHz ", *Iraqi J. Appl. Phys.*, 19(2) (2023) 53-55.

[3] R.D. Richtmyer, "Dielectric Resonators," *J. Appl. Phys.*, 10 (1993) 391-398.

[4] M. Gastine, L. Courtois and J.L. Dormann, "Electromagnetic resonances of free dielectric spheres", *IEEE Trans. Microwave Theory Tech.*, 15 (1967) 694-700.

[5] O. Sager and F. Tisi, "On eigenmodes and forced resonance-modes of dielectric spheres", *Proc. IEEE*, 56(9) (1968) 1593-1594.

[6] G. Hamed, L. Osman and K. Latrach, "Circularly polarized two layers conical DRA based on metamaterial", *Microwave Opt. Technol. Lett.*, 59(8) (2017) 1913-1919.

[7] N. RajaSekhar et al., "Performance Analysis of Conical Dielectric Resonator Antenna with Various Feeding Techniques", *2019 IEEE Indian Conf. on Antennas and Propogation (InCAP)*, Ahmedabad, India (2019) 1-4.

[8] S. Kohar, S. Singh and A. De, "Design of low profile cylindrical conformed microstrip patch antenna for wideband operation," *Int. J. Electron. Lett.*, 9(4) (2021) 1-10.

[9] D. Soren et al., "Dielectric Resonator Antennas: Designs and Advances", *Prog. in Electromag. Res. B*, 60 (2014) 195-213.

[10] S. Keyrouz and D. Caratelli, "Dielectric Resonator Antennas: Basic Concepts, Design Guidelines, and Recent Developments at Millimeter-Wave Frequencies", *Int. J. Antennas Propag.*, 2016, Article ID 6075680, 20 pages.

[11] F. Saeed, H. Oraizi and M. Ladislau, "Gain improvement of rectangular dielectric resonator antenna by engraving grooves on its sidewalls", *IEEE Antennas Wireless Propag. Lett.*, 16 (2017) 2167-2170.

[12] S.A. Long, M.W. McAllister and L.C. Shen, "The resonant cylindrical dielectric cavity antenna", *IEEE Trans. Antennas Propag.*, 31 (1983) 406-412.

[13] A. Al-Azza et al., "Stacked Conical-Cylindrical Hybrid Dielectric Resonator Antenna for Improved Ultra wide Bandwidth", *Prog. in Electromag. Res. Lett.*, 79 (2018) 79-86.

[14] A. Sharma, "Bandwidth Enhancement Techniques of Dielectric Resonator Antenna", Int. J. Eng. Sci. Technol., 3(7) (2011) 5995-5999.
[15] M.I. Sulaimam et al., "Bandwidth Enhancement of a Circularly Polarized Cylindrical DRA Using Multi-Dielectric Layers", *J. Artif. Intelleg.*, 9(4) (2016) 56-64.
[16] A.R. Mishra and R. Gupta, "Three Cylindrical Stacked DRA Excited by Coaxial Feeding for Wideband Radiation Pattern", *Int. J. Eng. Sci. Technol. Manag. Appl. Sci.*, 3(Special Issue) (2015) 199-204.
[17] J.F. Zurcher and F.E. Gardiol, **"Broadband Patch Antenna"**, Artech House (London, 1995) 51-53.
[18] A.R. Mishra and R. Gupta, "Study of a Conical DRA Array with Enhanced Bandwidth and Gain for C-band Applications", in Conf. 18th IEEE-Mediterranean Microwave Symp. (MMS), 2018.
[19] K.S. Naik, D.S. Kiran and S. Aruna, "High permittivity design of rectangular and cylindrical dielectric resonator antenna for c-band applications," *Adv. Sci. Technol. Lett.*, 147 (2017) 34-41.
[20] L. Zou, "Dielectric Resonant Antennas: From Multifunction Microwave Devices to Optical Nano-antennas", Ph.D. dissertation, Adelaide University (Australia, 2013).
[21] I. Ali et al., "Wideband and high gain dielectric resonator antenna for 5G applications", *Bull. Electr. Eng. Inform.*, 8(3) (2019) 1047-1052.
[22] M.M. Al-Hillo, "Bandwidth enhancement for circular-shaped microstrip antennas using FDTD method", Ph.D. dissertation, Basrah University (Iraq, 2012).
[23] N.A. Areebi, "New Design on Cylindrical Rectangular Microstrip Antennas and its Characteristics Using FDTD method", Ph.D. dissertation, Basrah University (Iraq, 2020).
[24] A.Z. Elsherbeni and V. Demir, "Introduction to FDTD: The finite-difference time-domain method for electromagnetics with MATLAB simulations", SciTech Pub., (NC, 2009).
[25] A. Taflove, **"Computational Electrodynamics: The Finite-Difference Time-Domain Method in Computational Electrodynamics II"**, vol. 3, 2nd ed., Artech House (Norwood, 1996).
[26] S.V. Rani et al., "Design and Analysis of Cylindrical Stepped C-Shaped Dielectric Resonator Antenna for C-Band Applications", *J. Electron. Commun. Eng.*, 11(2) (2016) 61-65.

 ISSN (print) 1813-2065, (online) 2309-1673

IRAQI JOURNAL OF APPLIED PHYSICS
Vol. 19, No. 4A, October 2023, pp. 43-48

Shatha H. Mahdi
Hanaa S. Mahmood
Kareem A. Jasim

Department of Physics, College of Education for Pure Sciences / Ibn Al-Haitham, University of Baghdad, Baghdad, IRAQ

Mechanical Properties and Surface Morphology of Polyester Resin Supported by Titanium Oxide Nanoparticles

Several nanocomposites dispersed with TiO_2 nanoparticles reinforced with unsaturated polyester resin were fabricated at different filler ratios. Nano-sized TiO_2-polyester resins were prepared throughout the poly-condensation reactions. The nanocomposite samples were characterized by morphology, hardness, strength and thermal insulation. The scanning probe microscopy showed that the particles are almost uniformly distributed in the samples, while increasing the content of nanoparticles led to the formation of some agglomerations. The hardness and strength results showed that 0.2% TiO_2 nanoparticles were the optimum ratio, depending on hardness and thermal conductivity results. This 0.2% ratio leads to the improvement of polyester resin samples and it is chosen to make a dental filling with other additives.

Keywords: Polyester resin; TiO_2 nanoparticles; Nanocomposites; Surface morphology
Received: 19 April 2023; **Revised:** 02 June 2023; **Accepted:** 09 June 2023

1. Introduction

Unsaturated polyester resin (UPR) is a type of synthetic copolymer used to fabricate fibers, coatings, and composites [1]. Various products in numerous fields can be synthesized with a wide range of qualities depending on the curing agents, fillers, and regulators utilized [2]. They are interesting because of the inexpensive cost of production. UPR has been extensively studied in numerous studies due to its high chemical resistance and cross-linking ability [3]. It is used in many applications since it has broadly integral components with a large field of characteristics [4]. Unsaturated polyester is often synthesized as a viscous liquid through the melt condensation of an aromatic dicarboxylic acid such as phthalic acid or anhydride with polyhydric alcohol and unsaturated dicarboxylic acid or anhydride [5]. There are numerous types of resins that are used in furniture composite applications [6]. Polyester resins have been used in many fields of our lives, including manufacturing many components in the construction and automobile industries, including wall panels, ceilings, etc. [7]. Cobalt compounds are added to polyester resins for proper curing or for the purpose of the solidification process. Polyester resin is chiefly collected from monomers, which are the basic building elements [8-10]. Depending on the resin type required, the chemical compositions of such monomers are changed. During the curing process, a reactive diluent, usually styrene, binds the polymer chains by free radical copolymerization and then hardens. The strength of the final product is determined by cross-link density. The process starts with an initiator, which is commonly a peroxide, which decomposes into highly reactive molecule fractions that initiate a chain reaction [11-13]. As the resin dries at a normal temperature, the accelerators activate the initiator, increasing its breakdown. Accelerators are virtually always cobalt metal salts. According to the final product, the amount of cobalt accelerator used but small amounts of cobalt can highly affect the final product, making it strong or flawed [14].

Recent advances in the composite materials field are related to the addition of nanoparticles (NPs) such as carbon nanotubes (CNTs) to improve thermal, mechanical, or electrical properties [8]. Also, nano-clays are broadly used in numerous industries, such as architecture [9] or fire safety substances [10,11]. The properties of nanocomposites depend on the dimensions and dispersion of nanoparticles [12]. Due to the high surface area of nanoparticles, a small amount in the matrix can provide a wide surface for polymer/filler interactions. Different metal oxide nanoparticles have been used as filler materials to alter the mechanical properties or enhance thermal conductivity [13], such as ZnO [14], Fe_2O_3 [15], and nano-alumina [16]. Titanium dioxide is commercially available in the form of powder that shows the largest surface area [17]. Polymer nanocomposites comprise a new class of materials with nanoscale particulates [18]. The mechanical properties of the composites filled with filler nanoparticles are better than those of micro-sized materials of the same material [19]. Rahman et al. have studied the mechanical, electrical, and optical properties of UPR composed of $NiFe_2O_4$ nanoparticles and they have found that the tensile properties were enhanced with $NiFe_2O_4$ nanoparticles, which reduced the sample's elasticity [20,21]. Blanco et al. have studied the effect of TiO_2

NPs on preparing photocatalytic nanocomposites with improved infrared reflectance properties. The nanocomposites were prepared by dispersing 0-20 wt.% of TiO_2 NPs in the matrix. The total solar reflectance greatly increased, as did the color change in the improved resin [22].

In this study, we concentrated on improving the mechanical and thermal characteristics of polyester resin by reinforcing it with TiO_2 NPs composite. These results would be chosen for the fabrication of a dental filling with other additions.

2. Experimental Part

Unsaturated polyester resin from Merck Chemicals Limited with a density of 1.10-1.20 g/cm^3 and melting point between 135 and 165 °C was used. Cobalt actuates of 3% metal content, titanium (IV) oxide, anatase nanoparticles of 25 nm particle size, 99.7% trace metal basis from Sigma-Aldrich, and commercial methyl ethyl ketone peroxide (from Sr Polychem) were also used.

The UPR was mixed with the 2 wt.% curing agent, which is cobalt, according to the amounts mentioned in table (1) for each sample. The TiO_2 NPs were added with different percentage weights (0.1 to 0.6%) as mentioned in the same table to the polyester-curing agent and mixed well for 15 minutes, after which the methyl ethyl ketone peroxide (MEKP) hardener was added and the mixing was continued for an additional five minutes. Then the samples were poured into cylindrical molds with a diameter of 20 mm and thickness of 15 mm. The samples were left for 24 hours and then placed in the oven at 50 °C.

Table (1) The sample's contents of resin weight, curing agent weight, and TiO_2 weight

Sample	Resin Weight (g)	Curing Agent Weight (g)	TiO_2 Weight (g)	Total Weight (g)
A	97.941	1.959	0.1	100
B	97.843	1.957	0.2	100
C	97.745	1.955	0.3	100
D	97.647	1.953	0.4	100
E	97.549	1.951	0.5	100
F	97.451	1.949	0.6	100

The scanning probe microscope (SPM) is used in the field of nanotechnology to study and map the surface topography of nano- and micro-dimensions. In this work, a AA3000 SPM instrument was used. Shore-hardness measurements were performed using the hardness tester model (TH220). A standardized press steel foot of 1.4 mm diameter was used, with a 30° conical point and a 0.1 mm tip radius. The indenter was measured after applying force on the material for 15 s. The compression test was done by placing the sample under press until the point of fracture to find the compression yield and strength. The thermal conductivity test for the prepared blend samples was completed by Lee's disc method (from Griffin & George, England). The sample and the three discs were cleansed, placed in their positions, and tightened firmly. The heater disc was supplied with 6 V and the disc's temperatures were measured by the thermometers after steadying for 5 mins. The final reading was measured after 20 min. of the initial reading.

3. Results and Discussions

Figures (1-3) illustrate the 2D SPM images of the polyester resin reinforced with TiO_2 NPs (0.1, 0.2 and 0.3 wt.%) of the samples with size of 3023nm, 3045 nm, 2621-2552nm and 2568-2517nm, respectively. Some particles appeared on the surface with average diameter of 97.37nm, 90.33nm and 101.41nm, respectively, as shown in tables (2), (3) and (4) (see the appendix), while figures (4-6) illustrate granularity cumulation distribution charts of these samples. SPM images illustrate that the particles are approximately uniformly distributed. The distribution of these nanoparticles in the composites is the main basis of successful reinforcement by crosslinking polymer chains with network structure [23,24]. The bonds added to the network of polymers restrict the stretching of chains, reduce the sample's elasticity, and enhance its stiffness. Increasing the content of nanoparticles caused the formation of some agglomerations, some of which appeared on the sample surface [25]. These clumps may weaken the sample's ability to hold the stresses imposed on it.

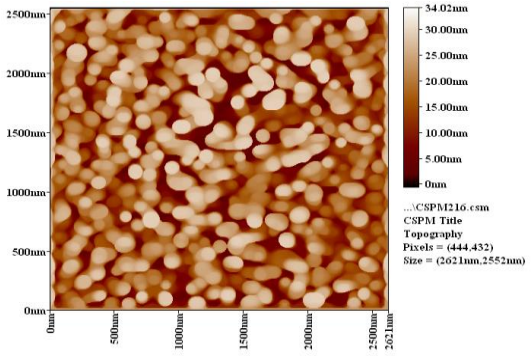

Fig. (1) SPM images, a two-dimensional image for the polyester resin reinforced by 0.1 wt.% NTPs of the sample with a size of 3023nm, 3045nm

Figure (7) displays the hardness variation for the solid resin sample prepared with different weight percentages of TiO_2 NPs using the shore D hardness test. It appears that the hardness increases from 81 to 87.3 as the content of TiO_2 NPs is increased from 0 to 0.2% and decreases to 75.6 at 0.6%. This result is consistent with previous studies [9]. Low TiO_2 NPs ratios enhance the interaction between the polymer chains by crosslinking, while higher ratios cause aggregation between the nanoparticles and restrict the joint between the host matrixes. The shore hardness values for the improved blends are good when compared with previous works [25,26].

 ISSN (print) 1813-2065, (online) 2309-1673

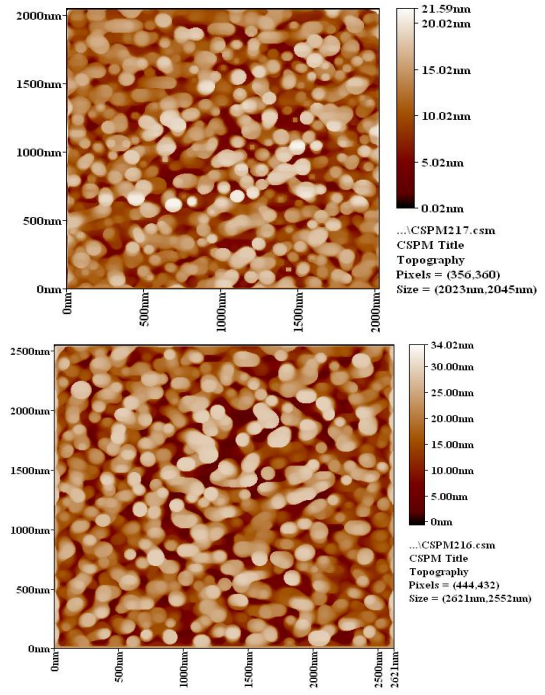

Fig. (2) SPM images, a two-dimensional image for the polyester resin reinforced by 0.2 wt.% NTPs of the sample with a size of 2621-2552nm

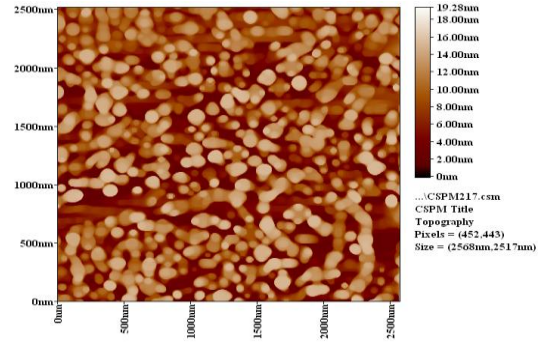

Fig. (3) SPM images, a two-dimensional image for the polyester resin reinforced by 0.3wt.% NTPs of the sample with a size of 2568-2517nm

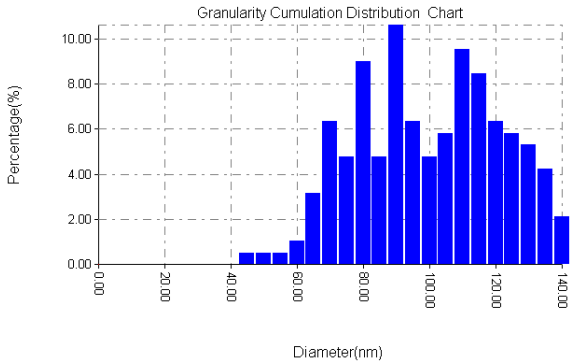

Fig. (4) Granularity cumulation distribution chart for the polyester resin reinforced by 0.1 wt.% NTPs of the sample

Figure (8) shows the deviation of the compression yield and strength of the nanocomposites with the TiO_2 NPs. It appears that the compression yield contrasts with the maximum strength of 24.5 MPa at TiO_2 NPs content of 0.2%. The reinforcement of the polyester resin with a specific amount of TiO_2 NPs significantly enhanced the mechanical properties of the samples by increasing their stiffness, as shown by the AFM results.

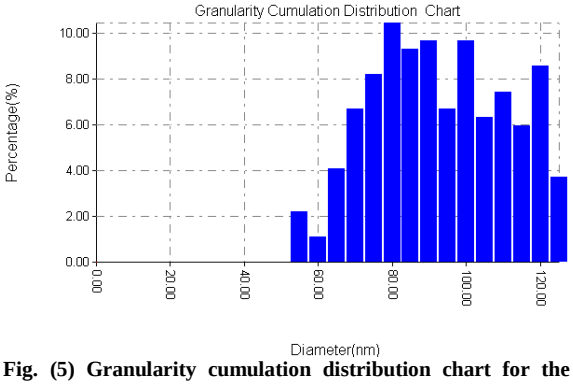

Fig. (5) Granularity cumulation distribution chart for the polyester resin reinforced by 0.2 wt.% NTPs of the sample

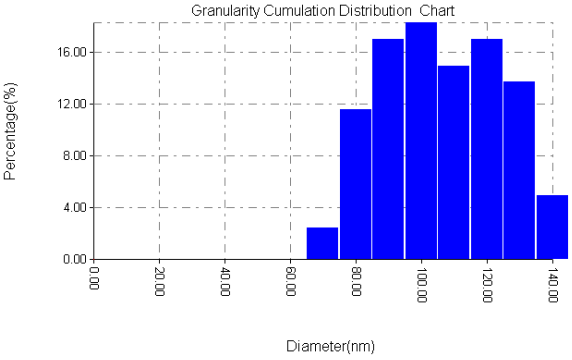

Fig. (6) Granularity cumulation distribution chart for the polyester resin reinforced by 0.3 wt.% NTPs of the sample

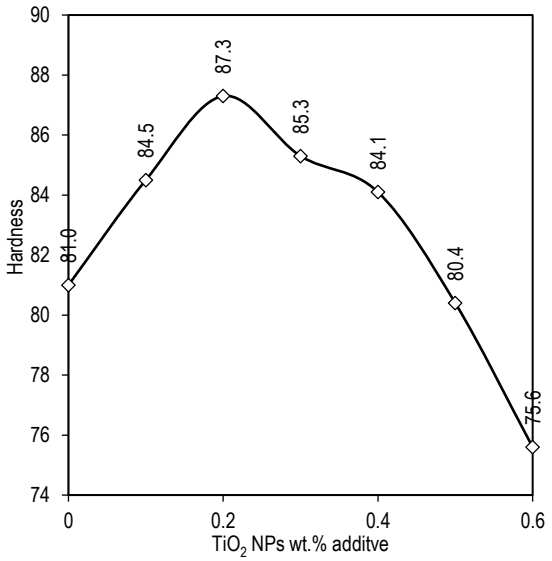

Fig. (7) The variation of hardness of the nanocomposite versus the TiO_2 NPs wt.% additive

Thermal conductivity is a property that defines the specific heat flow through a material due to a thermal gradient [27,28]. The higher the thermal conductivity, the better a substance conducts heat. Several important applications of thermal conductivity exist [29,30]. Figure (9) shows the variation of the thermal conductivity constant of the composite samples with the percentage content of TiO_2 NPs. Thermal

conductivity was enhanced, where the coefficient increased from 0.33 W/m.K for the samples free of TiO_2 NPs to 0.35 W/m.K for the sample with at 0.2% of TiO_2 NPs, and reduced to 0.29 W/m.K at 0.6% TiO_2 NPs. The increment of thermal conductivity owing to the added crosslinking occurs between the polymer chains [31] with the assistance of the added TiO_2 NPs or owing to the contribution of the charge carriers of the added TiO_2 NPs as a result of oxygen vacancies in TiO_2.

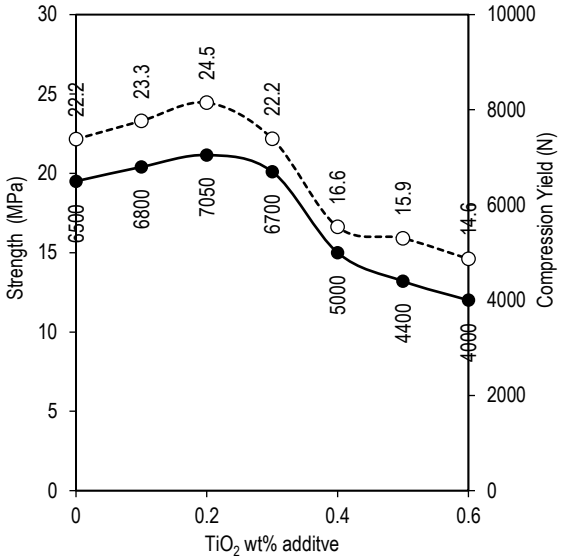

Fig. (8) The variation of compression (solid line) and strength (dotted line) of the nanocomposites with the TiO_2 NPs wt.% additve

4. Conclusions

In this paper, the mechanical properties, including hardness, compression, and strength, in addition to thermal conductivity, of TiO_2-reinforced saturated polyester resin nanocomposites at different ratios were tested. Incorporation of the TiO_2 NPs within the UPR enhanced the mechanical and thermal conductivity at TiO_2 NPs content of 0.2%. The hardness, compression, and strength of the nanocomposite samples increased from 81, 22.2 MPa, and 6500 N in the pure sample to 87.3, 24.5 MPa, and 7050 N, respectively, while increasing the TiO_2 NPs content weakened the interaction between the nanoparticles and the matrix due to some aggregations, which restricted the composite performance. Thermal conductivity was also enhanced at TiO_2 NPs content of 0.2% due to crosslinking occurring between the polymer chains in the sample.

References

[1] S. Jothibasu et al., "Polyhedral oligomeric silsesquioxane (POSS) reinforced-unsaturated polyester hybrid nanocomposites: Thermal, thermomechanical and morphological properties", *J. Macromol. Sci. Pt. A Pure Appl. Chem.*, 55 (2018) 433-439.

[2] A.A. Athawale and J.A. Pandit, "Unsaturated Polyester Resins, Blends, Interpenetrating Polymer Networks, Composites, and Nanocomposites: State of the Art and New Challenges", in "Unsaturated Polyest. Resins", Elsevier, (2019) 1-42.

[3] H. Noor et al., "Dielectric and magnetic response of iron oxide nanoparticles embedded in unsaturated polyester resin", *Phys. B Cond. Matter.*, 602 (2021) 412554.

[4] A.S. Ismail, A.H. Mady and S.M. Tawfik, "Synthesis, Characterization and Biological Activity of Iron (III) Oxide and Titanium (IV) Oxide Nanoparticle Dispersed Polyester Resin Nanocomposites", *Arab. J. Sci. Eng.*, 45 (2020) 197-203.

[5] P.A. Jeemol, S. Mathew and C.P.R. Nair, "Maleimide end- capped polyether telechelics as novel toughening agents for unsaturated polyester resin", *J. Polym. Res.*, 27 (2020) 300.

[6] N. Ramadan et al., "Towards selection charts for epoxy resin, unsaturated polyester resin and their fibre-fabric composites with flame retardants", *Materials (Basel)*, 14 (2021) 1-44.

[7] A.N. Jassim and W.H. Jassim, "Preparation of Polyester/Micro Eggshell Fillers Composite as Natural Surface Coating", *Ibn Al-Haitham J. Pure Appl. Sci.*, 36(1) (2023) 88-99

[8] Y. Hai et al., "Ultrathin Beta-Nickel hydroxide nanosheets grown along multi-walled carbon nanotubes: A novel nanohybrid for enhancing flame retardancy and smoke toxicity suppression of unsaturated polyester resin", *J. Coll. Interface Sci.*, 509 (2018) 285–297.

[9] F. Chu et al., "Hierarchical core–shell TiO_2@LDH@$Ni(OH)_2$ architecture with regularly-oriented nanocatalyst shells: Towards improving the mechanical performance, flame retardancy and toxic smoke suppression of unsaturated polyester resin", *Chem. Eng. J.*, 405 (2021) 126650.

[10] F. Chu et al., "Hierarchical Structure: An effective Strategy to Enhance the Mechanical Performance and Fire Safety of Unsaturated Polyester Resin", *ACS Appl. Mater. Interfaces*, 11 (2019) 29436–29447.

[11] X. Chen et al., "Improved flame resistance properties of unsaturated polyester resin with TiO_2-MXOY solid superacid", *Chin. J. Chem. Eng.*, 28 (2020) 2474–2482.

[12] T.A. Taha and S.A. Saad, "Processing, thermal and dielectric investigations of polyester nanocomposites based on nano-$CoFe_2O_4$", *Mater. Chem. Phys.*, 255 (2020) 123574.

[13] N. Bing et al., "Unsaturated polyester resin supported form-stable phase change materials with enhanced thermal conductivity for solar energy storage and conversion", *Renew. Ener.*, 173 (2021) 926-933.

[14] H. Chen, X. Tian and J. Liu, "Unsaturated

 ISSN (print) 1813-2065, (online) 2309-1673 PRINTED IN IRAQ

Polyester Resin Nanocomposites Containing ZnO Modified with Oleic Acid Activated by N,N′-Carbonyldiimidazole", *Polymers (Basel)*, 10 (2018) 362.

[15] M.T. Rahman et al., "Fe_2O_3 nanoparticles dispersed unsaturated polyester resin based nanocomposites: effect of gamma radiation on mechanical properties", *Radiat. Eff. Defects Solids*, 174 (2019) 480–493.

[16] R. Baskaran, M. Sarojadevi and C.T. Vijayakumar, "Unsaturated polyester nanocomposites filled with nano alumina", *J. Mater. Sci.*, 46 (2011) 4864–4871.

[17] A. Koltsakidou et al., "Biobased Poly(ethylene furanoate) Polyester/TiO_2 Supported Nanocomposites as Effective Photocatalysts for Anti-inflammatory/Analgesic Drugs", *Molecules*, 24 (2019) 564.

[18] Z. Younus, L. Abbas and A. Hussein, "Improving The Properties of a Polyester-Based Composite Using Nanoparticle Fillers", *Eng. Technol. J.*, 39 (2021) 1705-1714.

[19] S.M. Sapuan et al., "Mechanical properties of longitudinal basalt/woven-glass-fiber-reinforced unsaturated polyester-resin hybrid composites", *Polymers (Basel)*, 12 (2020) 1-14.

[20] M.T. Rahman et al., "Study on the mechanical, electrical and optical properties of metal-oxide nanoparticles dispersed unsaturated polyester resin nanocomposites", *Results in Phys.*, 13 (2019) 102264.

[21] A.K. Saadon, A.M. Mhayyal and K.A. Jasim, "Effect of $BaTiO_3$ mixture on the structural, electrical properties and morphology for PET/$BaTiO_3$ composite", *AIP Conf. Proc.*, 2307, (2020).

[22] M. Blanco et al., "Thermal and Photocatalytic Performance of Unsaturated Polyester Resins Modified with TiO_2 Nanoparticles as Panel Bodies for Vehicles", *Polymers (Basel)*, 13 (2021) 2036.

[23] L.R.G. TRELOA, "Stress-strain data for vulcanised rubber under various types of deformation", *Trans. Faraday Soc.*, 40 (1944) 59-70.

[24] Sh. Mahdi, Q. Abd Saloom and D. Abd Alaziz, "Preparation of unsaturated polyester/nano ceramic composite and study electric, thermal and mechanical properties", *Iraqi J. Phys.*, 15(35) (2017) 188-201.

[25] Sh. Mahdi et al., "Effect of Pyrex Waste on the Electrical and Mechanical Properties of an Epoxy Resin", *J. Xi'an Univ. Architect. Technol.*, XII (2020) 303.

[26] R.B. Lutfi and W.H. Jassim, "Improvement of Dental Composite Resin Using Supra -Nano Chicken thigh Bone Fibers", *Ibn Al-Haitham J. Pure Appl. Sci.*, 36(2) (2023) 156-170.

[27] A.K. Saadon, A.H. Shaban and K.A. Jasim, "Effects of the Ferrits Addition on the Properties of Polyethylene Terephthalate", *Baghdad Sci. J.*, 19(1) (2022).

[28] K.A. Jassim et al., "Characteristics of (epoxy–bentonite doped) composite materials", *Energy Procedia*, 119 (2017) 670-679.

[29] M.M. Yahyaa and S.H. Aleabi, "Enhancing Some Mechanical Properties (Compression, Impact, Hardness, Young modulus) and Thermal Conductivity, Diffusion Coefficient of MicroEpoxy Composites", *Ibn Al-Haitham J. Pure Appl. Sci.*, 53(3)(2022) 32-43.

[30] R.N. Fadhil and Sh.H. Mahdi, "Effect of Pistachio Husks Powder Additive on Unsaturated Polyester Composites", *Ibn Al-Haitham J. Pure Appl. Sci.*, 36(2) (2023) 191-200.

[31] A.Q. Fadhel and W.H. Jassim, "Fabrication of Natural Gelcoats (Epoxy/Pumpkin Peels Fibers) Composites with High Mechanical and Thermal Properties", *Ibn Al-Haitham J. Pure Appl. Sci.*, 35(4) (2022) 21-36.

Appendix

Table (2) Average diameter for 0.1 wt.% TiO_2 NPs sample

Sample: 0.1 wt.% NTPs, Avg. Diameter: 97.37 nm								
<=10% Diameter: 70.00 nm			<=50% Diameter: 85.00 nm			<=90% Diameter: 125.00 nm		
Diameter (nm)<	Volume (%)	Cumulation (%)	Diameter (nm)<	Volume (%)	Cumulation (%)	Diameter (nm)<	Volume (%)	Cumulation (%)
45.00	0.53	0.53	80.00	8.99	25.93	115.00	8.47	76.19
50.00	0.53	1.06	85.00	4.76	30.69	120.00	6.35	82.54
55.00	0.53	1.59	90.00	10.58	41.27	125.00	5.82	88.36
60.00	1.06	2.65	95.00	6.35	47.62	130.00	5.29	93.65
65.00	3.17	5.82	100.00	4.76	52.38	135.00	4.23	97.88
70.00	6.35	12.17	105.00	5.82	58.20	140.00	2.12	100.00
75.00	4.76	16.93	110.00	9.52	67.72			

Table (3) Average diameter for 0.2 wt.% TiO_2 NPs sample

Sample: 0.2wt.% NTPs, Avg. Diameter: 90.33 nm								
<=10% Diameter: 65.00 nm			<=50% Diameter: 85.00 nm			<=90% Diameter: 115.00 nm		
Diameter (nm)<	Volume (%)	Cumulation (%)	Diameter (nm)<	Volume (%)	Cumulation (%)	Diameter (nm)<	Volume (%)	Cumulation (%)
55.00	2.23	2.23	80.00	10.41	32.71	105.00	6.32	74.35
60.00	1.12	3.35	85.00	9.29	42.01	110.00	7.43	81.78
65.00	4.09	7.43	90.00	9.67	51.67	115.00	5.95	87.73
70.00	6.69	14.13	95.00	6.69	58.36	120.00	8.55	96.28
75.00	8.18	22.30	100.00	9.67	68.03	125.00	3.72	100.00

Table (4) Average diameter for 0.3 wt.% TiO_2 NPs sample

Sample: 0.3 wt.% NTPs, Avg. Diameter: 101.41 nm								
<=10% Diameter: 70.00 nm			<=50% Diameter: 100.00 nm			<=90% Diameter: 120.00 nm		
Diameter (nm)<	Volume (%)	Cumulation (%)	Diameter (nm)<	Volume (%)	Cumulation (%)	Diameter (nm)<	Volume (%)	Cumulation (%)
70.00	2.49	2.49	100.00	18.26	49.38	130.00	13.69	95.02
80.00	11.62	14.11	110.00	14.94	64.32	140.00	4.98	100.00
90.00	17.01	31.12	120.00	17.01	81.33			

 ISSN (print) 1813-2065, (online) 2309-1673

IRAQI JOURNAL OF APPLIED PHYSICS
Vol. 19, No. 4A, October 2023, pp. 49-54

Hadeel D. Hamadalla
Falah H. Ali

Department of Physics,
College of Science,
University of Baghdad,
Baghdad, IRAQ

Preparation and Characterization of Metal-Doped Titanium Dioxide Nanostructures by Sol-Gel Method

In this study, sol-gel method was used to synthesize TiO_2 nanoparticles, then thin layers of undoped and doped TiO_2 were prepared using dip coating technique. These nanoparticles were doped with manganese with different concentrations in order to study the effect of doping on the characteristics of TiO_2 samples. The final products were characterized by x-ray diffraction (XRD), atomic force microscopy (AFM), and UV-visible spectrophotometry. The XRD patterns showed that the anatase phase is dominant in undoped TiO_2 and Mn-doped TiO_2 samples and broad peaks were identified indicating the formation of nanoparticles. This was confirmed by the AFM results, those also showed high aggregated grain size and high roughness. Finally, the absorption measurements showed that there is a decrease in the indirect energy gap from 3.20 to 2.4 eV when the content of manganese is increased, allowing for excellent absorption in the visible region, which is appropriate for photocatalyst applications.

Keywords: Titanium dioxide; Nanoparticles; Sol-gel; Dip coating
Received: 01 May 2023; **Revised:** 06 June 2023; **Accepted:** 13 June 2023

1. Introduction

The sol-gel method was invented in the 1960s and currently, it is one of the most common methods to prepare thin films and nanoparticles. This method has some advantages those not found in other conventional methods and techniques of thin film deposition and nanoparticles preparation. In this method, the formation of inorganic oxides can be prepared with gelatinous structures, which are converted into solid (amorphous) glassy structures at low temperatures [1-4].

The interest to this method to prepare TiO_2 thin films and nanostructures has been rapidly increased as a result of their applicability in many applications, such as photonics, photocatalysts, optoelectronics, photo-electrochemistry and electrochemistry, dye-sensitized solar cells (DSSC), air and water purification, and self-cleaning [5-8]. Titanium dioxide is a promising semiconducting material with high photochemical stability and low-cost production [9-11]. Heterogeneous semiconducting photocatalysts such as TiO_2 was intensively studied and employed for oxidative degradation of different organic and inorganic contaminants in air and water environments as a result of its high photocatalytic degradation capability, strong oxidation strength, biological and chemical stability, low cost, chemical corrosion stability and abundance [12-17]. Lately, there has been a considerable growing interest in the nanostructured TiO_2 thin films due to the fact that it has numerous potential applications, such as chemical sensors, solar cells and biomedical materials. TiO_2 is also the most widely utilized coating material due to its good transmission in the visible and near IR regions, good cohesion, high constancy towards the mechanical scratches, and high thermal stability [18-20]. The structural phases of TiO_2 generally include rutile, anatase and brookite [21] and the energy gap of anatase is 3.20eV and of rutile is 3.0 eV [22]. In order to reduce the energy band gap of TiO2 to respond to visible radiation, the crystalline (bulk) structure of TiO2 is doped and/or its surface structure is modified with metallic or nonmetallic dopants such as Ag, Ni, N, etc. [23-26].

In the present study, preparation of TiO_2 nanoparticles by sol-gel method is presented. These nanoparticles are doped with different concentrations of Mn (1, 3, 5, 7 and 9%). Thin films of the prepared samples are deposited on glass substrates using dip coating method. The structural and optical characteristics of these films are determined and analyzed.

2. Experimental part

Initially, a solution (labeled as A) has been prepared by mixing 3ml of the titanium tetra-isopropoxide (97% Aldrich) with 10.6ml of the anhydrous ethanol (99.80% Aldrich) whereas another solution (labeled as B) included 0.15ml distilled water, 0.3ml of the anhydrous ethanol, and 11.10ml of the acetic acid (99.70 % Aldrich). After that, the solution B has been added in a dropwise manner to

the solution A in order to obtain clear transparent solution. Few hours later, the solution gains milky consistency and after more hours, a gel has been obtained. The drying step has been carried out at 110°C for 24 hours to remove volatile solvents. After that, a xerogel has been obtained and then milled in agate mortar. Resulted powder has been calcined at a temperature of 500°C for 2 hours (5°C/min). For the purpose of improving synthesis process, the impact of different Pluronic P-123 (Aldrich) ratios have been studied. The following weight ratios have been studied, mass P123/TiO_2 = 0, 1, 3, 5, 7 and 9%.

3. Result and Discussion

The XRD patterns shown in Fig. (1) were utilized in order to analyze the crystalline structure of the prepared samples (undoped and Mn-doped TiO_2 thin films) after they had been heated to 500°C for two hours. These patterns revealed the formation of anatase phase of TiO_2 as eight peaks were identified and all attributed to this crystalline phase in accordance to the JCPDS card 21-1272 [27]. These diffraction peaks are corresponding to the crystal planes (101), (200), (004), (211), (105), (116), (204), (220) and (215). The peak observed at 25.28°, which belongs to the undoped TiO_2, was considered as a reference to introduce the effect of doping with Mn. For the TiO_2 samples doped with different concentrations of Mn (1, 3, 5, 7 and 9%), this peak was approximately constant in position (25.241°, 25.29°, 25.243°, 25.27° and 25.4°, respectively) and intensity, as shown in table (1). This result shows that the anatase phase of TiO_2 had actually developed [28]. Other peaks got weaker as the concentration of manganese was increased.

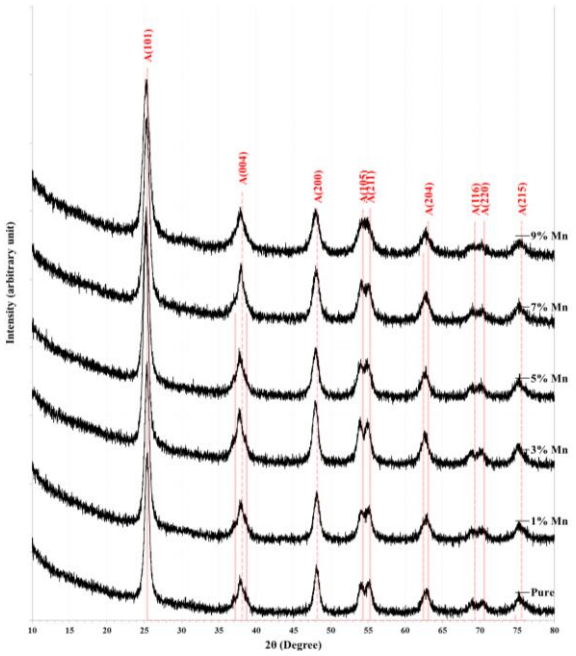

Fig. (1) XRD patterns of the undoped and Mn-doped TiO_2 thin film samples prepared in this work

The crystallite size (D) was determined from the Scherrer's equation as [27]

$$D = \frac{K\lambda}{\beta \cos\theta} \qquad (1)$$

where K represents a shaping factor equals to 0.9, λ represents the wavelength of the x-ray beam (nm), β is the full-width at half maximum intensity of diffracted peak (FWHM), and θ represents Bragg's diffraction angle

Table (1) Summary of structural parameters of the undoped and Mn-doped TiO_2 samples according to the XRD data

Mn (%)	2θ (deg.)	FWHM (deg.)	d_{hkl} (Å)	D (nm)	(hkl)	Phase
0	25.2886	0.3031	3.5190	26.9	(101)	Anatase TiO_2
1	25.2412	0.5628	3.5255	14.5	(101)	
2	37.8359	0.5196	2.3759	16.2	(004)	
3	25.2432	0.6927	3.5252	11.8	(101)	
5	25.2926	0.1732	3.5184	47.0	(101)	
7	25.2744	0.4330	3.5209	18.8	(101)	
9	25.4103	0.6494	3.5024	12.5	(101)	

The morphology of the undoped and Mn-doped TiO_2 thin films prepared in this work has been analyzed by the AFM results, as shown in Fig. (2), which shows the 2D and 3D images as well as the histogram of nanoparticle mean diameter distribution for undoped and Mn-doped TiO_2 nanoparticles at different concentrations of Mn dopants. Table (2) shows the average diameter of the prepared nanoparticles in addition to the values of average (R_a) roughness, root-mean-square ($R_{r.m.s.}$) roughness, and maximum height for all samples.

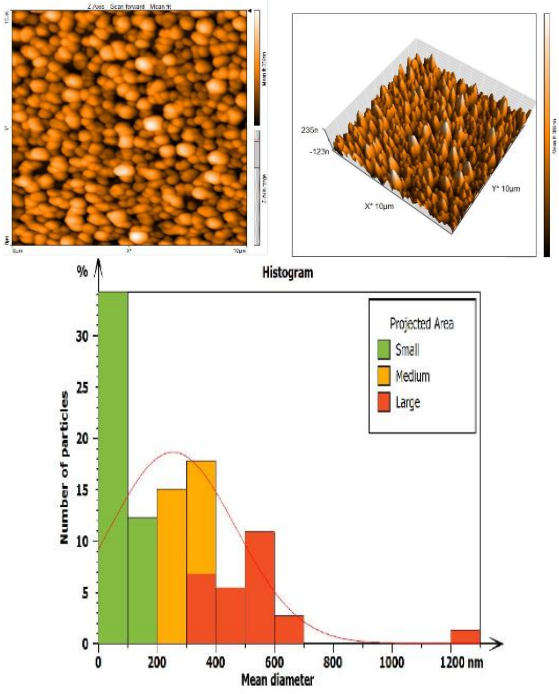

(a) undoped TiO_2 nanoparticles

  ISSN (print) 1813-2065, (online) 2309-1673

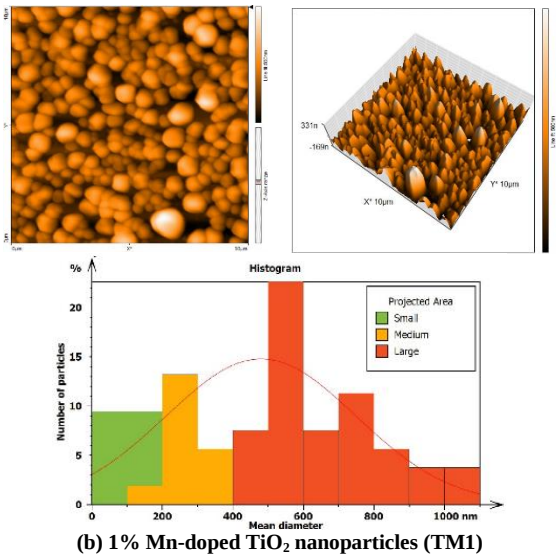

(b) 1% Mn-doped TiO_2 nanoparticles (TM1)

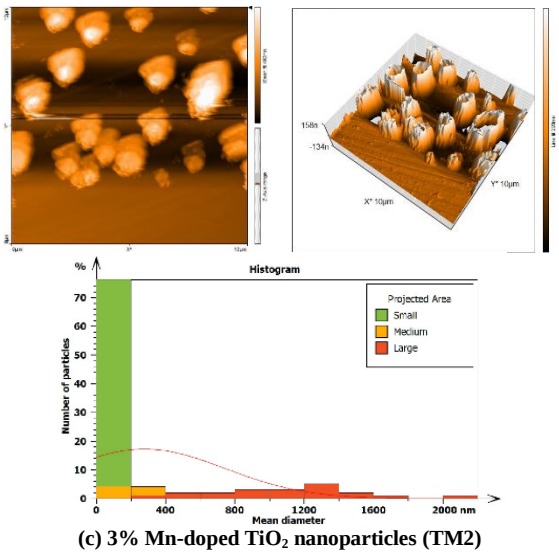

(c) 3% Mn-doped TiO_2 nanoparticles (TM2)

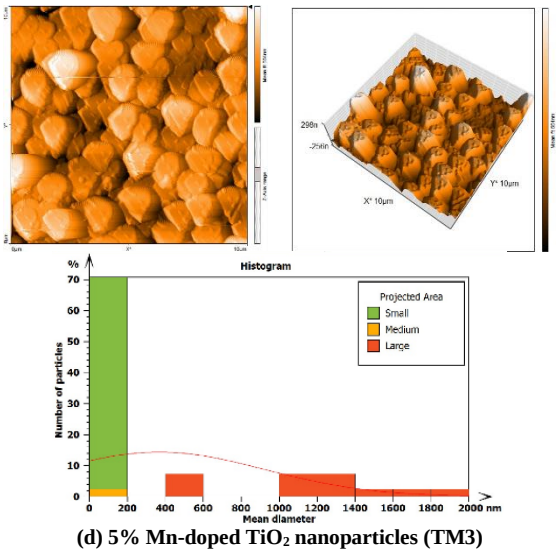

(d) 5% Mn-doped TiO_2 nanoparticles (TM3)

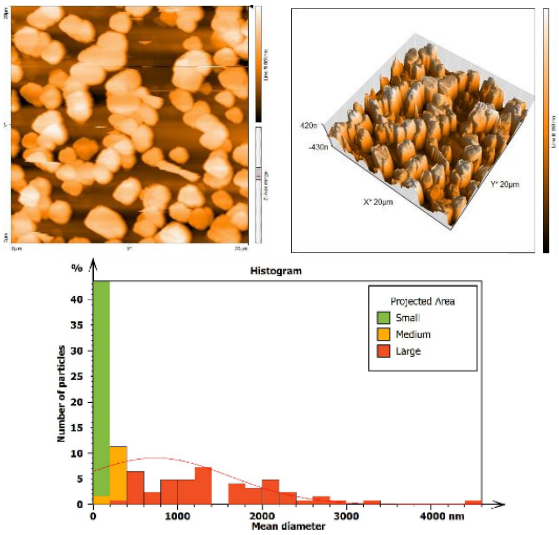

(e) 7% Mn-doped TiO_2 nanoparticles (TM4)

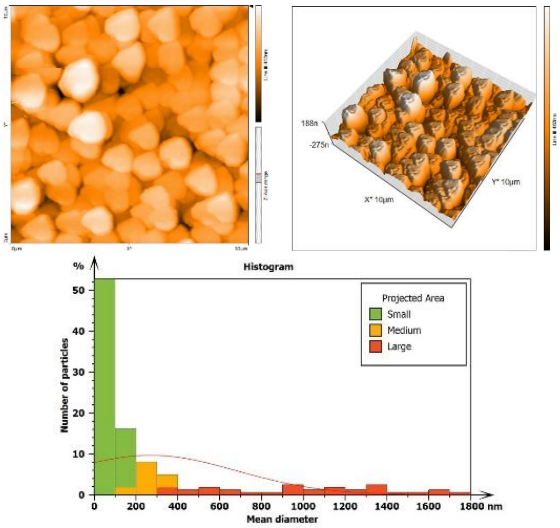

(f) 9% Mn-doped TiO_2 nanoparticles (TM5)

Fig. (2) 2D and 3D AFM images and histograms of undoped and Mn-doped TiO_2 nanoparticles prepared in this work

The surface roughness had varied within 49.38-58.57nm while the maximum values were shown by the sample doped with 7% Mn and the minimum values were shown by the undoped sample. These results are sufficiently necessary whne the prepared samples are used for practical applications those depend on the surface area, such as photocatalysts, photodetectors and solar cells. These results agree well to the results of Sharma et al. [29].

Table (2) Summary of AFM data of the undoped and Mn-doped TiO_2 samples

Sample	Mn (%)	Average Diameter (nm)	RMS Roughness (nm)	Average Roughness (nm)	Height (nm)
T	0	254.0	62.65	49.38	453.9
Tm1	1	479.5	79.26	63.14	489.8
Tm2	3	277.9	97.96	70.32	1542
Tm3	5	368.3	86.63	67.83	763.1
Tm4	7	735.3	208.2	188.7	1680
Tm5	9	268.0	73.2	58.57	520.5

Figure (3) shows the UV-visible absorption spectra the undoped and Mn-doped TiO_2 different concentrations of Mn. The undoped TiO_2 sample exhibited high absorption to the UV radiation shorter than 390nm, which is corresponding to energy band gap of about 3.2eV and the data in Fig. (4) and table (3) show the variation of energy band gap with the concentration of Mn dopants. It is clear that the energy band gap has increased with increasing the concentration of Mn dopants. Accordingly, the absorption edge had been shifted toward longer wavelengths (i.e., red shift). This can be attributed to the replacement of some Ti atoms with Mn atoms [30]. The absorption spectrum was reasonably raised in the visible and near infrared regions as the Mn doping concentration was 7%.

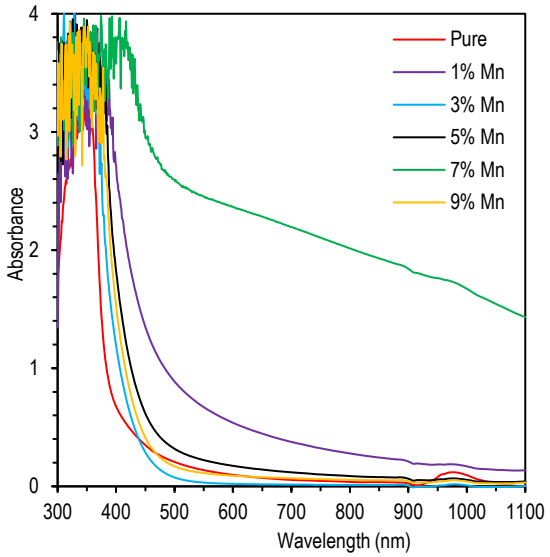

Fig. (3) Absorption spectra of the undoped and Mn-doped TiO_2 thin film samples prepared in this work

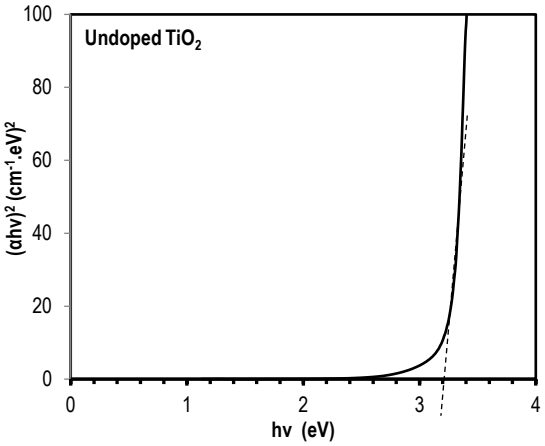

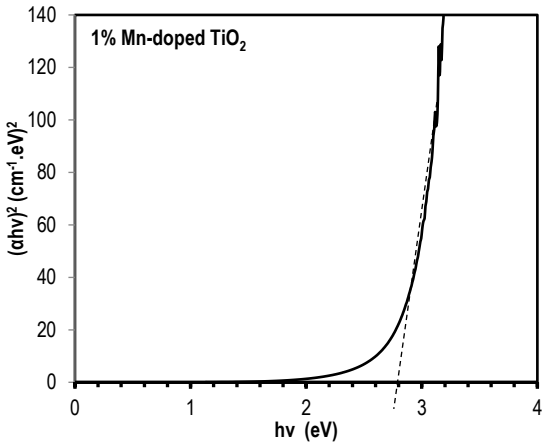

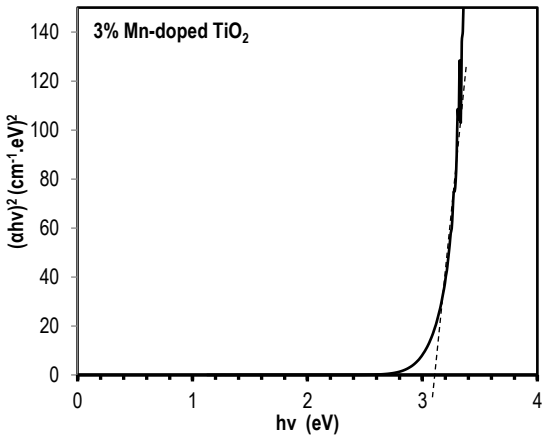

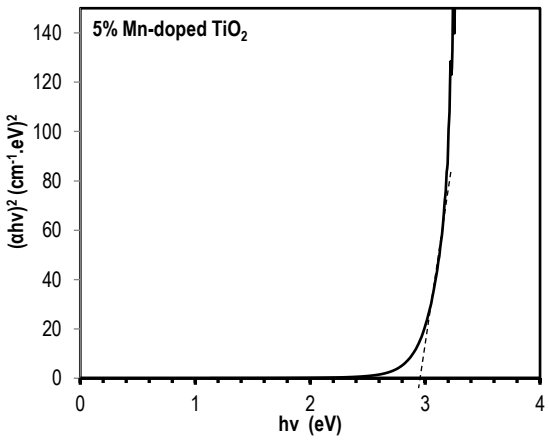

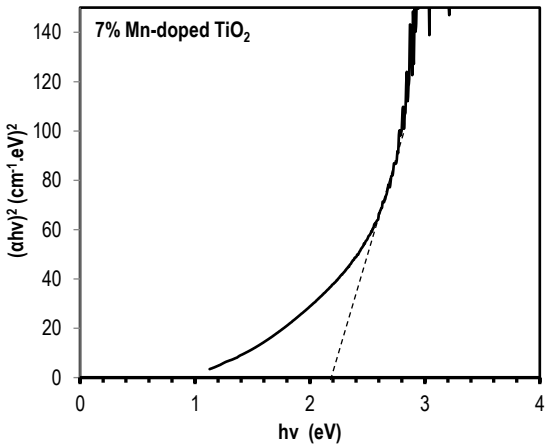

  ISSN (print) 1813-2065, (online) 2309-1673

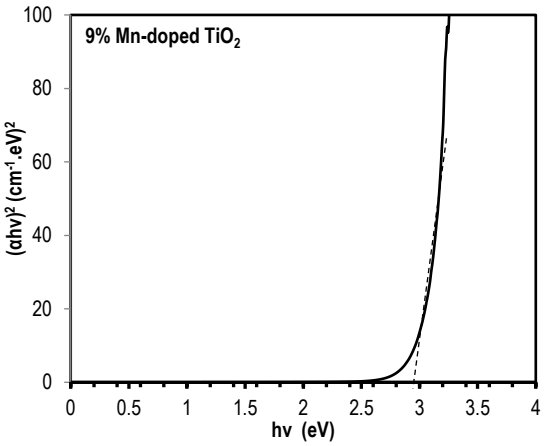

Fig. (4) Determination of energy band gap of the undoped and Mn-doped TiO_2 thin film samples prepared in this work

Table (3) Band gap values of the undoped and Mn-doped TiO_2 thin film samples prepared in this work

Sample	Mn doping (%)	E_g (eV)
T	0	3.2
Tm1	1	2.8
Tm2	3	3.1
Tm3	5	3.0
Tm4	7	2.4
Tm5	9	3.1

4. Conclusion

In concluding remarks, the sol-gel method can be considered as a good and effective method for the preparation of TiO_2 nanoparticles as well as for doping these nanoparticles with different concentrations of manganese. In both undoped and doped samples, the anatase phase of TiO_2 was dominant. The absorption edge of the doped samples was shifted to the visible region due to the narrowing of the energy band gap as the Mn dopants form energy states with the band gap of TiO_2. This is very important for some applications of TiO_2 nanostructures such as self-cleaning and dye-sensitized solar cells.

References

[1] M.N. Rahaman, **"Ceramic: Processing and Sintering"**, 2nd ed., CRC Press (2003).

[2] T.A. Al-Mashhadani and F.J. Al-Maliki, "Optimized Characteristics of Silver Nanoparticles Synthesized by Chemical Reduction and Embedded in Silica Xerogels", *Iraqi J. Appl. Phys.*, 18(3) (2022) 25-30.

[3] A.A. Salman and F.J. Al-Maliki, "Spectroscopic Study of Sol-gel Synthesized Silica Xerogel Embedded with Dysprosium Ions", *Iraqi J. Appl. Phys.*, 18(4) (2022) 21-25.

[4] T.A. Al-Mashhadani and F.J. Kadhim, "Photoluminescence properties of sliver-dysprosium co-doped silica obtained by sol–gel method", *J. Sol-Gel Sci. Technol.*, 106 (2023) 553-560.

[5] F.J. Al-Maliki, O.A. Hammadi and E.A Al-Oubidy, "Optimization of rutile/anatase ratio in titanium dioxide nanostructures prepared by DC magnetron sputtering technique", *Iraqi J. Sci.*, 60(Special issue) (2019) 91-98.

[6] G. Shemer and Y. Paz, "Photocatalytic Reduction of Cr (VI) by Titanium Dioxide Coupled to Functionalized CNTs: An Example of Counterproductive Charge Separation", *Int. J. Photoenergy*, 2011 (2011) 1-7.

[7] M. Montazer and S. Seifollahzadeh, "Enhanced Self-cleaning, Antibacterial and UV Protection Properties of Nano TiO_2 Treated Textile through Enzymatic Pretreatment", *Photochem. Photobiol.*, 87(4) (2011) 877-883.

[8] A. Nakaruk, D. Ragazzon and C.C. Sorrell, "Anatase–Rutile Transformation Through High-Temperature Annealing of Titania Films Produced by Ultrasonic Spray Pyrolysis", *Thin Solid Films*, 518(14) (2010) 3735-3742.

[9] F.H. Ali, W.A.A. Twej and A. Al-Kafaji, "Structural and Optical Properties of AL-doped TiO_2 Thin Films Prepared by Dip-Coating Method", *J. Spectro. Mol. Phys.*, 10(10) (2015) 91-96.

[10] E.A. Al-Oubidy and F.J. Al-Maliki, "Effect of Gas Mixing Ratio on Energy Band Gap of Mixed-Phase Titanium Dioxide Nanostructures Prepared by Reactive Magnetron Sputtering Technique", *Iraqi J. Appl. Phys.*, 14(4) (2018) 19-23.

[11] R.A.H. Hassan and F.T. Ibrahim, "Preparation and Characterization of Anatase Titanium Dioxide Nanostructures as Smart and Self-Cleaned Surfaces", *Iraqi J. Appl. Phys.*, 16(4) (2020) 13-18.

[12] A.L. Linsebigler, G. Lu Jr and J.T. Yates, "Photocatalysis on TiO_2 Surfaces: Principles, Mechanisms, and Selected Results", *Chem. Rev.*, 95(3) (1995) 735-758.

[13] A. Mills and S.K. Lee, "A web-based overview of semiconductor photochemistry-based current commercial applications", *J. Photochem. Photobiol. A: Chem.*, 152(1-3) (2002) 233-247.

[14] P. Zhong, W. Que, J. Chen and X. Hu, "Ruthenium oxide-coated carbon felt electrode: A highly active anode for microbial fuel cell applications", *J. Power Sourc.*, 210 (2012) 38-41.

[15] F.J. Al-Maliki and E.A. Al-Oubidy, "Effect of gas mixing ratio on structural characteristics of titanium dioxide nanostructures synthesized by DC reactive magnetron sputtering", *Physica B: Cond. Matter*, 555 (2019) 18-20

[16] Asal A. Moahmmed Ali, Mohammed A. Hameed, "Fabrication of Solid Random Gain Media in Visible Region from Rhodamine Dye Solutions Containing Highly-Pure Titanium Dioxide Nanoparticles", *Iraqi J. Appl. Phys.*, 18(1) (2022) 3-8

[17] F.J. Kadhim, O.A. Hammadi and N.H. Mutesher, "Photocatalytic activity of

TiO_2/SiO_2 nanocomposites synthesized by reactive magnetron sputtering technique", *J. Nanophot.*, 16(2) (2022) 026005.

[18] S.Y. Khalaf and F.H. Ali, "Hydrophilic Properties Study of Mn-TiO_2 Thin Films Deposited by Dipping Technique", *Iraqi J. Phys.*, 19(49) (2021) 62-74.

[19] E.A. Al-Oubidy and F.J. Al-Maliki, "Photocatalytic activity of anatase titanium dioxide nanostructures prepared by reactive magnetron sputtering technique", *Opt. Quantum Electron.*, 51(1-2) (2019) 23.

[20] Zahraa H. Zaidan, Qasim H. Mahmood and Oday A. Hammadi, "Using Banana Peels for Green Synthesis of Mixed-Phase Titanium Dioxide Nanopowders", *Iraqi J. Appl. Phys.*, 18(4) (2022) 27-30.

[21] S.J. Kadhem, "Optical properties for TiO_2/PMMA nanocomposite thin films prepared by plasma jet", *Iraqi J. Phys.*, 15(35) (2017) 24-28.

[22] A.H. Ataiwi and A.A. Abdul-Hamead, "Study the effect of adding TiO_2 nano-powder on some surface properties of TiO_2 thin film prepared on stainless steel substrate", *Iraqi J. Phys.*, 10(18) (2012) 29-34.

[23] S.N.R. Inturi, T. Boningari, M. Suidan and M. Smirniotis, "TiO_2 Modification with Transition Metallic Species (Cr, Co, Ni, and Cu) for Photocatalytic Abatement of Acetic Acid in Liquid Phase and Propene in Gas Phase", *P. G*, 144 (2014) 333-342.

[24] O.A. Hammadi, F.J. Kadhim and E.A. Al-Oubidy, "Photocatalytic Activity of Nitrogen-Doped Titanium Dioxide Nanostructures Synthesized by DC Reactive Magnetron Sputtering Technique", *Nonl. Opt. Quantum Opt.*, 51(1-2) (2019) 67-78.

[25] R.A.H. Hassan and F.T. Ibrahim, "Preparation and Characterization of Ni-doped TiO_2 Nanostructures for Surface Cleaning Applications", *Iraqi J. Appl. Phys.*, 17(1) (2021) 3-8.

[26] Noor Alhuda H. Hashim, Firas J. Kadhim and Zinah S. Abdulsattar, "Characterization of Electrochromism and Photoelectrochromism of N-Doped TiO_2 and Co_3O_4 Thin Films Prepared by DC Reactive Magnetron Sputtering: Comparative Study", *Iraqi J. Appl. Phys.*, 19(1) (2023) 5-12.

[27] M. Cohen, **"Elements of X-Ray Diffraction"**, 2nd ed., Addison-Wesley Pub. Co. (1978).

[28] H. Tang et al., "Urbach tail of anatase TiO_2", *Phys. Rev. B*, 52(11) (1995) 7771-7774.

[29] S. Sharma et al., "Room temperature ferromagnetism in Mn doped TiO_2 thin films: electronic structure and Raman investigations", *J. Appl. Phys.*, 109(8) (2011) 083905.

[30] Q.R. Deng et al., "Mn-doped TiO_2 nanopowders with remarkable visible light photocatalytic activity", *Mater. Lett.*, 65(13) (2011) 2051-2054.

  ISSN (print) 1813-2065, (online) 2309-1673

IRAQI JOURNAL OF APPLIED PHYSICS
Vol. 19, No. 4A, October 2023, pp. 55-60

Ali K. Shanoof
Nabeel A. Areebi

Department of Physics, College of Education, University of Al-Qadisiyah, Al-Diwaniyah, IRAQ

Bandwidth Enhancement of Cylindrical Circular Microstrip Antenna Using Slots Technique

This paper proposes an improved performance for the circular conformal microstrip antennas. Narrow bandwidth is the main disadvantage of these antennas. The proposed antenna is a circular patch constructed on a cylindrical surface called a "Cylindrical Circular Microstrip Antenna" (CCMA) at the resonant frequency of 2.4 GHz which is designed via CST program with aid Finite Difference Time Domain FDTD method. The slot techniques are used to improve the antenna's performance including bandwidth. Two ring slots and two square slots are drilled in all the patch and ground plane, respectively. The best result which was obtained for the bandwidth is 43% compare with 1.6% without slots. Furthermore, a fabricated prototype provides a good agreement between the measured and simulated results. The measured bandwidth is 30.7% compared with simulated 43%.

Keywords: Bandwidth; Cylindrical Circular Microstrip Antenna; FDTD Method; Slots Technique
Received: 16 May 2023; **Revised:** 5 June 2023; **Accepted:** 12 June 2023

1. introduction

An antenna is a conductor of electricity or a group of conductors used in electromagnetic wave transmission and reception systems. A microstrip antenna consists of two small superconductors sandwiched between dielectric substrates. Microstrip antennas come in two varieties: planar and non-planar, or conformal. There are several uses for conformal microstrip antennas with strong directivity and cheap cost [1]. To create the simulation model of the FDTD approach in the time domain, Maxwell curl equations are solved [2]. A conformal antenna, as is well known, is a kind of antenna that may be utilized with any curved surface, regardless of its shape, by simply altering the geometry of the ground plane for the antenna. Furthermore, the patch can be applied to the base without causing any extra downsides or altering its radiation properties in an unacceptable way [3]. From the antOne type of conformal antenna is singularly curved, like a cylindrical antenna, depending on how many curves the geometry has, while the other na ground plane is doubly curved, like a spherical antenna. Surface wave radiation increases with substrate thickness and dielectric constant, therefore it can be reduced using a variety of techniques, such like restricting substrate size or including a modal photonic band gap [4]. As is well known, a wide bandwidth antenna with a variety of shapes, including a circle, an ellipse, and a triangle, has been reported [5]. Patch antennas have a variety of benefits, including low profile, light weight, compact volume, and compatibility with MMICs and MICs [6]. The main barrier to widespread implementation of the microstrip antenna is its limited bandwidth [7].

In recent years, low cost, light weight, low profile antennas that can sustain great performance over a wide spectrum of frequencies have been popular in commercial and government communication systems.

The design of tiny strip (patch) antennas has received a great deal of attention in this technological trend. The use of a microstrip antenna has all the benefits that come with printed circuit technology. Basic microstrip structures also have other problems such loss, half-plane radiation, low power handling capacity, and gain limitations. The benefits of tiny strip antennas outweigh the drawbacks in many practical systems [8].

There are several methods to improve the bandwidth including double of the dielectric layer, make slots within patch, using a material with a low dielectric constant, partial cutting with patch or ground and slotted work [9].

Now, in proposed design, the antenna's ground plane and patch have been modified. Ground plane and the antenna have a square slots and two ring slots respectively. Significant increasing in bandwidth will be achieved.

2. Finite Difference Time Domain (FDTD) Method

Kane Yee 1966 presented a numerical method for solving problems related to Maxwell's curl equations [10]. Yee assumed that a point in space is a cell of size ΔxyΔzΔ which illustrates the distribution of the elements that make up magnetic fields and electric field and that the space will be a network of cells [11,12] as shown in Fig. (1). Any component of the electromagnetic field can be represented by a function u that depends on space and time, and its value is calculated within the Yee cell. Value of u is as follows [13,14]

$$U(\Delta x, \Delta y, \Delta z, n\Delta t) = u^n(i, j, k) \quad (1)$$

where i , j and k are integral

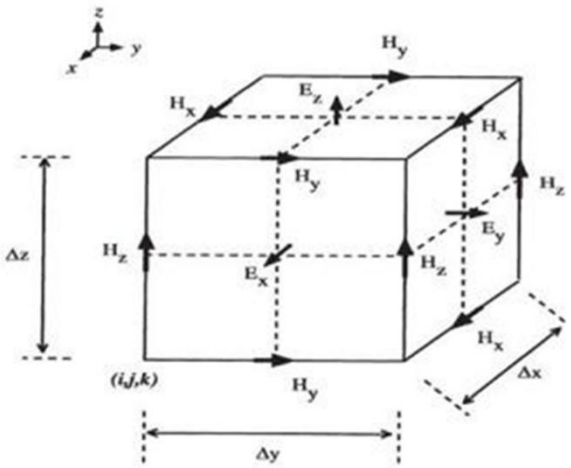

Fig. (1) Yee's cell in 3D

The system is excited by an electrical pulse, which is mathematically represented by a Gaussian function in the time domain called a Gauss pulse [15,16]

$$p(t) = e^{-(\frac{t-t_0}{\tau})^2} \quad (2)$$

where τ is called the decay constant and its value is influenced by the frequency range used, t_0 represents the relaxation time and t is the simulated time

For programming, the perfectly matched (PML) method was used to handle infinite space [17,18]. The propagation of the wave in space leads to the diminishing of the values of its compounds and becomes a very small value compared to the values of the compounds at their maximum values. Thus, after N calculations, Fourier transformations can be used to find the impedance value $Z_{in} = R + ix$ [19,20].

The matched condition can be ex-pressed by the formula:

$$Z_{in(\omega)} = Z_S^* = \left(\frac{\int_{-\infty}^{\infty} v(t)e^{-i\omega t}dt}{\int_{-\infty}^{\infty} I(T)e^{-i\omega t}dt}\right)$$

$$= \frac{\sum_n^N 0(n\Delta t)e^{-i\omega tn\Delta t}\Delta t}{\sum_{n=0}^{N-1} I\left((n+\frac{1}{2})\Delta t\right)e^{-i\omega\left(n+\frac{1}{2}\right)\Delta t}\Delta t} \quad (3)$$

where $Z_{in}$is the input impedance, R, the input resistance, x the total reluctance, ω , the frequency of the angular for the electromagnetic wave and $\Delta(t)$, size of the time step, $v(t)$ is the voltage at the feeding point that is calculated to be in the time domain. From Faraday's law [21] (*see appendix*, Eq. 4).

I(t) is the current at the feeding point that is measured in the time domain, and Ampere's law is determined as shown in appendix (Eq. 5).

The loss factor S_{11}in the frequency domain is calculated as follows [22]

$$S_{11} = \left(\frac{\int_{-\infty}^{\infty} V(t)e^{-i\omega t}dt}{\int_{-\infty}^{\infty} p(t)e^{-i\omega t}dt}\right) = \frac{\sum_{n=0}^{N} V(n\Delta t)e^{-i\omega tn\Delta t}\Delta t}{\sum_{n=0}^{N} p(n\Delta t)e^{-i\omega tn\Delta t}} \quad (6)$$

3. Cylindrical Circular Microstrip Antenna Design

The proposed arrangement for the antenna is a circular patch constructed on a cylindrical surface called a "Cylindrical Circular Microstrip Antenna" (CCMA) which is simulated vertically through CST Studio Suite 2021 program as shown in Fig. (2). The antenna design consists of a substrate with a single layer of 1.5 mm and dielectric thickness constant 4.4. A diameter of cylindrical a=8.5 cm and radius of circular patch $a_p = 17mm$ at the resonant frequency 2.4GHz.

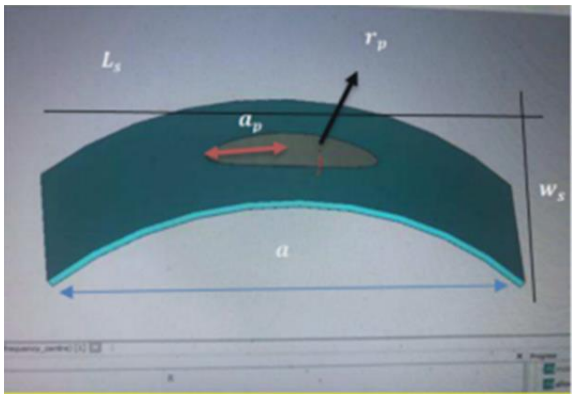

Fig. (2) The proposed CCMA

The coaxial probe approach used for feeding the CCMA. The feeding point is located at r_p=5.13mm. The radius and patch's resonance frequency can be computed by using the formula below [23]

$$f_r = \frac{1.84118C}{2\pi a_e\sqrt{\varepsilon_e}} \quad (7)$$

where $a_e$is the effective radius, C is the speed of light, and ε_e is the effective dielectric constant.

The average current can be determined by

$$I_{feed}^n = \sqrt{I_{feed}^{n-\frac{1}{2}} I_{feed}^{n+\frac{1}{2}}}$$

where *n* is time step iteration

4. Results and Discussion

4.1. The Simulated Results

The input impedance must be matched at 50 Ω. Input impedance Z_{in} is one of the important parameters. Simulation results of the imaginary (reactance) and real (resistance) In Fig. (3), input impedance is displayed.. The resonant frequency occurs when the reactance value is zero $f_r = 2.42GHz$ and the input, impedance Zin = 55Ω.

 ISSN (print) 1813-2065, (online) 2309-1673

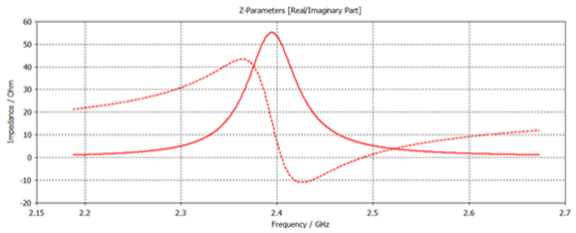

Fig. (3) The input impedance calculated by CST (— Z1,1 (Re), ---- Z1,1 (Im))

Value of the return loss -50dB shown in Fig. (4). The range of frequencies at the two opposing corners of at -10dB's return loss is used to compute the bandwidth. Bandwidth is calculated from the following equation [24] and the percentage of bandwidth for the proposed antenna is 1.6%

$$BW = 200 \times \frac{f_H - F_L}{f_H - f_L}\% \quad (8)$$

where f_H is the upper frequency and f_L is the lower frequency.

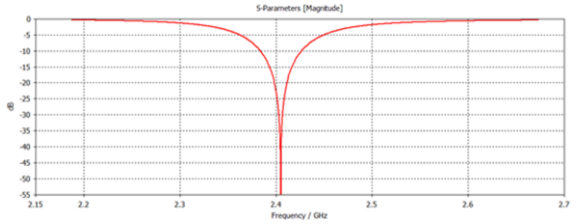

Fig. (4) Return loss calculated by CST

Figure (5) displays the E-plane and H-plane's respective polar electric field distributions. Radiation pattern represents the normalized values for the field patterns. The pattern of radiation is depicted being broadside and devoid of side lobes. Radiation Pattern, which is one of the basic characteristics of the antenna, which shows the direction of energy concentration or the intensity of radiation, whether it is in a specific direction or in all directions in space or physical media. Based on the radiation pattern, it is possible to determine how the direction of the antenna is in the case of transmission or reception.

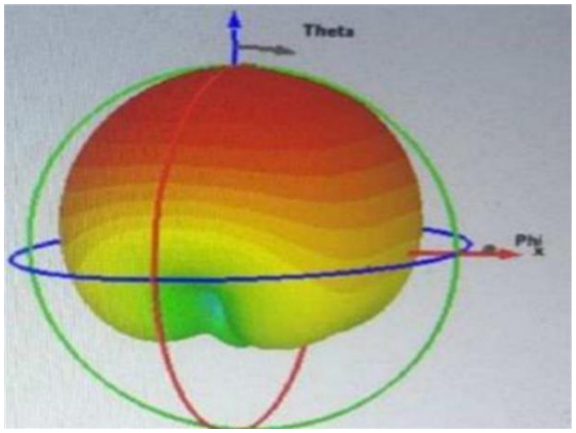

Fig. (5) Radiation pattern of the CCMA

4.1.1. The Measured Results

The CCMA was manufactured to operate at frequency (2.4GHz) with the same dimensions of the designed CCMA using CST program. Patch and ground plane are made of copper, and the dielectric substrate is (FR-4) with dielectric constant of ε_r= 4..4 and thickness h = 1.5 mm. Coaxial feed is used to fed CCMA at $r_p = 5.13mm$ from the patch's center, as shown in Fig. (6). Using Vector Network Analyzer, return loss is measured. Figure (7) shows the comparison between the measured and simulated results of the two manufactured and designed CCMAs. The measured bandwidth is 1.5% compared with simulated 1.6%. The measured resonant frequency is 2.375 GHz compared with simulated 2.42 GHz and this difference occurs because of the dimensions of fabricated prototype those may be sufficiently inaccurate. Resonant frequency can be affected by the increase or decrease in the radius of patch.

Fig. (6) Fabricated prototype of CCMA

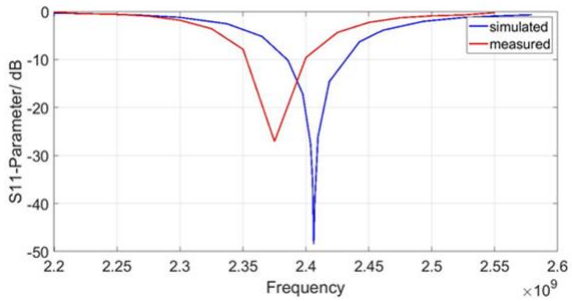

Fig. (7) Comparison between measured and simulated results of CCMA without slot

4.2. Design of CCMA with Slots.

In order to increase the bandwidth of CCMA, two ring slots and two square slots have been designed in all the patch and ground plane, respectively, as shown in Fig. (8). The dimensions of proposed antenna and slots are summarized in Table (1). The obtained results of CCMA is plotted in Fig. (9). From the simulated return loss, bandwidth is 43% with resonant frequency of 4.4 GHz, which can be affected

by the dimensions of patch as it increases with decreasing the size of patch. Figure (10) shows radiation pattern which depicts that the radiation power increases as the slots introduces.

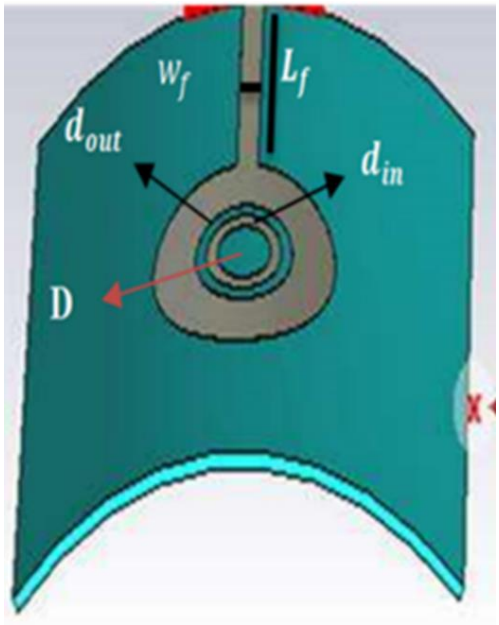

(a)

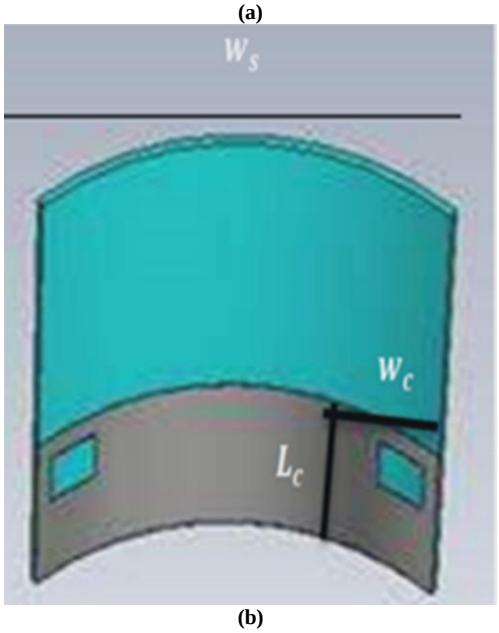

(b)

Fig. (8) The proposed CCMA with slots. (a): Top View. (b): Bottom View

Table (1) Parameters of the Proposed Antennas

Parameter	Value (mm)	Parameter	Value (mm)
Wsub	78.5	Lsub	78.5
Wc	10	L_c	10
Wf	4	L_f	32.62
d_{in}	14	d_{out}	18
a_p	17	a	8.5 cm
r_p	5.13	D	10

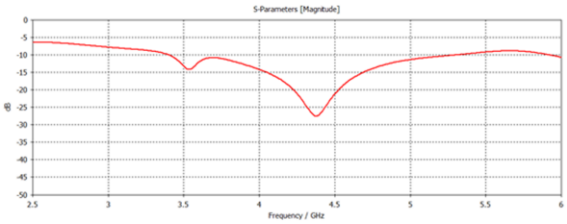

Fig. (9) Return loss with slot by CST

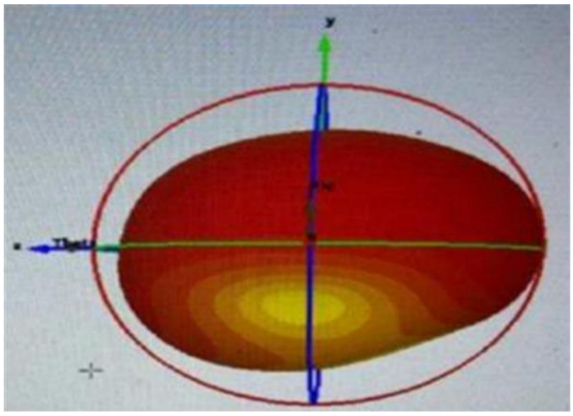

Fig. (10) Radiation pattern with slots

4.2.1. The Measured Results

Again, CCMA with slots was manufactured as shown in Fig. (11). Using Vector Network Analyzer, return loss is measured. The measured bandwidth is 30.7% compared with simulated 43%. The measured resonant frequency is 4 GHz as compared with simulated 4.4 GHz. This difference can be a result of the size of proposed prototype that may be inaccurately fabricated.

Fig. (11) Fabricated prototype of CCMA with slots

4.2.2. Comparison between measured and simulated results

Figure (12) shows a comparison between the measured results and the simulated results .A small difference is due to the result that the simulation is

 ISSN (print) 1813-2065, (online) 2309-1673

approximate, and also when manufacturing, slight parts of patch or the substrate material are damaged. In addition, the laboratory conditions are somewhat unsuitable, which led to a mismatch between the measured and simulated results.

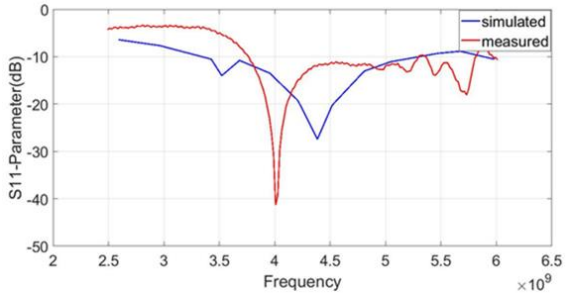

Fig. (12) Comparison between measured and simulated results with slots

5. Conclusion

In conclusion, the FDTD approach used in the CST software, is used to design and simulate CCMA. Values of, return loss, the input impedance and the pattern of radiation is calculated. The slots technique has been essential in improving CCMA's operation in UWB applications. With frequency range 3.37 to 5.24 GHz and 43% of impedance bandwidth. Hence, this study confirmed that using slots technique (in all antenna's ground plane and patch) increased the value of the bandwidth and improved both the radiation pattern and return loss coefficients.

References

[1] N. Areebi and J.N. Jabir, "Bandwidth Improvement of a Cone-Inverted Cylindrical and Cross Hybrids Dielectric Resonator Antennas," *Iraqi J. Phys.*, 21(1) (2023) 77–87.

[2] L. C. Godara, **"Handbook of Antennas in Wireless Communications"**, CRC Press (2018).

[3] L. Josefsson and P. Persson, **"Conformal Array Antenna Theory and Design"**, John-Wiley & Sons (2006).

[4] N.A. Areebi, Z.A. Ahmed and M.M. Aubais, "New Design of Cylindrical Rectangular Microstrip Antenna (CRMA) By Using The Slots Technique," *J. Kufa Phys.*, 12 (1) (2020) 1-8.

[5] M. Scalora et al., "Transparent, metallo-dielectric, one-dimensional, photonic band-gap structures," *J. Appl. Phys.*, 83(5) (1998) 2377–2383.

[6] R. Garg, P. Bhartia, I.J. Bahl and A. Ittipiboon, **"Microstrip Antenna Design Handbook"**, Artech house (2001).

[7] T.A. Denidni and M.A. Habib, "Broadband printed CPW-fed circular slot antenna," *Electron. Lett.*, 42(3) (2006) 135.

[8] M. Labiod, Z. Mahdjoub and M. Debab, "Frequency reconfigurable circular microstrip patch antenna with slots for cognitive radio," *Telecommun. Comput. Electron. Control.*, 20(4) (2022) 740–752.

[9] D.S. Katz et al., "FDTD analysis of electromagnetic wave radiation from systems containing horn antennas", *IEEE Trans. Antennas Propag.*, 39(8) (1991)1203-1212.

[10] A. Taflove, "Application of the finite-difference time-domain method to sinusoidal steady-state electromagnetic-penetration problems," *IEEE Trans. Electromagn. Compat.*, 11(3) (1980) 191–202.

[11] Z.N. Chen and M.Y.W. Chia, "Broadband Planar Antennas: Design and Applications", John-Wiley & Sons (2006).

[12] D.S. Katz, E.T. Thiele and A. Taflove, "Validation and extension to three dimensions of the Berenger PML absorbing boundary condition for FD-TD meshes," *IEEE Microw. Guid. Wave Lett.*, 4(8) (1994) 268–270.

[13] S. C. Hagness, S. T. Ho and A. Taflove, "Finite-difference time-domain (FDTD) computational electrodynamics simulations of microlaser cavities in one and two spatial dimensions," *Comput. Electromag. Appl.*, (1997) (229–251).

[14] V. Demir and A.Z. Elsherbeni, "Compute unified device architecture (CUDA) based finite-difference time-domain (FDTD) implementation," *Appl. Comput. Electromagn. Soc. J.*, (2010) 303–314.

[15] K.K. Lehmann and D. Romanini, "The superposition principle and cavity ring down spectroscopy", *J. Chem. Phys.*, 105(23) (1996) 10263-10277.

[16] E.K. Miller and J.A. Landt, "Direct time-domain techniques for transient radiation and scattering from wires", *Proc. IEEE*, 68(11) (1980) 1396-1423.

[17] D.M. Sheen, "Numerical modeling of microstrip circuits and antennas." Massachusetts Institute of Technology (1998).

[18] R. Remski, "Analysis of photonic bandgap surfaces using Ansoft HFSS," *Microw. J. Euroglobal Ed.*, 43(9) (2000) 190–199.

[19] H.S. Gally, Z.A. Ahmed and A.H. Abood, "Mutual Coupling Reduction In Microstrip Antenna Array Using Ebg," *J. Basrah Res.*, 44(1) (2018) 1-8.

[20] U.S. Inan and R.A. Marshall, **"Numerical Electromagnetics: The FDTD Method"**, Cambridge University Press (2011).

[21] D. Rano, M.A. Chaudhary and M.S. Hashmi, "A new model to determine effective permittivity and resonant frequency of patch antenna covered with multiple dielectric layers," *IEEE Access*, 8(2020) 34418–34430.

[22] E.S. Al-Sayed and N.A. Areebi, "Bandwidth enhancement of cylindrical triangular

microstrip antenna using a stacked technique," *Iranian J. Phys. Res.*, 22(3) (2022) 167-173.

[23] W.Y. Tam, A.K.Y. Lai and K.M. Luk, "Microstripline-and stripline-fed aperture-coupled cylindrical rectangular microstrip antennas," *IEE Proc. Microwaves, Antennas Propag.*, 145(3) (1998) 257–261.

[24] K.-L. Wong, **"Design of nonplanar microstrip antennas and transmission lines"**, John-Wiley & Sons (1999).

APPENDIX

$$V_{feed}^{n} = -\frac{1}{9}\left(\sum_{i=i_{feed-1}}^{i=i_{feed+1}}\sum_{j=j_{feed-1}}^{j=j_{feed+1}}\sum_{k=d}^{k=u} E_{z\left(i_{feed},j_{feed},k\right)}^{n}\Delta z\right) \quad (4)$$

$$I_{feed}^{n+\frac{1}{2}} = \frac{1}{u-d}\left(\sum_{k=d}^{k=u}\left(\sum_{i=i_{feed-1}}^{i=i_{feed+1}} H_{x}^{n+\frac{1}{2}}(i,j-1,k)\Delta x + \sum_{j=j_{feed}}^{j=j_{feed+1}} H_{y}^{n+\frac{1}{2}}(i-1,j,k)\,\Delta y - \sum_{i=i_{feed-1}}^{j=i_{feed+1}} H_{x}^{n+\frac{1}{2}}(i,j+1,k)\Delta x - \sum_{j=j_{feed-1}}^{j=j_{feed+1}} H_{y}^{n+\frac{1}{2}}(i+1,)\Delta y\right)\right) \quad (5)$$

 ISSN (print) 1813-2065, (online) 2309-1673

IRAQI JOURNAL OF APPLIED PHYSICS
Vol. 19, No. 4A, October 2023, pp. 61-66

Innovative Method to Prepare Highly Adhesive CuO Thin Films on FTO Substrates for Optoelectronic Applications

Mofeed A. Jaleel
Mustafa A. Hassan
Khaleel I. Hassoon

Department of Applied Sciences, University of Technology, Baghdad 10066, IRAQ

In this work, low-cost homemade hydrothermal autoclave is used to prepare CuO thin films on FTO substrates. The tape method for rating adhesion showed good adhesion quality between CuO films and FTO substrates. The XRD analysis exhibited polycrystalline structure with predominant monoclinic system. The peaks were at 35.72°, 38.83°, and 48.86° against average crystallite size 34, 52, and 28 nm, respectively. FESEM images revealed that the films were composed of nanosheets and microsheets varied in length and width (up to several micrometers) and thickness from several hundred nanometers to several micrometers. The CuO micro and nanosheets provide high (area to volume) ratio which is favorable to offer high contact area between CuO as a counter electrode and the electrolyte in dye sensitized photodetectors and solar cells.

Keywords: Copper oxide; Thin films; Hydrothermal deposition; Optoelectronics
Received: 24 June 2023; **Revised:** 23 July 2023; **Accepted:** 30 July 2023

1. Introduction

Thin films are layers of atoms or molecules of any material deposited on various substrates to achieve new surface properties which make the material with better sensitivity for ambient changes like light intensity or temperature [1]. In recent years, a great interest has emerged by researchers in copper oxide thin films due to their unique characteristics represented by chemical stability, high absorption coefficient, abundance, nontoxicity and low cost [2, 3]. Copper oxide almost exists in two stable phases: CuO (Cupric oxide) and Cu_2O (Cuprous oxide). The cupric oxide phase has a monoclinic crystal system with an optical bandgap (1.3-2.2 eV), while Cuprous oxide phase has a cubic crystal system with an optical bandgap (2-2.6eV) [2,4]. The semiconducting properties of CuO stem from Cu vacancies in the crystalline structure [5]. Cupric oxide is a p-type semiconductor, but it could be n-type by doping [6] or by annealing [7]. The electrical conductivity of copper oxide thin films varies in a wide range depending on the method of preparation and the type of impurity as well as the nature of crystallization, and this made it possible to develop new applications for CuO thin films [3,6,7].

Copper oxide is not only used in detectors [8,9] and solar cells [10, 11], but also it is employed in other applications such as gas sensors [12], humidity sensors [13] and lithium batteries [14,15].

One of the advantages of copper oxide films is the possibility of preparing them by several methods, some of these methods are inexpensive and simple, such as spraying pyrolysis [1,7] and chemical bath deposition [3], they could be prepared by a more sophisticated methods such as diode sputtering [16].

In 2013, Gund et al [17] fabricated copper oxide thin films with nanosheets microstructures. The thin films directly grown onto a stainless-steel substrate to be used as a capable electrode material for super-capacitors.

In 2015, Ghotabi et al [18] prepared Cupric thin films by a hydrothermal method using copper hydroxide nitrate as a precursor. Thickness, crystallite size and morphology were modified by changing the time of hydrothermal treatment. They concluded that the contact angle and hence the wettability of thin films can be tailored via changing the hydrothermal time.

In 2017, Teli et al [19] synthesized CuO electrodes by rapid hydrothermal technique. Trioctylphosphine oxide (TOPO) was used as a capping agent to study its effect on structural, morphological and electrochemical properties for different concentration of Cu precursor. They concluded that the specific capacitance can be modified by optimizing the concentrations of TOPO and Cu precursor.

In 2020, Ozga et al [20] used a modified hydrothermal method to prepare CuO thin films with nanocrystal size (7-12nm). This preparation technique is shown to be fast, simple and the reaction solutions are only three, i.e., deionized H_2O, copper (II) acetate and NaOH as a pH regulator.

In 2022, Mroczyński etal [21] deposited CuO thin films of thickness (100 nm) on highly doped n-type silicon substrates using Hydrothermal method for the application in switching memory devices.

In the field of solar cells, there is much new research that uses an alternative to the platinum electrode in dye-synthesized solar cells [5,22-24], where the metal oxides or metal sulfides have been used. However, attempts to prepare CuO thin films on FTO are quite rare. In this research, copper oxide nanosheets have been synthesized on FTO substrates and used as a counter electrode for dye sensitized photodetector. CuO thin films with nanosheets structures are appropriate for optoelectronic devices for their high absorption coefficient in the visible light, as well as its preferred high surface to volume ratio which provides with large contact area between the CuO film and the electrolyte solution.

2. Experimental part

Porous copper oxide (CuO) thin films were prepared using the hydrothermal method. This method was also used to prepare copper oxide nanoparticles using more complex compounds than what was used in this study [21,25]. All chemicals were used as received without further purification. Firstly, a solution of copper chloride (0.1 M) was prepared. Then ammonia (0.22M) was added until the pH became 12. FTO (fluorine tin oxide) slides from GreatCell Energy were used as substrates to deposit copper oxide films. The substrates are previously cleaned by immersing them in pure ethanol and placed in an ultrasonic cleaning instrument. After that, the slides are placed on a special homemade Teflon rack and autoclave (Fig. 1).

The FTO glass slides are placed so that the conductive surface becomes upward since it was noted experimentally that CuO films could not be deposited onto uncoated glass slides. After the introduction of the slides and the solution into the Teflon container, the autoclave has been closed tightly. Then the autoclave was placed in an oven and heated to a temperature of 200 °C for two hours. Later, the autoclave is taken out of the oven and cooled down to room temperature. After that, the samples are washed with pure distilled water and placed inside a Pyrex Petri dish. The annealing treatment was implemented inside an oven for two hours at temperature 400 °C. After that, the samples were left until they cooled down to room temperature and then they were taken out from the oven. To evaluate adhesion of a CuO thin film to FTO substrates is the rating adhesion by tape test method according to the ASTM D 3359. The surface of the thin film scratched with cutting tool to form a lattice pattern with either six or eleven cuts in each direction is made through the film to the substrate. The surface is scratched to form 8 parallel lines (first lines) approximately 20mm long and 1mm between each adjacent lines in one direction, and other 8 lines (second lines) were scratched at 90° in direction to the first 8 lines as shown in Fig. (2). A tape was applied to the thin film and peeled away at 60° then observed by an optical microscope. The adhesion is estimate qualitatively on a scale of (0B, 1B, 2B, 3B, 4B, 5B) according removed area percent of thin film (>65%, 35-65%, 15-35%, 5-15%, <5%, 0%), respectively.

Fig. (1) Autoclave and Teflon rack used to deposit CuO thin film hydrothermally on FTO substrate

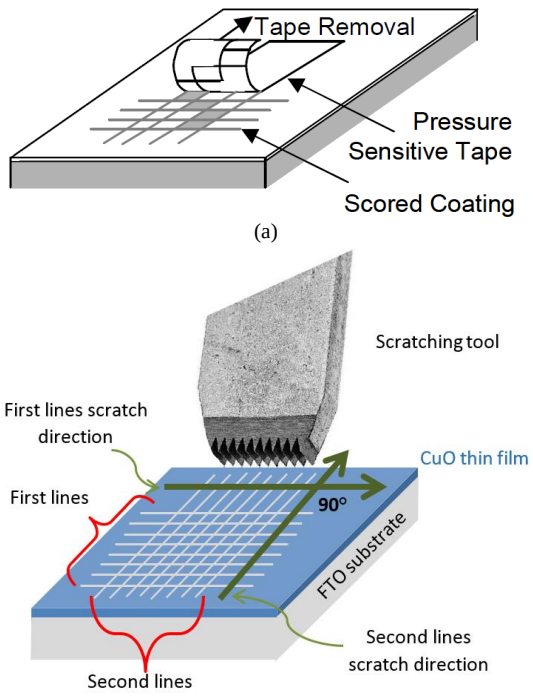

Fig. (2) (a) Schematic graph to demonstrate adhesion test method, and (b) scratching tool to form lattice pattern

 ISSN (print) 1813-2065, (online) 2309-1673

Special tape is used to estimate the percentage ratio of the removed area [26]. Scanning electron microscopic images were recorded using Thermo Fisher Scientific scanning electron microscope supported with an energy dispersive spectroscopy (EDS) equipment with energy from 0 to 20keV.

3. Results and Discussion

The strength of bond between the materials of thin film and substrate is an important limitation in various applications. Adhesion or bond strength is the measured force or work required to separate the thin film away from the substrate. For a thin film to fulfill its function of permanence and high durability, it must have a good adherence to the substrate. [27,28]. Figure (3a) shows CuO thin film deposited on FTO using hydrothermal method. The film was brownish-black color. Figure (3b) shows the film after scratching to estimate the adhesion capability of CuO on FTO. The percentage of the delaminated area was measured using Image J software. The percentage of the removed area was 3.38% which is less than 5% and rated as 4B according to the ASTM D 3359. In conclusion, we can say that CuO thin film had a strong adhesion to FTO substrate. For bare glass (without FTO), we noted some voids in the samples due to weak adhesion between CuO and glass. The adhesion of CuO to FTO appears to more efficient than CuO on bare glass. This may depend upon a number of factors such as the affinity of the substrate, the film structure, and the amount of oxygen in the film [29]. In this case a mediated seed layer is needed. The seed layer can be metal such as Au or metal oxide such as low thickness layer of CuO [30].

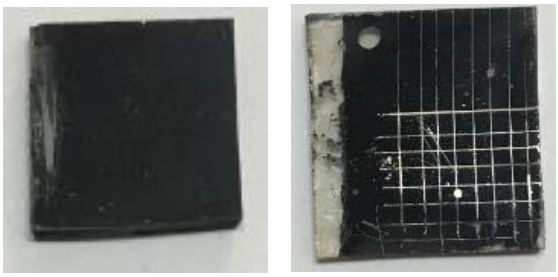

(a) **(b)**

Fig. (3) (a) CuO film deposited on FTO substrate, and (b) scratched CuO film on FTO substrate for adhesion test

Figure (4) shows the X-ray diffraction pattern for CuO thin film deposited on FTO substrate. In order to assign the peaks clearly, we plotted two ranges of 2θ, i.e., (a) 2θ=0-45°, (b) 2θ=45-90°. The most prominent peaks for CuO are 2θ=35.72°, 38.83°, 58.56°, 48.86°, 66.44°, 72.64° and 83.76°. No other peak attributed to other phases are found. This demonstrates that pure CuO is the sole product formed in our route. The crystallite sizes of the deposited CuO thin films were calculated by Scherrer's analysis using the full width at half maximum (FWHM) data for each peak. The average crystallite size of CuO thin films were 34, 52, and 28 nm respectively according to Scherrer's analysis. The data are in good agreement with a previous study [31]. Table (1) summarizes the obtained results.

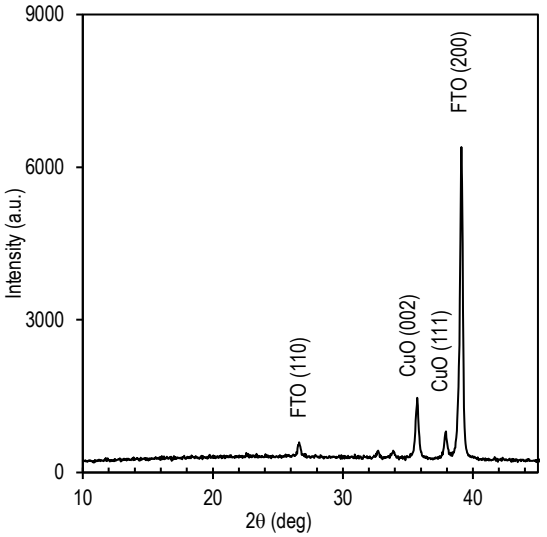

(a)

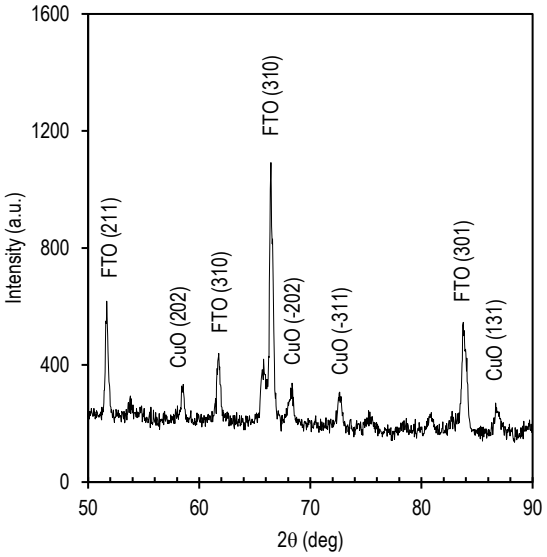

(b)

Fig. (4) XRD patterns of CuO nanosheets deposited on FTO substrate using hydrothermal technique: (a) 2θ=0-45°, and (b) 2θ=45-90°

Field-emission scanning electron microscope (FE-SEM) is used to capture the microstructure image of the cupric thin films produced by hydrothermal technique. Figure (5) shows the images of FE-SEM at different magnification scales (scale bars 500 nm to 5 μm). The structure of CuO reveals a distribution of irregular nanosheets with thickness in the range from 20 to several micrometers. The average particle size of the CuO is quite big up to 3 μm. The shapes of the nanosheets are identical to those in previous works [32,33].

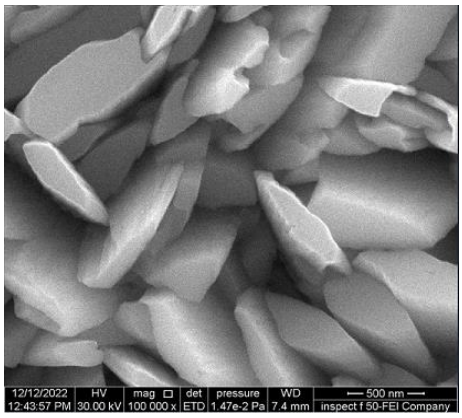

(a)

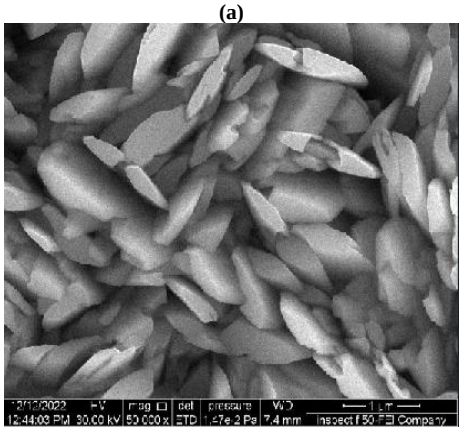

(b)

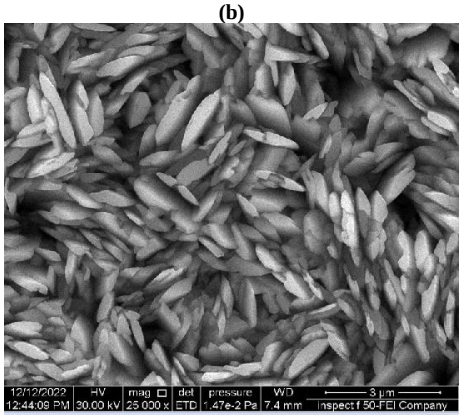

(c)

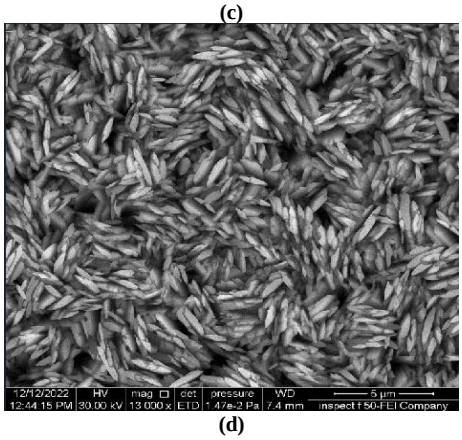

(d)

Fig. (5) FE-SEM images for CuO nanostructures prepared by hydrothermal method (a) scale bar 500 nm, (b) scale bar 1 µm, (c) scale bar 3 µm, (d) scale bar 5 µm

Figure (6) shows energy-dispersive spectroscopy (EDS) for CuO nanosheets prepared by hydrothermal method. The peaks of EDS clearly illustrate the presence of only peaks corresponding to Cu and O elements with negligible peak (0.6%) attributed to silicon which is believed to be assigned to the glass substrate (SiO_2). The observed atomic ratio of 50.7%: 48.7% as indicated in table (2), which is approximately 1:1 between Cu and O elements confirms the presence of CuO in these films. This result is compatible with those of XRD analysis and it suggests that the films predominantly contain CuO. The excess O (50.7-48.7=2%) observed in EDS is originating from FTO substrate. There were no peaks related to the elements other than Cu, O and Si in the EDS spectra, which confirms the formation of phase pure CuO in the thin films prepared through hydrothermal technique.

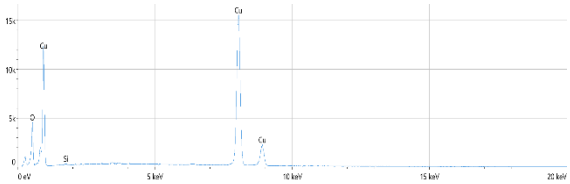

Fig. (6) EDS spectra of CuO thin films on FTO substrate by hydrothermal technique

Table (2) EDS data for CuO thin film on FTO substrate

Element	Atomic %	Atomic % Error	Weight %	Weight % Error
O	50.7	0.4	20.6	0.2
Si	0.6	0.1	0.4	0.0
Cu	48.7	0.2	78.9	0.3

For an optoelectronic application, a dye sensitized photodetector (DSPD) with CuO as as counter electrode has been fabricated (Figure 7). The proposed structure of DSPD is identical to that for dye sensitized solar cell but with CuO as platinium-alternative counter electrode. Figure 8 shows responsivity of CuO based DSPD with standard (Platinium) and alternative (CuO) counter electrodes. The photocurent values were recorded for different wavelength emitted from LEDs. The two samples show high responsivity in the range (460-590 nm). Although DSPD with CuO as a counter electrode showed higher respnsivity in the short wavelengths region (450-570 nm) [34], we think that the high photo-response region in our dye sensitized solar cells at about 520 nm is mostly coming from the dye (N719) which has an identical peak absorption at 520 nm [35]. This is reasonable since the thickness of titanium electrode (TiO_2+N719) is about 10 micrometers which is about 10 times higher than the average thickness of CuO electrode. We think the

 ISSN (print) 1813-2065, (online) 2309-1673

contribution of CuO absorption in the total absorption of DSSCs is minor.

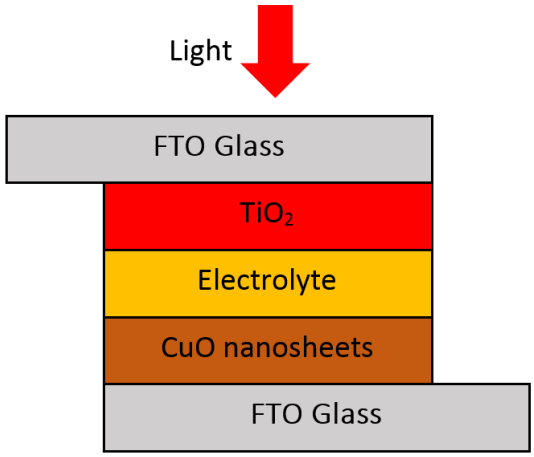

Fig. (7) Dye-sensitized photodetecter with CuO nanosheet thin film as a counter electrode

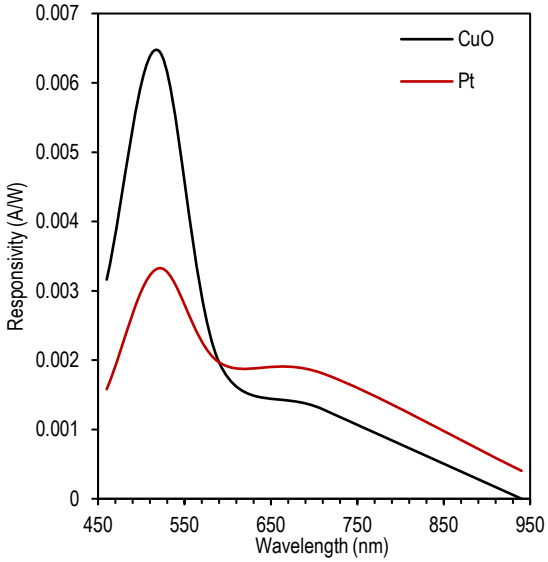

Fig. (8) Responsivity of CuO based DSPD for visible and near IR light

4. Conclusions

CuO thin films with nanosheets structure have been synthesized using simple and cost-effective hydrothermal method. The as deposited nanosheets exhibited polycrystalline structure with monoclinic system. The prepared samples were pure in phase. The films are composed of large micro and nanosheets. The high (area to volume) ratio offered by CuO nanosheets can be invested optoelectronically to fabricate alternative counter electrode in dye sensitized photodetectors and solar cells.

References

[1] A.H. Mustafa, M.M. Sadeer and S.A. Duha, "Preparation Doped CuO Thin Film and Studies of Its Antibacterial Activity", *Acta Phys. Pol. A*, 135 (2019) 4.

[2] S.D. Alghamdi, A.O.M. Alzahrani and M.S. Aida, "Effect of molarity on the properties of CuO thin films prepared by air-pressurized spray pyrolysis", *J. Optics*, 52 (2023) 803-809.

[3] Z.M. Sadiq, M.A. Hassan and K.I. Hassoon, "Preparation and Characterization of CuO Nanostructured Thin Films by Chemical Bath Deposition", *J. Phys.: Conf. Ser.*, 2322(1) (2022) 012088.

[4] R. Bunea, A.K. Saikumar and K. Sundaram, "A comparison of optical properties of CuO and Cu_2O thin films for solar cell applications", *Mater. Sci. Appl.*, 12(7) (2021) 315-329.

[5] M.M. Ibrahim, M.A. Hassan and K.I. Hassoon, "Novel route to prepare iron sulphide as a counter electrode for dye-sensitized solar cell", *Bull. Mater. Sci.*, 46(3) (2023) 120.

[6] Ş. Baturay et al., "n-Type conductivity of CuO thin films by metal doping", *Appl. Surf. Sci.*, 477 (2019) 91-95.

[7] A.N. Hussain, K.I. Hassoon and M.A. Hassan, "Effect of annealing on copper oxide thin films and its application in solar cells", *J. Phys.: Conf. Ser.*, 1530(1) (2020) 012140.

[8] H.J. Song et al., "High-performance copper oxide visible-light photodetector via grain-structure model", *Sci. Rep.*, 9(1) (2019) 7334.

[9] A.D. Faisal, A.A. Aljubouri and W.K. Khalef, "Photodetector fabrication based on heterojunction of CuO/SnO_2/Si nanostructures", *Bull. Mater. Sci.*, 45(2) (2022) 84.

[10] R. Motoyoshi et al., "Structure and photovoltaic activity of cupric oxide-based thin film solar cells", *J. Cer. Soc. Japan*, 118(1383) (2010) 1021-1023.

[11] M. Dahrul and H. Alatas, "Preparation and optical properties study of CuO thin film as applied solar cell on LAPAN-IPB Satellite", *Proc. Env. Sci.*, 33 (2016) 661-667.

[12] S. Steinhauer, "Gas sensors based on copper oxide nanomaterials: A review", *Chemosens.*, 9(3) (2021) 51.

[13] B.R. Bade et al., "Hydrothermally synthesized CuO nanostructures and their application in humidity sensing", *AIP Conf. Proc.*, 2335(1) (2021) 100001).

[14] Z. Deng et al., "Boosting lithium-ion storage capability in CuO nanosheets via synergistic engineering of defects and pores", *Front. In Chem.*, 6 (2018) 428.

[15] P. Wang et al., "Facile synthesis of CuO nanochains as high-rate anode materials for lithium-ion batteries", *New J. Chem.*, 43(17) (2019) 6535-6539.

[16] W.Z. Tawfik et al., "Sputtered cobalt doped CuO nano-structured thin films for photoconductive sensors", *J. Mater. Sci.: Mater. In Electron.*, 30 (2019) 1275-1281.

[17] G.S. Gund et al., "Porous CuO 65anosheets clusters prepared by a surfactant assisted hydrothermal method for high performance

supercapacitors", *RSC Adv.*, 46(3) (2013) 24099-24107.
[18] M.Y. Ghotbi and Z. Rahmati, "Nanostructured copper and copper oxide thin films fabricated by hydrothermal treatment of copper hydroxide nitrate", *Mater. Design*, 85 (2015) 719-723.
[19] A.M. Teli et al., "TOPO mediated rapid hydrothermal synthesis and study of electrochemical performance of nano-structured copper oxide thin films", *Sust. Ener. Fuels*, 1(2) (2017) 377-386.
[20] M. Ozga et al., "Ultra-fast growth of copper oxide (II) thin films using hydrothermal method", *Mater. Sci. Semicond. Process.*, 120 (2020) 105279.
[21] R. Mroczyński et al., "Hydrothermally formed copper oxide (CuO) thin films for resistive switching memory devices", *Sol. Stat. Electron.*, 194 (2022) 108357.
[22] K. Subalakshmi et al., "Platinum-free metal sulfide counter electrodes for DSSC applications: Structural, electrochemical and power conversion efficiency analyses", *Solar Energy*, 193 (2019) 507-518.
[23] J. Theerthagiri et al., "Recent progress in non-platinum counter electrode materials for dye-sensitized solar cells", *Chem. Electro. Chem.*, 2(7) (2015) 928-945.
[24] S. Yun, P.D. Lund and A. Hinsch, "Stability assessment of alternative platinum free counter electrodes for dye-sensitized solar cells", *Energy Env. Sci.*, 8(12) (2015) 3495-3514.
[25] S. Sonia et al., "Hydrothermal synthesis of highly stable CuO nanostructures for efficient photocatalytic degradation of organic dyes", *Mater. Sci. Semicond. Process.*, 30 (2015) 585-591.
[26] A.S. Maxwell, "Review of Test Methods for Coating Adhesion", Nat. Phys. Lab. Teddington, Middlesex (2001).
[27] J.E. Lee, H.J. Kim and D.E. Kim, "Assessment of adhesion between thin film and silicon based on a scratch test", *J. Mech. Sci. Technol.*, 24 (2010) 97-101.
[28] J.E. Pawel and C.J. McHargue, "Testing of adhesion of thin films to substrates", *J. Adhes. Sci. Technol.*, 2(1) (1988) 369-383.
[29] P. Benjamin and C. Weaver, "Adhesion of metal films to glass", *Proc. Royal Soc. London. Ser. A. Math. Phys. Sci.*, 254(1277) (1960) 177-183.
[30] M. Merschky et al., "Using a metal oxide adhesion layer and wet chemical cu metallization for fine line pattern formation on glass", *in Int. Symp. on Microelectron., Int. Microelectron. Assem. Packag. Soc.*, 1 (2017) 458-463.
[31] W. Xia et al., "Different annealing atmosphere gases on the growth and photocurrent performance of CuO films grown on FTO substrate", *ACS Omega*, 3(9) (2018) 11354-11361.
[32] Y. Zou et al., "Flower-like CuO synthesized by CTAB-assisted hydrothermal method", *Bull. Mater. Sci.*, 34 (2011) 967-971.
[33] A. Umar et al., "CuO nanosheets as potential scaffolds for gas sensing applications", *Sens. Actuat. B: Chem.*, 250 (2017) 24-31.
[34] M.A. Hassan, M.H. Mohsin and R.A. Ismail, "Preparation of high-responsivity strontium–doped CuO/Si heterojunction photodetector by spray pyrolysis", *J. Mater. Sci.: Mater. In Electron.*, 34(10) (2023) 912.
[35] F. De Angelis et al., "Absorption spectra and excited state energy levels of the N719 dye on TiO_2 in dye-sensitized solar cell models", *J. Phys. Chem. C*, 115(17) (2011) 8825-8831.

Table (1) Scherrer's analysis for CuO film deposited on FTO substrate using hydrothermal method, d is the spacing distance, FWHM is full-width at half maximum, D is the crystallite size, S is the dislocation defects density and ε lattice strain

Peak no.	2θ (deg)	d (nm)	FWHM (deg)	D (C.S.) (nm)	$S=1/D^2$ (lines/nm^2)	$\varepsilon = \beta\cos\theta/4$ ($\times10^{-3}$)
1	35.7146	0.2514	0.2600	34	0.00086	1.08
2	38.8347	0.2319	0.1694	52	0.00037	0.69
3	48.8621	0.1864	0.3257	28	0.00127	1.29

 ISSN (print) 1813-2065, (online) 2309-1673 PRINTED IN IRAQ

IRAQI JOURNAL OF APPLIED PHYSICS
Vol. 19, No. 4A, October 2023, pp. 67-72

Asmaa D. Nusseif
Nedal A. Hussain
Raad S. Sabry

Department of Physics, College of Science, Mustansiriyah University, Baghdad, 10052, IRAQ

Preparation and Wettability of Zinc Oxide Nanostructures by Oxidation of Zinc Foil in Hot Water

Zinc oxide (ZnO) nanostructures have been prepared by wet oxidation method using hot water treatment of zinc foil at 90°C. The prepared nanostructures were characterized using diverse techniques. X-ray diffraction results confirmed the formation of hexagonal wurtzite structure ZnO with averge crystallite size of 32 nm and 40 nm for wet oxidation at 4 h and 10 h, respectively. Depending on the oxidation time, field emission scanning electron microscopy identifies two distinct morphologies: hierarchical micro- and nanoscale structures and rod-like structures. The wettability of ZnO surfaces is confirmed by water contact angle measurements.Wet oxide ZnO surface at 4 h exhibited hydrophobic-strong adhesion behavior with a water contact angle of 148°±1°. Superhydrophobic- low adhesion behavior was revealed by the wet oxide ZnO surface at 10 h with water contact angle of 151°±1°.The samples wettability showed good stability after one year of storage in an ambient environment.

Keywords: Zinc oxide; Nanostructures, Wet oxidation, Wettability
Received: 11 June 2023; **Revised:** 15 August 2023; **Accepted:** 22 August 2023

1. Introduction

The wettability of solid surfaces is critical and determines their applications. When a liquid spreads equally over the surface without forming any droplets, the surface is called wetted. In the case of water, the surface is called hydrophilic. The surface is said to be hydrophobic when water forms droplets on it [1-4]. The direct definition of surface wettability is the contact angle of a water droplet on a solid surface [5,6]. A surface is said to be hydrophilic when the water contact angle (WCA) is less than 90° [7]. If the contact angle is greater than 90° and less than 150°, the surface is termed hydrophobic. At a water contact angle exceeding 150, a surface is classified as superhydrophobic [8,9]. The lotus leaf (Nelumbo nucifera) and the red rose (Rosea rehd) are examples of naturally superhydrophobic surfaces observed in nature [10,11]. Although both exhibit superhydrophobic behavior, they differ significantly in terms of water adhesion properties, which are determined by dynamic contact angle measurements (hysteresis contact angle and sliding angle) [12-14]. Since the discovery of these bio-inspired regimes, researchers have invented numerous approaches and procedures for creating superhydrophobic surfaces [15-18]. These surfaces have grown in interest over recent decades because of their desirable properties and potential applications. Among numerous metal oxides, zinc oxide (ZnO) reveals unique structural and functional properties, especially at the nanoscale [19,20]. ZnO that is intrinsically hydrophilic because of the hydroxyl group's presence on its surface [21]. It is possible to modify hydrophilic surfaces to produce superhydrophobic surfaces using two main steps: one is by roughening the surfaces, and the other is by modifying the rough surfaces with low surface energy materials [22,23]. Surface roughness with micro, nano, or hierarchical scales having both plays an important role in obtaining superhydrophobic surfaces [24,25]. Hydrothermaly grown ZnO nanorods on zinc surfaces exhibit superhydrophobic and ice-phobic behavior with water contact angles higher than 165° and tilting angles as low as 1° [26]. Hierarchical ZnO nanostructures were fabricated by a simple chemical method exhibiting superhydrophobic properties without using any low surface energy additives or modifiers [27]. A variety of attempts have been made to obtain superhydrophobic ZnO surfaces employing various chemical and physical methods [28-31]. Many of these methods require costly and complicated equipment, high temperatures, multistep procedures, and specialized reagents. On the other hand, it is imperative to develop simple, low-cost, and reproducible synthetic methods for large-scale industrial and commercial applications. Recently, a wet oxidation process using hot water has been employed to grow several metal oxide nanostructures at low temperatures [32]. There are many documented studies on the synthesis of ZnO nanostructures grown on different substrates using the wet oxidation method [33-36]. This synthesis process is simple, cost-effective, high-throughput, non-toxic, and environmentally friendly since only deionized water was used in the synthesis process. Zinc oxide superhydrophobic surfaces are widely employed in many applications, including self-

cleaning, ice-phobicity, oil-water separation, anticorrosion, and antibacteriality [37-41].

The present study describes zinc oxide nanostructures prepared by wet oxidation of a zinc foil substrate on hot deionized water. The influence of oxidation time on the structure and morphology of the resulting nanostructures has been studied. The wettability properties of ZnO nanostructured surfaces were investigated and confirmed by water contact angle (WCA) experiments.

2. Material and methods

High purity zinc foil (99.99% Zn from Sigma Aldrich) was used as the substrate and zinc source. The foil was cut into small pieces (1.5×1.0×0.3 cm) and ultrasonically cleaned in acetone for 15 minutes. Before the oxidation process, zinc foil was chemically etched with diluted hydrochloric acid (5 wt% in ethanol, HCl from Sigma Aldrich) by immersion samples for 5 min. The wet oxidation process was performed by immersing samples in 100 ml of hot, deionized water at a temperature of 90 °C for 4 and 10 hours. Finally the samples were then dried by blowing them with hot air.

Various techniques have been used to characterize ZnO nanostructures prepared by wet oxidation method. The crystal structure was determined by X-ray diffraction (XRD) using a Miniflex II, Rigaku, Japan, CuKα radiation, λ = 1.5408 Å diffractometer with 2θ ranging from 20° to 80°. A Hitachi S-4160 field-emission scanning electron microscope (FE-SEM) was used to reveal the surface morphology of the ZnO nanostructures. The wettability of the ZnO surfaces was evaluated by water contact angle (WCA) measurements using a homemade contact angle measuring instrument. A 5 µL sized deionized water droplets were carefully distributed on the surface. The digital images of water droplets were captured by a high-speed CCD camera with a setting of 25 frames per second were then analyzed using the ImageJ analysis software. The measurements were performed on at least five different regions of the surface to provide a mean value. The scheme of the instrument used to measure the contact angle is shown in Fig. (1).

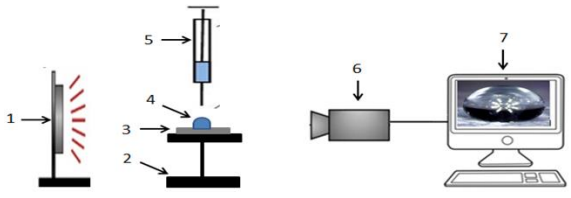

Fig. (1) Scheme for water contact angle instrument (1: light source, 2: stand, 3: sample, 4: water droplet, 5: syringe, 6: CCD camera, 7: computer)

3. Results and Discussion

Figure (2) shows the x-ray diffraction (XRD) patterns of ZnO nanostructures grown on zinc foil substrates at 90°C for different wet oxidation times. The diffraction peaks at 2θ of 31.47°, 34.18°, 36.2°, 47.5°, 56.6°, 62.8°, and 67.8° correspond to the (100), (002), (101), (102), (110), (103), and (200) diffraction planes, are related to ZnO with a hexagonal wurtzite structure in accordance with the Joint Committee on Powder Diffraction Standards (JCPDS card no. 36-1451).

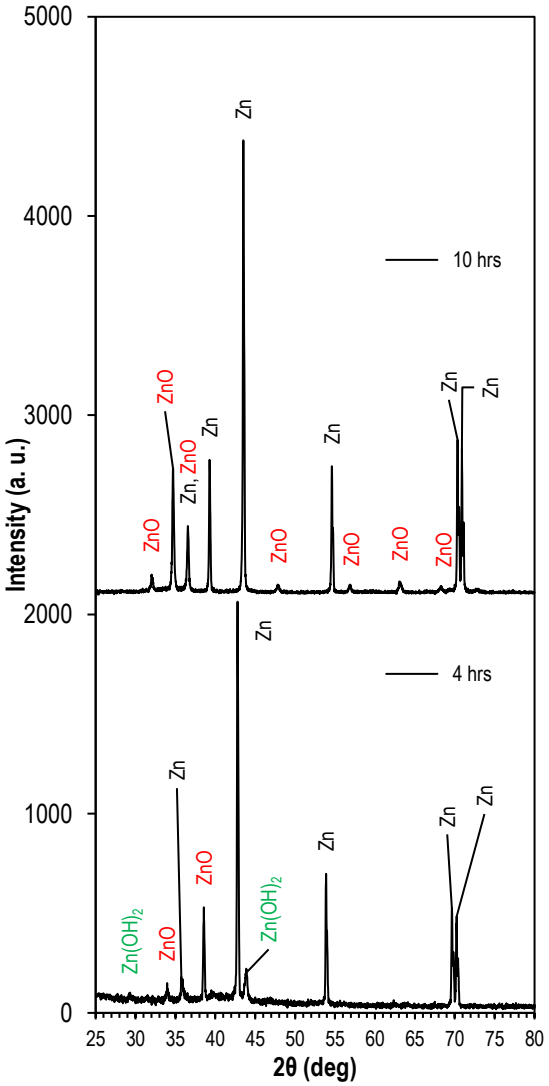

Fig. (2) XRD patterns of wet oxidized ZnO nanostructures at 90°C for different times (a) 4 hrs and (b) 10 hrs

The highest intense (002) peak observed at 34.18° in the XRD patterns reveals that the ZnO nanostructures suggest preferential growth along the [001] direction. The peaks correspond to the underlying metallic zinc foil substrate are also observed (JSPDS card no. 04-0831). It should be noted that the (002) peak of metallic Zn at 36.2° overlaps with the (101) peak of ZnO. An increase in the number and intensity of diffraction peaks that corresponds to ZnO composition with metallic Zn peaks as the oxidation time increases suggests an increase in the concentration of ZnO on the surface of the zinc foil as oxidation proceeds. XRD pattern of ZnO nanostructures grown on zinc foil substrates for

 ISSN (print) 1813-2065, (online) 2309-1673

4 hours shows two diffraction peaks at 29.30° and 43.90° belonging to $Zn(OH)_2$ (JCPDS card no. 38-0385), which decomposes into ZnO as the oxidation time is increased. Observed shift in the peaks between the two cases is related to the instrumental error during the measurements.

The crystallite size of ZnO nanostructures can be estimated from the highest intensity peak (002) using the Scherrer's formula. The calculated crystallite size was found to be 32 and 40 nm for wet oxidation at 4 hours and 10 hours, respectively.

The surface morphology of zinc foil after wet oxidation at 90°C is shown in Fig. (3). It can be clearly observed from the FE-SEM image after wet oxidation for 4 hours (Fig. 3a) that the sample morphology consists of spherical-like microstructures covered with porous nanosheets (see the magnified image in Fig. (3b and c). The average size of spherical-like microstructures is about 4 µm. The sheet thickness is about 24 nm, and their diameter is averaged at 134 nm. As the wet oxidation time increased to 10 hours, the surface morphology changed to nanorod-like structures (Fig. 3d, e and f with different magnifications). It can be seen that these rods have a diameter average of 86 nm and a length average of 670 nm.

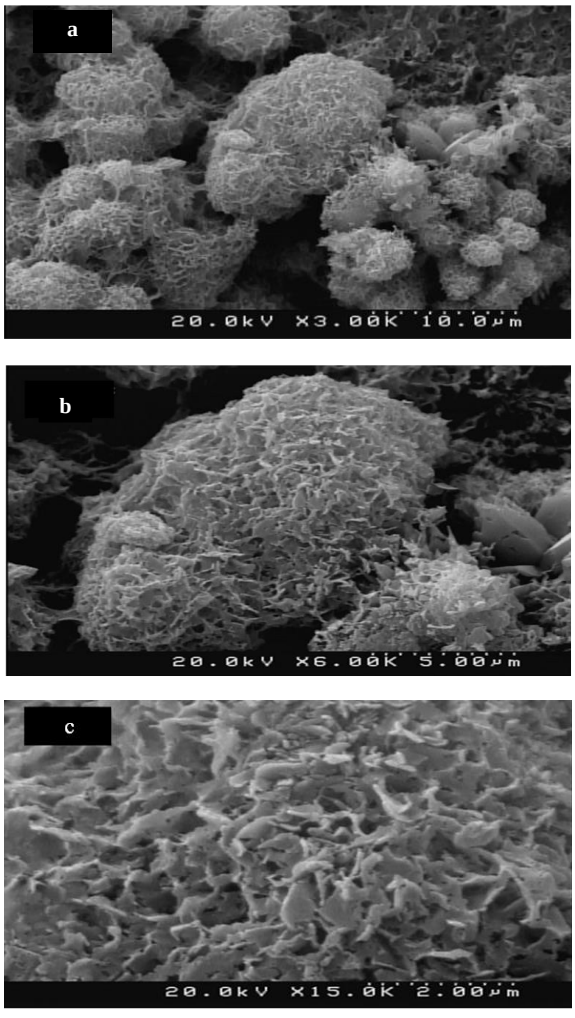

Fig. (3) Top-view FE-SEM images (with different magnifications) of wet oxidized ZnO nanostructures at 90°C for different times (a,b,c) 4 hrs and (d,e,f) 10 hrs

The wettability of ZnO surfaces was investigated. Figure (4) shows photographs of water droplets on the ZnO surfaces wet oxidized at 90°C for 4 and 10 hours. Both samples exhibited hydrophobic properties. The hydrophobicity of ZnO surfaces is attributed to their surface roughness. The wet oxidized ZnO surface for 4 hours showed hydrophobic behavior with a WCA of approximately 148±1° and high water droplet adhesion (see Fig. 4a). The water droplet does not fall off even when the sample is turned upside down, as shown in Fig. (4b). The formation of hierarchical structures having both micro- and nano-roughness increases the effective surface area, causing water droplets to spread less on the surface and penetrate into the grooves of the surface. Having a very high adhesion to the surface leads to an idealized sticky hydrophobic state, this is in good agreement with the Wenzel model [42]. Wenzel's state involves the fact that the water droplet filling up the grooves of the surface makes complete wet-contact mode with the solid surface, resulting in a high contact angle hysteresis (CAH). Owing to the high adhesive force, the water droplet is unable to slide on the surface.

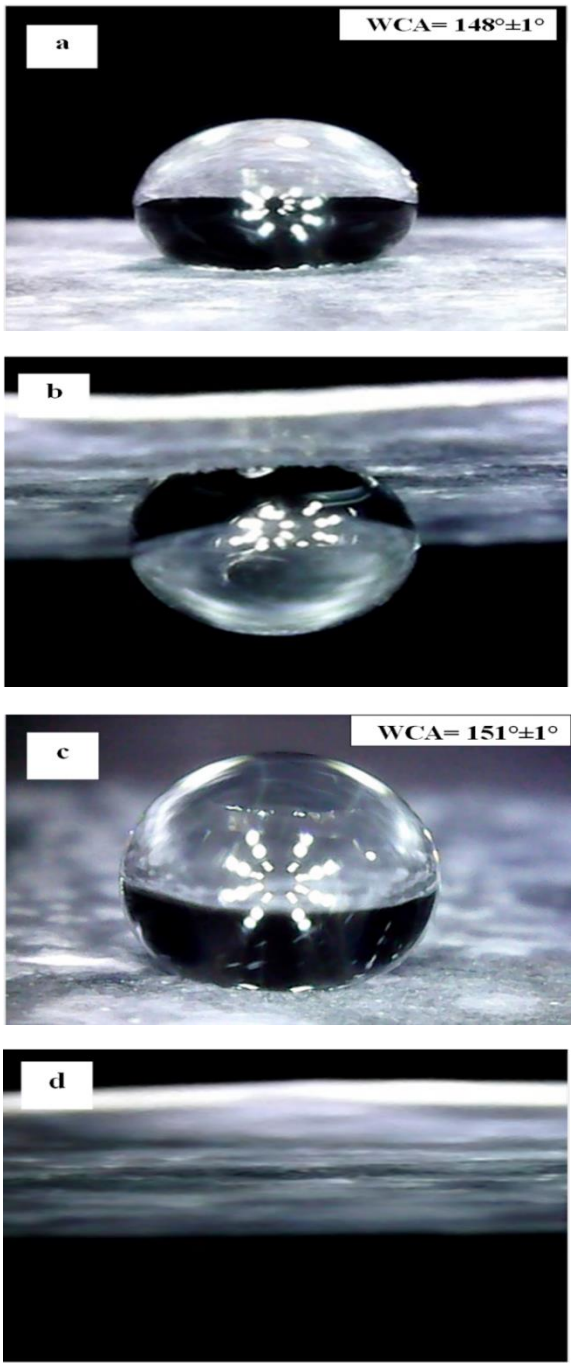

Fig. (4) Water droplet photographs on ZnO surfaces wet oxidized at 90°C for (a) 4 hrs and (c) 10 hrs. Figures (b) and (d) are upside-down photographs of water droplets on (a) and (c)

Wet oxidized ZnO surfaces for 10 hours exhibited superhydrophobic behavior with a WCA of (151±1°) and low water droplet adhesion as shown in Fig. (4b). The water droplet moves very freely with a very small tilt angle and falls off when the samples are turned upside down. The photograph of a water droplet cannot capture (see Fig. 4d). The formation of nanorod morphology as wet oxidation time increased caused air to be trapped under water droplets, minimizing the contact between the water droplet and the surface. Water contact angles improve, and the surface behavior changes from hydrophobic to superhydrophobic. The superhydrophobic behavior of this sample can be described by the Cassie-Baxter model [43], in which, it is presumed that the grooves under the droplet are filled with air instead of liquid. A water droplet is suspended on the top of the irregular structure in a non-wet-contact mode with low contact angle hysteresis. The water droplet is able to roll off easily due to its low adhesive force. The most noticeable differences in samples hydrophobicity are found by varying the wet oxidation time. To find out the effect of the surrounding environment on the wettability of the prepared samples, they were stored for a year in an ambient environment. The water contact angle was measured after that, and no significant change was observed during this period for both ZnO samples.

4. Conclusion

Zinc oxide nanostructures are successfully prepared on zinc foil substrates via a convenient approach based on wet oxidation using hot deionized water. Oxidation time has a significant effect on nanostructured ZnO morphology. The surface of nanostructured ZnO exhibits both hydrophobic and superhydrophobic wetting behavior depending on surface morphology. Hydrophobic ZnO surfaces with a water contact angle of 148° and high adhesion were obtained after wet oxidation at 90°C for 4 hours. A low-water-adhesion superhydrophobic surface with a water contact angle of 151° was obtained as the oxidation time increased to 10 hours. The samples showed good durability and stability against environmental conditions.The prepared ZnO surfaces can be used for specific applications.

References

[1] E. Jiaqiang et al., "Wetting models and working mechanisms of typical surfaces existing in nature and their application on superhydrophobic surfaces: a review", *Adv. Mater. Interf.*, 5(1) (2018) 1701052.

[2] V.J. Raj et al., "Application of zinc oxide nanoflowers in environmental and biomedical science", *BBA Adv.*, 2 (2022) 100051.

[3] A. Verbič et al., "Designing UV-protective and hydrophilic or hydrophobic cotton fabrics through in-situ ZnO synthesis using biodegradable waste extracts", *Appl. Surf. Sci.*, 599 (2022) 153931.

[4] R. Li et al., "A pine needle-like superhydrophobic Zn/ZnO coating with excellent mechanochemical robustness and corrosion resistance", *Mater. Des.*, 225 (2023) 111583.

[5] X. Li, D. Reinhoudt and M. Crego-Calama, "What do we need for a superhydrophobic surface? A review on the recent progress in the preparation of superhydrophobic surfaces", *Chem. Soc. Rev.*, 36(8) (2007) 1350-1368.

[6] D. Klaas et al., "Development of a Humidity Sensor Element based on sputter deposited thin

 ISSN (print) 1813-2065, (online) 2309-1673

ZnO-Layers", *Proced. Technol.*, 26 (2016) 27-34.
[7] J. Simpson, S. Hunter and T. Aytug, "Superhydrophobic materials and coatings: a review", *Rep. Prog. Phys.*, 78(8) (2015) 086501.
[8] F. Ma et al., "Geometrical effect, optimal design and controlled fabrication of bio-inspired micro/nanotextures for superhydrophobic surfaces", *Mater. Res. Express*, 4(9) (2017) 092001.
[9] R.-Q. Chen et al., "Zinc oxide nanostructures and porous films produced by oxidation of zinc precursors in wet-oxygen atmosphere", *Prog. Nat. Sci.: Mater. Int.*, 21 (2011) 81-96.
[10] T. Darmanin and F. Guittard, "Supehydrophobic and superoleophobic properties in nature", *Mater. Today*, 18(5) (2015) 273-285.
[11] T. Yuki et al., "Fabrication of layered hydroxide zinc nitrate films and their conversion to ZnO nanosheet assemblies for use in dye-sensitized solar cells", *J. Asian Cer. Soc.*, 3 (2015) 144-150.
[12] O. Gotlib et al., "Investigation of an improved electricidal coating for inhibiting biofilm formation on urinary catheters", *J. Mater. Res. Technol.*, 10 (2021) 339-348.
[13] L. Feng et al., "Petal Effect: A Superhydrophobic State with High Adhesive Force", *Langmuir*, 24(8) (2008) 4114-4119.
[14] J. Law et al., "Bioinspired Ultrahigh Water Pinning Nanostructures", *Langmuir*, 30(1) (2014) 325−331.
[15] S. Xu, Q. Wang and N. Wang, "Chemical fabrication strategies for achieving bio-inspired superhydrophobic surfaces with micro and nanostructures: A review", *Adv. Eng. Mater.*, 23(3) (2021) 2001083.
[16] C. Xue et al., "Large-area fabrication of superhydrophobic surfaces for practical applications: an overview", *Sci. Technol. Adv. Mater.*, 11(3) (2010) 033002.
[17] V. Ganesh et al., "A review on self-cleaning coatings", *J. Mater. Chem.*, 21(41) (2011) 16304-16322.
[18] E. Celia et al., "Recent advances in designing superhydrophobic surfaces", *J. Colloid Interf. Sci.*, 402 (2013) 1-18.
[19] W. Zhu, Y. Wu and Y. Zhang, "Fabrication and characterization of super hydrophobicity ZnO nanoparticles with two morphologies by using stearic acid", *Mater. Res. Exp.*, 6(11) (2019) 1150d1.
[20] R. Sha et al., "ZnO nano-structured based devices for chemical and optical sensing applications", *Sens. Actuat. Rep.*, 4 (2022) 100098.
[21] M. Myint et al., "Superhydrophobic surfaces using selected zinc oxide microrod growth on ink-jetted patterns", *J. Colloid Interf. Sci.*, 354(20) (2011) 810-815.
[22] M. Myint et al., "Hydrophobic/hydrophilic switching on zinc oxide micro-textured surface", *Appl. Surf. Sci.*, 264 (2013) 344-348.
[23] E. Velayiand and R. Norouzbeigi, "Robust superhydrophobic needle-like nanostructured ZnO surfaces prepared without post chemical-treatment", *Appl. Surf. Sci.*, 426 (2017) 674-687.
[24] X. Hao et al., "Superhydrophobic surfaces based on ZnO-constructed hi-erarchical architectures", *Microelectronic Eng.*, 141 (2015) 44-50.
[25] M. Ebrahimi et al., "Sustainable superhydrophobic branched hierarchical ZnO nanowires: Stability and wettability phase diagram", *Appl. Surf. Sci.*, 561 (2021) 150068.
[26] M. Balordi, F. Pini and G. Magistris, "Superhydrophobic ice-phobic zinc surfaces", *Surf. Interfaces*, 30 (2022) 101855.
[27] E. Velayi and R. Norouzbeigi, "Synthesis of hierarchical superhydrophobic zinc oxide nano-structures for oil/water separa-tion", *Ceram. Int.*, 44(12) (2018) 14202-14208.
[28] P. Kumar et al., "Hydrophobic ZnO nanostructured thin films on glass substrate by simple successive ionic layer absorption and reaction (SILAR) method", *Thin Solid Films*, 518(24) (2010) e183-e186.
[29] R. Mardosaitė, A. Jurkevičiūtė and S. Račkauskas, "Superhydrophobic ZnO Nanowires: Wettability Mechanisms and Functional Applications", *Cryst. Growth Des.*, 21(8) (2021) 4765-4779.
[30] L.Yanbo et al., "Fabrication of Hierarchical ZnO Architectures and Their Superhydrophobic Surfaces with Strong Adhesive Force", *Inorg. Chem.*, 47(8) (2008) 3140-3143.
[31] X. Hou et al., "Superhydrophobic zinc oxide surface by differential etching and hydrophobic modification", *Mater. Sci. Eng. A*, 452-453 (2007) 732-736.
[32] N. Saadi, L. Hassan and T. Karabacak, "Metal oxide nanostructures by a simple hot water treatment", *Sci. Rep.*, 7 (2017) 7158.
[33] M. Balela, C. Pelicano and Z. Lockman, "*in situ* mixed potential study of the growth of zinc oxide hierarchical nanostructures by wet oxidation of zinc foil", *J. Mater. Sci.*, 52 (2017) 2319-2328.
[34] O. Farhat et al., "Growth of ZnO Nanostructures by Wet Oxidation of Zn Thin Film Deposited on Heat-Resistant Flexible Substratesat Low Temperature", *Semicond.*, 54 (2020) 1220-1223.
[35] M. Balela et al., "Formation of zinc oxide nanostructures by wet oxidation of vacuum deposited Zn thin film", *Opt. Quantum Electron.*, 49 (2017) 3.
[36] O. Farhat et al., "Fabrication and characterization of ZnO nanowires by wet oxidation of Zn thin film deposited on Teflon

substrate", *Superlat. Microstruct.*, 86 (2015) 236-242.
[37] M. Banik et al., "Colloidal Transfer Printing–Mediated Fabrication of Zinc Oxide Nanorods for Self-Cleaning Applications", *Adv. Mater. Interfaces*, 6(9) (2019) 1900063-1900072.
[38] Y. Bao et al., "Fabrication of anti-icing/de-icing superhydrophobic composite coating based on hydrangea-like ZnO@CuS", *Sol. Ener. Mater. Sol. Cells*, 245 (2022) 111838.
[39] R. Sutar et al., "Oil–Water Separation by ZnO-Based Superhydrophobic PU Sponges", *Macromol. Symp.*, 393(1) (2020) 2000036.
[40] M. Selim et al., "Facile design of graphene oxide-ZnO nanorod-based ternary nanocomposite as a superhydrophobic and corrosion-barrier coating", *Colloids Surf. A: Physicochem. Eng. Aspects*, 611 (2021) 125793.
[41] A. Singh and S. Singh, "ZnO nanowire-coated hydrophobic surfaces for various biomedical applications", *Bull. Mater. Sci.*, 41 (2018) 94.
[42] R. Wenzel, "Resistance of Solid Surfaces to Wetting by Water", *Ind. Eng. Chem.*, 28(8) (1936) 988-994.
[43] A. Cassie and S. Baxter, "Wettability of porous surfaces", *Trans. Faraday Soc.*, 40 (1944) 546-551.

 ISSN (print) 1813-2065, (online) 2309-1673

IRAQI JOURNAL OF APPLIED PHYSICS
Vol. 19, No. 4A, October 2023, pp. 73-76

Spectroscopic Characterization of Silicon Nitride Thin Films Prepared by DC Reactive Sputtering Using Silicon Targets with Different Types of Conductivity

Diyar A. Taher
Mohammed A. Hameed

Department of Physics, College of Science, University of Baghdad, Baghdad, IRAQ

In this work, silicon nitride thin films were prepared by dc reactive sputtering technique using silicon targets with different types of electrical conductivity (n-type and p-type) and Ar:N_2 gas mixing ratio of 70:30. The optical microscopy and spectroscopic characteristics of these films were determined in order to introduce the effect of target conductivity type on these characteristics. The results showed that using p-type silicon target would produce Si_3N_4 films with lower tendency to adsorb water vapor and other constituents of the atmospheric air, higher absorbance in the visible range 400-700nm, and lower variation in the energy band gap with film thickness than the Si_3N_4 films prepared from n-type silicon target.

Keywords: Silicon nitride; Reactive sputtering; Thin films; Nanostructures
Received: 30 March 2023; **Revised:** 01 June 2023; **Accepted:** 08 July 2023

1. Introduction

Silicon nitride (Si_3N_4) is widely used as a hard optical material with excellent piezoelectric response [1-3]. In addition to its many photonic applications, the Si_3N_4 and $SiN_{1.3}$ films are employed in the surface loading of crystalline silicon solar cells, high-frequency piezoelectric transducers, biomedical applications and nanostructures [4-8]. Silicon nitride is an important insulating material for light emitting diodes and transistors as well as for insulating gate applications [9]. Si_3N_4 exhibits high resistivity (~10^{13} Ω.cm), dielectric constant of 7.0 and wide energy gap (5.06-5.25 eV) [10,11]. It can be found in two main structural phases, α-Si_3N_4 and β-Si_3N_4 those are both hexagonal [12,13]. The chemical bonding of both phases is attributed to the interference of sp^3 hybrid orbitals of silicon atoms with the sp^2 hybrid orbitals of nitrogen atoms [14]. The fundamental unit of Si_3N_4 lattice is the SiN_4 tetragon as the Si atom is located at the center of the tetragon while four N atoms are located at the corners [15]. The Sin_4 tetragons are connected throughout the corners as each N atom is shared by three tetragons. Hence, each N atom will have three neighboring Si atoms [16,17].

Similar to most semiconductors, the intrinsic conductivity can be changed into extrinsic semiconductors by doping with n-type or p-type dopants to serve certain photonics and optoelectronics applications [18,19]. Obviously, the main difference between the two types of the conductivity in semiconductors may determine the structural, optical and electrical properties of the silicon compounds, such as Si_3N_4 and SiO_2, made from n-type or p-type silicon atoms. Therefore, the fact that the holes are the majority charge carriers in a p-type semiconductor should be carefully considered when atoms are ejected from such material to bond to other atoms and form new compound [20]. Regardless that both hole and electron have the same electrical charge, they are different in their masses and hence different in their effects on the structural characteristics of the silicon-based compound [1,4,8].

In this work, the effect of conductivity type of silicon target on the spectroscopic characteristics of the silicon nitride nanostructures prepared by dc reactive magnetron sputtering technique was introduced.

2. Experimental Part

In this study, silicon nitride thin films were deposited on glass and metallic (titanium) substrates using a homemade dc reactive sputtering system. Both types of silicon wafers (n-type and p-type) were used as targets. These targets and substrates were cleaned with ethanol and distilled water before the deposition process. The electric discharge of the argon was used to generate plasma required for sputtering. The operation parameters were classified into two groups: constant and variable. The constant

parameters include the vacuum pressure, discharge voltage, discharge current, deposition temperature, and inter-electrode distance. The variable parameters include the deposition time and Ar:N_2 gas mixing ratio for both types of silicon wafer conductivity. The inter-electrode distance was optimized at 4 cm. Figure (1) shows the optical microscopic images of two films deposited on Ti substrate using gas mixing ratio of 70:30 from n-type and p-type silicon targets.

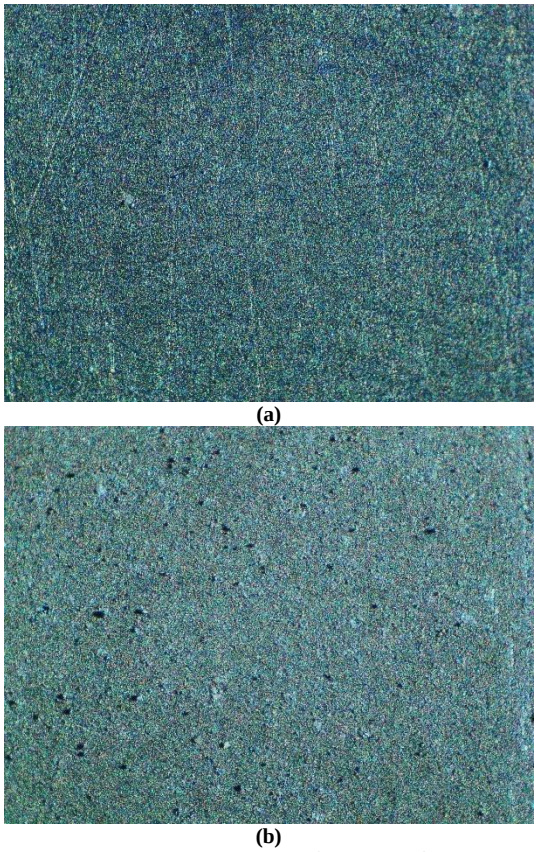

(a) **(b)**

Fig. (1) Optical microscope images of Si_3N_4 thin films prepared from (a) n-type Si target and (b) p-type Si target and deposited on Ti substrates using gas mixing ratio of 70:30

As the n-type silicon wafer was used mounted on the cathode as a target, the deposition chamber was initially evacuated down to 0.001 mbar and then the gas mixture of Ar:N_2 with mixing ratio of 50:50 was pumped into the chamber to prepare samples after different deposition times. The gas mixture pressure was about 0.15 mbar, the discharge voltage was 730 V and the discharge current was 50 mA. The mixing ratio was changed to 70:30. This procedure was repeated when the p-type silicon wafer was used. Both electrodes were cooled by circulating water through the inner channels of them. The nanopowders were extracted from the prepared thin film samples by the conjunctional freezing-assisted ultrasonic method.

The spectroscopic characteristics of he prepared samples were introduced by the UV-visible and Fourier-transform infrared (FTIR) spectroscopy.

The thickness of the prepared films was determined by the laser fringes method as 1 mW semiconductor lasers (532 and 632 nm) was used to generate concentric fringes and then determine the film thickness using the following relation [21]:

$$t = \frac{\Delta x}{x} \cdot \frac{\lambda}{2} \qquad (1)$$

where Δx is the spacing between two adjacent bright fringes, x is the width of a bright fringe, λ is the wavelength of laser used

3. Results and Discussion

Figure (2) shows the FTIR spectra of the silicon nitride thin films prepared using two silicon targets with different types of conductivity (n- and p-type) and gas mixing ratio of 70:30. Two apparent peaks can be seen in Fig. (2a) at 958.56 and 1103.21 cm^{-1}, while similar peaks in Fig. (2b) can be seen at 958.56 and 1097.42 cm^{-1}. These peaks are ascribed to the vibration modes of the Si-N bonds in silicon nitride molecule. All peaks seen within 1400-3600 cm^{-1} are attributed to the environmental contaminations those reached the samples before the FTIR tests [22].

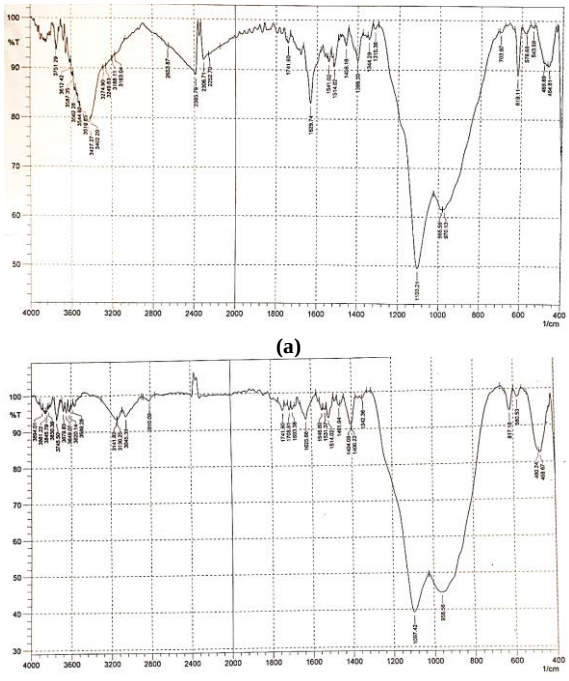

(a) **(b)**

Fig. (2) FTIR spectra of the Si_3N_4 samples prepared using gas mixing ratio of 70:30 from (a) n-type Si target, (b) p-type Si target

Figure (3) shows the absorption spectra of the thin film samples prepared after different deposition times (1, 1:30, 2, 2:30 and 3 hrs) in the spectral range of 300-800 nm. It is obvious that the shorter deposition times produces samples with lower thickness and hence lower absorbance. This is typical behavior as the shorter deposition time leads to growth of fewer number of layers forming the thin film. As shown in Fig. (3a), the sample prepared after deposition time of 1 hr shows an absorption peak at 400 nm and this peak is slightly shifted towards longer wavelengths as the deposition time is increased. Beyond 400 nm, all samples show low absorption in the visible region

 ISSN (print) 1813-2065, (online) 2309-1673

(450-700nm). On the other hand, figure (3b) shows that all samples exhibit high absorption in the UV region and the absorbance decreases to reach a minimum at about 490 nm. Then, the absorbance starts to increase and an absorption peak can be seen around 685 nm.

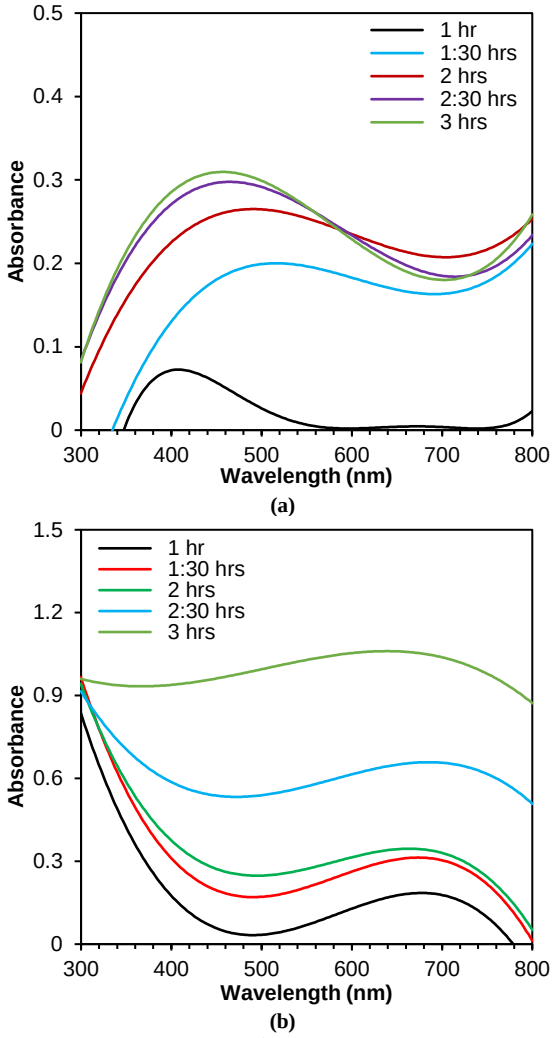

Fig. (3) Absorption spectra of the Si_3N_4 samples prepared using gas mixing ratio of 70:30 from (a) n-type Si target, (b) p-type Si target

The energy band gap of silicon nitride is ranging in 4.55-5.30 eV. Figure (4) shows the variation of energy band gap of the prepared Si_3N_4 samples with deposition time. It is clear that the variation in the energy band gap of the samples prepared from p-type Si target is smaller than that of samples prepared from n-type Si target. In general, increasing film thickness leads to create energy states within the band gap of the silicon nitride and hence decrease the energy band gap [23]. For the samples prepared from n-type silicon target, as the electrons are the majority charge carriers, then the majority silicon atoms sputtered from the target are bonded to nitrogen atoms to form Si_3N_4 molecules. This bonding is supported by the availability of electrons ready for covalent bonding. Consequently, the number of silicon nitride molecules is relatively large and the probability of the formation of intra-band states is decreasing with film thickness and hence the energy band gap is increased to reach its maximum at 4.2 eV before decreases with increasing film thickness due to the formation of intra-band states at large thickness.

On the other hand, the silicon atoms sputtered from p-type silicon target have the holes as the majority charge carriers, therefore, the concentration of electrons available for bonding is relatively low and hence the number of silicon nitride molecules is relatively small. Accordingly, the probability of the formation of intra-band states is low too but the energy band gap is ranging in the range 4.75-4.9eV.

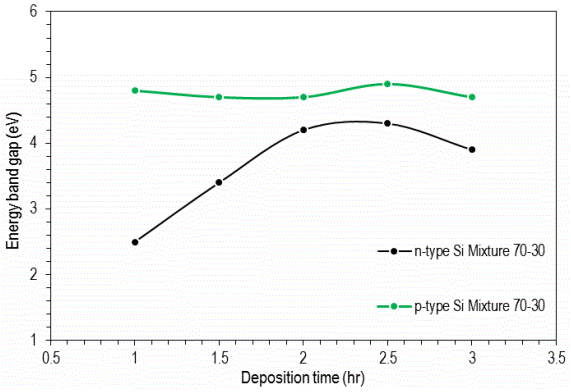

Fig. (4) Relation between energy band gap and deposition time for the Si_3N_4 samples prepared using 70:30 mixing ratio from n-type and p-type Si targets

4. Conclusion

In concluding remarks, the type of conductivity of silicon target used in the dc reactive sputtering technique has a reasonable role in determining the spectroscopic characteristics of the silicon nitride thin films prepared by this technique. Using p-type silicon target would produce Si_3N_4 films with lower tendency to adsorb water vapor and other constituents of the atmospheric air, higher absorbance in the visible range 400-700nm, and lower variation in the energy band gap with film thickness than the Si_3N_4 films prepared from n-type silicon target. These results are highly required to assess the prepared Si_3N_4 thin films for photonics, biomedical and gas sensing applications employing these films.

References

[1] P.M. Martin, **"Introduction to Surface Engineering and Functionally Engineered Materials"**, John Wiley & Sons, Inc. (NJ, 2011) 262-264.

[2] F.J. Kadhim and A.A. Anber, "Microhardness of Nanostructured Si_xN_{1-x} Thin Films Prepared by Reactive Magnetron Sputtering", *Iraqi J. Appl. Phys.*, 12(2) (2016) 15-19.

[3] S.M. Sze, "Current transport and maximum dielectric strength of silicon nitride films", *J. Appl. Phys.*, 38 (1967) 2951-2955.

[4] O.A. Hammadi, M.K. Khalaf and F.J. Kadhim, "Fabrication and Characterization of UV Photodetectors Based on Silicon Nitride Nanostructures Prepared by Magnetron Sputtering", *Proc. IMechE, Part N, J. Nanomater. Nanoeng. Nanosys.*, 230(1) (2016) 32-36.
[5] H. Lorentz et al., "Characterization of low temperature SiO_2 and Si_3N_4 films deposited by plasma enhanced evaporation", *J. Vac. Sci. Technol. B*, 9 (1991) 208-214.
[6] F.J. Kadhim and A.A. Anber, "Fabrication of nanostructured silicon nitride thin film gas sensors by reactive direct current magnetron sputtering", *Proc. IMechE, Part N, J. Nanomater. Nanoeng. Nanosys.*, 231(4) (2017) 173-178.
[7] J.G. Simmons, "Conduction in thin dielectric films", *J. Phys. D: Appl. Phys.*, 4 (1971) 613-657.
[8] S.W. Hseih et al., "Properties of plasma-enhanced chemical-vapor-deposited a-SiN_x:H by various dilution gases", *J. Appl. Phys.*, 76 (1994) 3645-3655.
[9] E.C. Paloura, J. Lagowski and H.C. Gatos, "Growth and electronic properties of thin Si_3N_4 films grown on Si in a nitrogen glow discharge", *J. Appl. Phys.*, 69 (1991) 3995-4002.
[10] F.J. Kadhim and A.A. Anber, "Fabrication of Nanostructured Silicon Nitride Films by Reactive DC Magnetron Sputtering for Gas Sensing Applications", *Proc. IMechE, Part N, J. Nanoeng. Nanosys.*, 231(4) (2017) 173-178.
[11] B.K. Nasser and M.A. Hameed, "Narrow Emission Linewidth of Highly-Pure Silicon Nitride Nanoparticles in Different Dye Solutions as Random Gain Media", *Nonl. Opt. Quant. Opt.*, 35(1-2) (2020) 99-105.
[12] O.A. Hammadi, "New Technique to Synthesize Silicon Nitride Nanopowder by Discharge-Assisted Reaction of Silane and Ammonia", *Mater. Res. Exp.*, 8(8) (2021) 085013.
[13] X.F. Zhang, P.G. Wen and Y. Yan, "Silicon nitride thin films deposited by DC pulse reactive magnetron sputtering", *Proc. SPIE* 7995, 7th *Int. Conf. on Thin Film Phys. Appl.*, 17 February 2011, paper no. 79951M.
[14] S.V. Deshpande et al., "Optical properties of silicon nitride films deposited by hot filament chemical vapor deposition", *J. Appl. Phys.*, 77(12) (1995) 6534-6541.
[15] O.A. Hammadi, M.K. Khalaf and F.J. Kadhim, "Silicon Nitride Nanostructures Prepared by Reactive Sputtering Using Closed-Field Unbalanced Dual Magnetrons", *Proc. IMechE, Part L, J. Mater.: Design and Applications*, 231(5) (2017) 479-487.
[16] A.A. Anber and F.J. Kadhim, "Preparation of Nanostructured Si_xN_{1-x} Thin Films by DC Reactive Magnetron Sputtering for Tribology Applications", *Silicon*, 10(3) (2018) 821-824.
[17] B.K. Nasser and M.A. Hameed, "Structural Characteristics of Silicon Nitride Nanostructures Synthesized by DC Reactive Magnetron Sputtering", *Iraqi J. Appl. Phys.*, 15(4) (2019) 33-36.
[18] F.J. Kadhim, O.A. Hammadi and A.A. Anber, "Spectroscopic Study of Chromium-Doped Silicon Nitride Nanostructures Prepared by DC Reactive Magnetron Sputtering", *Iraqi J. Appl. Phys.*, 17(2) (2021) 9-12.
[19] O.A. Hammadi, M.K. Khalaf, F.J. Kadhim and B.T. Chiad, "Operation Characteristics of a Closed-Field Unbalanced Dual-Magnetrons Plasma Sputtering System", *Bulg. J. Phys.*, 41(1) (2014) 24-33.
[20] D.A. Taher and M.A Hameed, "Effect of Target Conductivity Type on Optical Constants of Silicon Nitride Thin Films Prepared by DC Reactive Sputtering", *Iraqi J. Appl. Phys. Lett.*, 6(3) (2023) 15-18.
[21] M. Ohring, **"The Materials Science of Thin Films"**, Academic Press (San Diego, 1992) Ch. 4, 182.
[22] N.N. Greenwood and E.J.F. Ross, **"Index of Vibrational Spectra of Inorganic and Organometallic Compounds"**, vol. III, The Butterworth Group (London, 1966) 800, 1078.
[23] T.E. Cook Jr et al., "Band offset measurements of the Si_3N_4/GaN (0001) interface", *J. Appl. Phys.*, 94(6) (2003) 3949-3954.

 ISSN (print) 1813-2065, (online) 2309-1673 PRINTED IN IRAQ

IRAQI JOURNAL OF APPLIED PHYSICS
Vol. 19, No. 4A, October 2023, pp. 77-80

Inaam M. Abdulmajeed [1]
Suha H. Ibraheem [2]

[1] *Department of Physics, College of Science, University of Baghdad, Baghdad, IRAQ*
[2] *College of Basic Education, Mustansiriyah University, Baghdad, IRAQ*

Preparation and Characterization of Biomaterial Powder by Sol-gel Method

This investigation is focused on the production of hydroxyapatite (HA) powder and the impact of calcination temperature on the crystalline structure of HA. This work involved the chemical synthesis of HA powder utilizing stoichiometric ratios of the initial ingredients, followed by gel formation, drying, crushing, and calcination at temperatures ranging from 600°C to 800°C. Samples sintered at 600°C and 800°C were examined for their mechanical characteristics, such as Vickers microhardness and Young's modulus. The results demonstrated that higher sintering temperatures improved crystallinity and stiffness via increasing microhardness and Young's modulus. The synthetic HA powder's polycrystalline nature was confirmed by x-ray diffraction (XRD) examination, with the main peak exhibiting the maximum crystallinity. Debye-equation Scherrer's formula was used to get the average crystallite size. The investigation of hydroxyapatite functional groups using Fourier-transform infrared spectroscopy (FTIR) revealed distinctive peaks.

Keywords: Hydroxyapatite; Bioceramics; Microstructure; Sol-gel
Received: 10 June 2023; **Revised:** 12 August 2023; **Accepted:** 15 August 2023

1. Introduction

In biological systems, the primary inorganic element in the structure of bones and teeth is hydroxyapatite (HA). In 1981, HA was used for the first time to treat a periodontal lesion, which has the same meaning as the term "periodontal", which refers to the area of dentistry that deals with the framework that supports and surrounds teeth. A lesion is a section of an organ or tissue that has been harmed by trauma or illness. In the medical field, HA is widely used and its applications have grown to include films, solid blocks, and solid components for dental implants [1]. Due to its exceptional biocompatibility, calcium phosphate has undergone substantial research for potential biomedical applications, numerous investigations have demonstrated that HA ceramics have the potential to connect directly to the host bone and exhibit no toxicity, inflammation, pyrogenetic reaction, or fibrous tissue formation [2].

In recent years, researchers working in the field of biomaterials have been interested in hydroxyapatite $Ca_{10}(PO_4)_6(OH)_2$, as an essential inorganic biomaterial [3,4]. On the basis of crystallographic and chemical research, it is known that synthetic HA and naturally occurring HA are comparable. Different methods can be used to prepare HAp particles such as modified precipitation [5,6], hydrothermal [7], and sol-gel [8]. The microstructural characteristics of HAp, including sintered density, grain size, grain size distribution, and microstructural flaws, heavily influence their mechanical performance. In order to create ceramic HAp with a high sintered density and suitable microstructure, the preparation of fine and well-calcination temperature of HAp powder is the most crucial stage [9].

The main objective of this work is to synthesize hydroxyapatite powder by sol-gel method and study the effect of calcination temperature on the crystalline structure to obtain a high degree of crystallinity and purity of HA powder which may be developed later to use in a biomedical applications. Mechanical properties such as Vickers microhardness and Young's modulus for the prepared samples were studied as a function of sintering temperature.

2. Experimental Work

The chemicals such as Ca $(NO_3)_2.4H_2O$ supplied by Himedia with 99.5% purity and P_2O_5 with 99% purity were used as starting materials. Stoichiometric ratios for each component were used to prepare $Ca_{10}(PO_4)_6.(OH)_2$. Each compound was dissolved in 100 ml of ethanol, then both solutions were slowly mixed using magnetic stirrer for 20 minutes until the formation of a gel. The prepared gel was dried in an electric oven at 70°C for 20 hours. The prepared compound was crushed in agate mortar and calcined at temperature of 600 to 800°C with heating rate of 5°C/min for 3 hours. The powders were finally cooled by switching off the furnace to room temperature.

The mechanical properties such as Vickers microhardness and Young's modulus of the prepared hydroxyapatite samples were studied as functions of sintering temperature.

According to the hexagonal crystallite structure of hydroxyapatite, the lattice constant parameters were calculated by [10,11]

$$\frac{1}{d^2} = \frac{4}{3}\left[\frac{h^2+k^2+hk}{a^2}\right] + \frac{l^2}{c^2} \quad (1)$$

where *hkl* are Miller indices of crystal plane, *d* denotes the distance between neighboring planes, and the lattice constants were determined to be a=b=9.4116 and c=6.11

The following Debye-Scherrer's formula was used to determine the average crystallite size [12]:

$$D = \frac{0.9\lambda}{\beta\, cos\theta} \quad (2)$$

The following formula was employed to determine the volume of a hexagonal unit cell in hydroxyapatite [11,12]:

$$V = 2.589a^2c \quad (3)$$

The specific surface area of hydroxyapatite was calculated using the following formula:

$$S = \frac{6\times10^3}{D\times\rho} \quad (4)$$

where D is the crystallite size, and ρ is the theoretical density of HAp (3.16 g/cm^3)

A special hardness instrument is normally used to conduct the Vickers hardness test on the prepared Hap samples placed on the stage of the testing device. A load of 1 kg was applied to imprint a diamond tip. The device will press down on the sample's surface for a predetermined amount of time (often 10 to 30 s). Once the load is released, the two diagonals (d_1 and d_2) of the indentation are measured using a built-in optical microscope in the testing device. The measurement was repeated many times for sake of accuracy. The Vickers hardness number (H_V) is determined by the following formula [13]:

$$H_v = 1.854 \times \frac{F}{(d_1\times d_2)} \quad (5)$$

where F is the applied load in kilograms

The ASTM standard D2845-08 is used to perform the V-Meter MK IV ultrasonic instrument.

The following equation was used to compute elastic modulus [14]:

$$E = \frac{V_L^2\rho(1+\gamma)(1-2\gamma)}{1-\gamma} \quad (6)$$

where E, ρ, and V_L are respectively the elastic modulus, bulk density, ultrasonic longitudinal wave velocity

$$\gamma = \frac{1-2(\frac{v_T}{v_L})^2}{2-2(\frac{V_T}{V_L})^2} \quad (7)$$

where V_T and V_L are transverse and longitudinal velocity, respectively

With fracture toughness defined as the material's resistance to crack propagation, an empirical relationship between hardness and fracture toughness is utilized by indentation fracture toughness technique. The Vickers indent and cracks profile were observed under an optical microscope on the surface of prepared sample in order to determine the precise values of the fracture lengths. The Vickers hardness (H_V) and fracture toughness (K_{IC}) of a material are related by the indentation fracture toughness equation, which is a frequently used correlation. This method proposed by Antis et al. [15] offers an estimation of fracture toughness as

$$K_{IC} = 0.0161 \times (\frac{E}{H_v})^2 \times \frac{P}{C^{1.5}} \quad (8)$$

A load of 50 N was used in this work. It is reasonable to infer that the created cracks will always have a half-penny median crack profile. This suggests that only an equation specifically appropriate for half-penny median cracks should be used for this study in order to calculate K_{IC}. Figure (1) shows the profile of half-penny median, which typically develops at low indentation loads. This type of cracks combines with the cracks at the indent's corner to create the radial-median crack by diffusing beneath the indent [16].

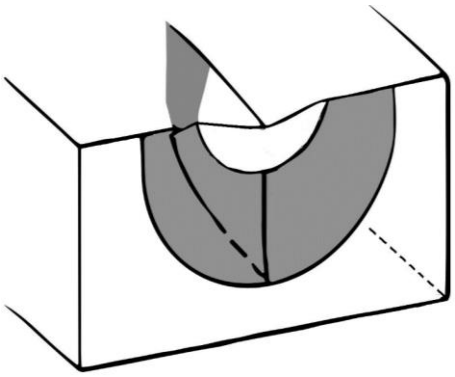

Fig. (1) A radial-median crack brought on by the Vickers load

3. Results and Discussion

Figure (2) illustrates the XRD patterns for the samples prepared at 600 and 800°C. The scanning range of diffraction angle (2θ) was 10-80° for all samples. By comparing between the resulting patterns and tabulated data of HA for 2θ, peak intensity, and Miller indices with the International Centre for Diffraction Data (ICDD) card no. 96-431-7044, it is clear that the prepared hydroxyapatite $Ca_{10}(PO_4)_6.(OH)_2$ powder is polycrystalline and the highest peak on the pattern corresponds to the highest plane crystallinity.

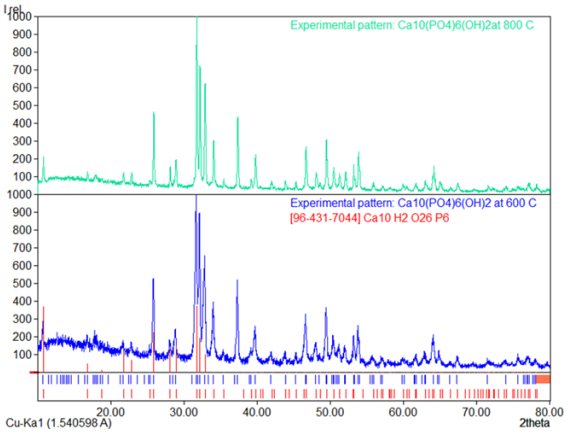

Fig. (2) XRD patterns of HAp powder prepared at 600 and 800°C

 ISSN (print) 1813-2065, (online) 2309-1673

Debye-Scherrer's formula was used to determine the average crystallite size of Hap prepared at 800°C to be 36.27 nm. Equation (3) was used to calculate the hexagonal unit cell volume of the HAp structure to be 1365.5203. It was found that the specific surface area (S) was 52.349 using Eq. (4).

The FTIR spectra of HA powder prepared at 600 and 800 °C, respectively, are shown in figures (3) and (4). It is clear that the vibrational and stretching modes of the hydroxyapatite -OH groups have generated the peaks at 634 and 3571 cm^{-1}. The peaks seen at 468, 567, 603, 960, and 1039-1093 cm^{-1} are attributed to the distinctive tetrahedral structure of PO_4^{-3}. The $PO_4^{-3}(2\upsilon)$ and $PO_4^{-3}(4\upsilon)$ modes are represented by the peaks at 468 and 567 cm^{-1}, respectively. Additionally, $PO_4^{-3}(3\upsilon)$ mode is responsible for the peak seen at 960 cm^{-1}, while the $PO_4^{-3}(1\upsilon)$ mode is responsible for the peaks seen at 1093 and 1039 cm^{-1} [17].

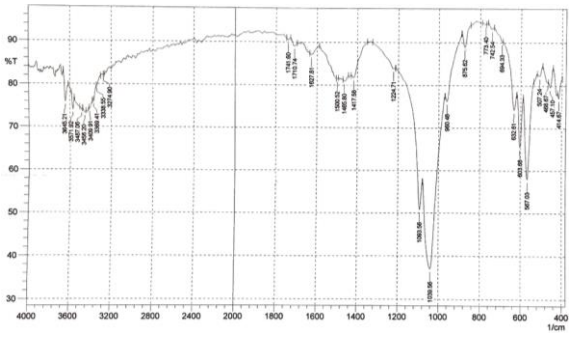

Fig. (3) FTIR spectrum of HA powder prepared at 600°C

Figure (4) shows a sharp peak at 3509 cm^{-1} and a medium peak at 634 cm^{-1} due to the stretching and vibrational, respectively, modes of the –OH groups of hydroxyapatites. The medium peaks seen at 1461 and 1417 cm^{-1} are ascribed to the CO_3^{-2} group. These peaks show that the PO_4^{-3} group in the HA lattice has been replaced by the CO_3^{-2} group, which may have begun when ambient carbon dioxide was adsorbed [18]. Therefore, it is clear that the synthetic powder is unquestionably hydroxyapatite.

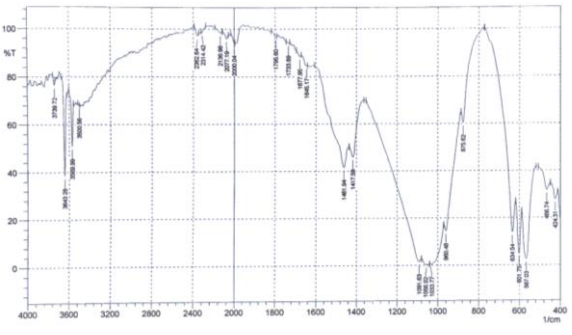

Fig. (4) FTIR spectrum of HA powder prepared at 800°C

The grain size of pure HAp was also measured using the field-emission scanning electron microscopy (FE-SEM). The concept that temperature-dependent development of crystallite size occurring in the prepared samples was based on the surface morphology introduced by FE-SEM. This can be used to explain why these microstructures of derived HAp form during the thermal process since particles have a tendency to crystallize and congregate at high temperatures. Figure (5a) illustrates how the prepared HAp crystallized into nanoparticles with sizes between 14 and 49nm at 600°C. As the preparation temperature was increased to 800°C, HAp microstructures became more apparent (Fig. 5b). The crystallite size of the prepared HAp varies from 40 to 60 nm.

The FE-SEM microimages make it easy to see changes in the grain size and semi-spherical shape as the grain size increased with increasing preparation temperature.

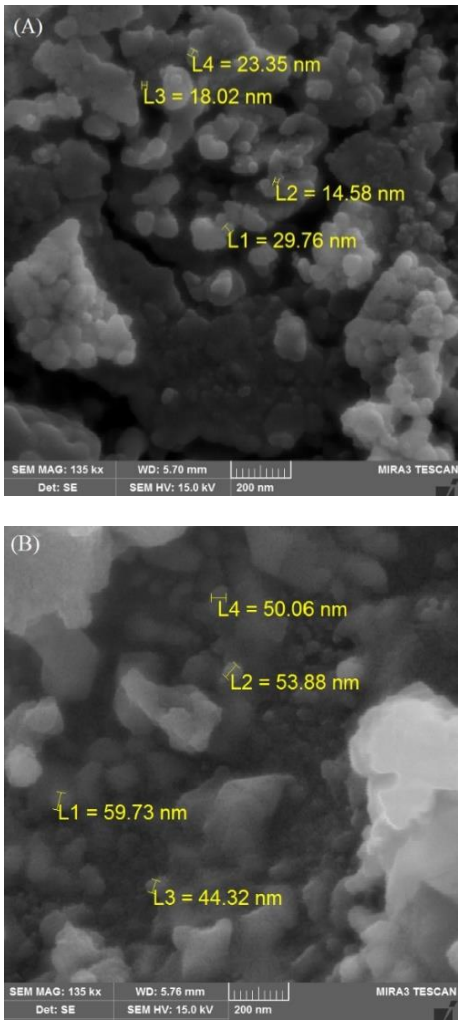

Fig. (5) SEM microimages of prepared HAp powder prepared at (A) 600°C and (B) 800°C

The exact qualities and the desired properties of the HAp would determine the ideal calcination temperature to reach the maximum microhardness. Table (1) shows that the microhardness increased with increasing sintering temperature.

The Young's modulus, which refers to the material's stiffness or elasticity and quantifies how

stress and strain interact during deformation, was determined. This modulus of HAp can be influenced by the calcination temperature, which can also alter the crystal structure, grain size, and porosity of the prepared material.

Table (1) shows values of some mechanical parameters as a function of sintering temperature. The Young's modulus of the prepared HAp typically increase, similar to microhardness, with increasing sintering temperature. A more rigid structure is produced as a result of better crystallinity being promoted by higher sintering temperatures. As a result, at higher temperatures, the Young's modulus has a tendency to be larger.

Table (1) Values of some mechanical parameters as a function of sintering temperature

Sintering Temperature (°C)	V_l (m/s)	V_T(m/s)	Bulk density (kg/m^3)	Vickers Hardness (GPa)	Young's Modulus (GaP)	K_{IC} (MPa /m$^{1/2}$)
600	3464.2	2313	1862	4.2	1.205	2.828
800	3772.1	2494	2442	7.4	2.105	4.606

4. Conclusions

This work involved the chemical synthesis of hydroxyapatite (HA) powder and analysis of the effect of calcination temperature on the crystalline structure of the material. The prepared HA powder was polycrystalline. The average crystallite size of the prepared powder calcined at 800°C was determined to be 36.27 nm. The particle size was found to increase with increasing calcination temperature. Also, Vickers microhardness and Young's modulus were both increasing with temperature, showing enhanced crystallinity and stiffness. The findings of this work may contribute to the understanding of production, characterization, and potential applications of HA powder in biomedical fields.

References

[1] Y. Javad et al., "A short view on nanohydroxyapatite as coating of dental implants", *Biomed. Pharmacother.*, 105 (2018) 553-557.

[2] A.N. Lipton, A. Fathima and S.G.P. Vincent, "In-vitro Evaluation of Chitosan-Hydroxyapatite Nanocomposite Scaffolds as Bone Substitutes with Antibiofilm Properties", *J. Pure Appl. Microbiol.*, 15(3) (2021) 1455-1471.

[3] F. Elisa et al., "Hydroxyapatite for Biomedical Applications: A Short Overview", *Ceramics*, 4 (2021) 542-563.

[4] S. Pokhrel, "Hydroxyapatite: Preparation, Properties and Its Biomedical Applications", *Adv. Chem. Eng. Sci.*, 27 (2018) 225-240.

[5] G.C. Koumoulidis et al., "Preparation of hydroxyapatite nanoparticles using a modified precipitation method", *Demokritos National Centre for Scientific Research, Institute of Materials Science*, 156 (2003) 10, 83-90.

[6] S. Ramesh et al., "Sintering properties of hydroxyapatite powders prepared using different methods", *Ceram. Int.*, 39(1) (2013) 111-119.

[7] M. Guoqing, "Three common preparation methods of hydroxyapatite", *Mater. Sci. Eng.*, 688 (2019) 033057, 1-12.

[8] L. Sopyan, R. Singh and M. Hamdi, "Synthesis of nano sized hydroxyapatite powder using sol-gel technique and its conservation to dense and pours bodies", *Indian J. Chem.*, 47A(11) (2008) 1626-1631.

[9] A.J. Ruys et al., "Sintering effects on the strength hydroxyapatite", *Biomater.*, 16 (1995) 409-415.

[10] Z.Y. Li et al., "Chemical composition, crystal size and lattice structural changes after incorporation of strontium into biomimetic appetite", *Biomater.*, 28 (2007) 1452-1460.

[11] Y. Waseda, E. Matsubara and K. Shinod, **"X-Ray Diffraction Crystallography"**, Springer (Heidelberg, 2011).

[12] I. Uysal et al., "Co-doping of hydroxyapatite with zinc and fluoride improves mechanical and biological properties of hydroxyapatite", *Prog. Nat. Sci. Mater. Int.*, 24(4) (2014) 340-349.

[13] B.D. Cullity, **"Elements of X-ray Diffraction"**, Addison-Wesley Pub. Co., Inc. (1978).

[14] A. Benhammou et al., "Mechanical behavior and ultrasonic non-destructive characterization of elastic properties of cordierite-based ceramics", *Ceram. Int.*, 39(1) (2013) 21-27.

[15] G.R. Anstis et al., "A Critical Evaluation of Indentation Techniques for Measuring Fracture Toughness: I, Direct Crack Measurements", *J. Am. Ceram. Soc.*, 64(9) (1981) 533-538.

[16] R.F. Cook, "Direct Observation and Analysis of Indentation Cracking in Glasses and Ceramics", *J. Am. Ceram. Soc.*, 73(141) (1990) 787-817.

[17] A. Hanifi and M.H. Fathi, "Bioresorbability Evaluation of Hydroxyapatite Nanopowders in a Stimulated Body Fluid Medium", *Iranian J. Pharmaceut. Sci.*, 4(2) (2008) 141-148.

[18] I. Uysal et al., "Co-doping of hydroxyapatite with zinc and fluoride improves mechanical and biological properties of hydroxyapatite", *Prog. Nat. Sci. Mater. Int.*, 24(4) (2014) 340-349.

 ISSN (print) 1813-2065, (online) 2309-1673

IRAQI JOURNAL OF APPLIED PHYSICS
EDITORIAL BOARD

COPYRIGHT RELEASE FORM
IRAQI JOURNAL OF APPLIED PHYSICS (IJAP)

We, the undersigned, the author/authors of the article titled

……
……
……
……
……
……
……

that is submitted to the Iraqi Journal of Applied Physics (IJAP) for publication, declare that we have neither taken part or full text from any published work by others, nor presented or published it elsewhere in any other journal. We also declare transferring copyrights and conduct of this article to the Iraqi Journal of Applied Physics (IJAP) after accepting it for publication.

The authors will keep the following rights:

1. Possession of the article such as patent rights.
2. Free of charge use of the article or part of it in any future work by the authors such as books and lecture notes after informing IJAP editorial board.
3. Republishing the article for any personal purposes of the authors after taking journal permission.

To be signed by all authors:

Signature:……..date: ……
Printed name: ……

Signature:……..date: ……
Printed name: ……

Signature:……..date: ……
Printed name: ……

Correspondence author:……..……...……...
……
Address:……..……
……
Telephone:……..……..email: ……

Note: Complete and sign this form and mail it to the below address with your finally revised manuscript

The Iraqi Journal of Applied Physics
P. O. Box 88052, Baghdad 12631, IRAQ
www.iraqiphysicsjournal.com
Email: info@iraqiphysicsjournal.com
Email: editor_ijap@yahoo.co.uk
Email: ijap.editor@gmail.com

IRAQI JOURNAL OF APPLIED PHYSICS

Volume (19) Issue (4A) October 2023

CONTENTS